Understanding the Viability of Impurity-Band Photovoltaics: A Case Study of S-doped Si

by

Joseph Timothy Sullivan

B.S., Mechanical Engineering
Cornell University (2007)
M.S., Civil & Environmental Engineering
Stanford University (2008)

Submitted to the Department of Mechanical Engineering
in partial fulfillment of the requirements for the degree of

Doctor of Philosophy

at the

MASSACHUSETTS INSTITUTE OF TECHNOLOGY

June 2013

Author .....
Department of Mechanical Engineering
May 18, 2013

Certified by .....
Tonio Buonassisi
Associate Professor
Thesis Supervisor

Accepted by .....
David E. Hardt
Chairman, Committee on Graduate Students

Understanding the Viability of Impurity-Band Photovoltaics: A Case Study of S-doped Si

by

Joseph Timothy Sullivan

Submitted to the Department of Mechanical Engineering
on May 18, 2013, in partial fulfillment of the
requirements for the degree of
Doctor of Philosophy

Abstract

This thesis explores the electronic structure, optical properties, and carrier lifetimes in silicon that is doped with sulfur beyond the equilibrium solid solubility limit, with a focus on applications as an absorber layer for an impurity-band photovoltaic device. The concept of an impurity-band material envisions the creation of a band of electronic states by incorporating high concentrations of deep-level dopants, which enable the generation of free carriers using photons with energy less than that of the band gap of the host semiconductor. The investigations reported in this thesis provide a framework for the appropriate selection of impurity-band candidate materials. The thesis is divided into three primary sections, one for each of three experimental techniques, respectively.

First, the electronic band structure is studied using synchrotron-based x-ray emission spectroscopy. These spectra provide the first insights into how the electronic structure changes as the sulfur concentration is increased across the metal-insulator transition, and how the electronic structure is linked to the anomalously high sub-band gap absorption. A discrete change in local electronic structure is seen that corresponds to the macroscopic change in electronic behavior. Additionally, a direct correlation is seen between sulfur-induced states and the sub-band gap absorption.

Next, the optical properties are studied using Fourier transform infrared spectroscopy. Extraction of the complex index of refraction is performed using numerical models that simulate both the transmission and reflection measurements. Analysis of the absorption coefficient determines the position of the sulfur-induced states within the band gap and their optical cross section for different sulfur concentrations and annealing conditions. At sulfur concentrations above the metal-insulator transition, the sulfur states become degenerate or near-degenerate with the conduction band, and such high concentrations are deemed to have an electronic structure unsuitable for an impurity-band photovoltaic material.

Third, low-temperature photoconductivity experiments determine the mobility-lifetime product for carriers generated via sub-band gap photons. Combining both the FTIR optical results with the mobility-lifetime product measured from photocon-

ductivity experiments provide the first empirical determination of the impurity-band figure of merit for sulfur-doped silicon. The figure of merit is found to be over an order of magnitude too low to be suitable as an impurity band absorber layer.

Finally, in the conclusion, future directions and a predictive methodology for selecting new candidate impurity band materials that hold promise are discussed. The predictive methodology describes a simple way to estimate the figure of merit for super-saturated materials solely using literature values of the optical and electrical capture cross sections at dilute concentrations.

Thesis Supervisor: Tonio Buonassisi
Title: Associate Professor

Acknowledgments

In the many years that I've spent at MIT, I'd like to acknowledge several people and organizations who have helped or enabled my research. The National Science Foundation and the MIT Energy Initiative granted fellowships to me that funded my graduate research.

I'd like to thank many of my hyperdoped Si collaborators, especially Mark Winkler, Dan Recht, Elif Ertekin, Jacob Krich, Renee Sher, Christie Simmons, Austin Akey, Peter Persans, Mike Aziz, and Jonathan Mailoa. Discussions with this group of scientists has helped me grow and develop as a scientist and a researcher. I'd also like to acknowledge the entire group in the PV Laboratory who have provided an excellent environment to work.

I'd like to thank my advisor Tonio Buonassisi, who gave me the freedom to pursue many academic interests; as his advisee I was able to spend significant time teaching, developing new coursework, and creating and developing the PV Lab Solar Bootcamp program.

I'd like to thank all the lab members who came to participitate in the PV Lab Solar Bootcamp. Everyone who participated made the experience worthwhile for me and incredibly gratifying.

Christine and Nick made my first year at MIT feel like a home away from home and continue to do so even though they live so far away, so thanks! And a special thanks to Finn Piro, for reminding us why life is important.

I'd also like to acknowledge Leslie Regan, whose kindness and warmth first attracted me to MIT in the first place on visit weekend. Also, special thanks Leslie Regan, Una Sheehan, and Joan Kravit, whose administrative wizardry keeps the Mechanical Engineering department running smoothly.

A special thanks to my fellow graduate students who kept me sane during my graduate career and were always available to share a home-brew or a draft at the Muddy: Sam Crawford, David Fenning, Andrej Lenert, and Bill Polachek. I owe a special thanks to Kevin Cedrone, who actually read and gave constructive criticism

on this thesis. I'd also like to thank Meaghan Killian for keeping Kevin in line.

I'd also like to thank my parents, Elaine and Dick Sullivan, for always being supportive, caring, and some of my biggest advocates.

I'd like to thank my wife, Renée, who has kept me happy and motivated throughout this whole process. May the fourth be with you!

Symbols

Below is a list of symbols used in this thesis and their physical meaning. If a standard set of units is used throughout the thesis, they are reported in brackets.

Symbol	Description
α	absorption coefficient [cm^{-1}]
a_B	Bohr radius
ϵ_0	dielectric constant of free space
e	charge of an electron
E_T	trap energy [eV]
E_σ	standard deviation of trap energies [eV]
G	generation rate of carriers [cm^{-3} s^{-1}]
$\hbar\omega$	photons energy [eV]
k	complex component of index of refraction, often referred to as the extinction coefficient
λ	wavelength of light
$\mu_{e,h}$	mobility for electrons or holes [cm^2/s]
$\tilde{n}$	complex index of refraction $(n + ik)$
n	real part of index of refraction
n, p	free carriers in the conduction and valence bands, respectively
Δn, Δp	excess carriers in conduction or valence band [cm^{-3}]
$\sigma_{e,h}$	electrical capture cross-section for electrons or holes
$\sigma_{O_{e,h}}$	optical cross-section for generating electrons and holes via the impurity band, respectively
σ	electrical conductivity
$\tau_{e,h}$	effective or measured lifetime of carriers for either electrons or holes, respectively [s]
$\tau_{e0,h0}$	Shockley-Read-Hall recombination lifetime of electrons or holes when all trap states are empty or filled, respectively

R_m	measured reflectance (total intensity of light reflected toward incident light source off of sample)
R_S	sample resistance
ΔR_S	sample resistance
T_m	measured transmission (total intensity of light transmitted toward incident light source off of sample)

Acronyms

Below is a list of acronyms used in this thesis and their explanation.

Acronym	**Description**
CB	conduction band
DFT	density functional theory
DLTS	deep-level transient spectroscopy
DOS	density of states
EBSD	electron backscatter diffraction
FTIR	Fourier transform infrared spectroscopy
FCA	free-carrier absorption
IB	impurity band (i.e. state introduced by deep levels with the band gap)
IMT	insulator to metal transition
PLM	pulse laser melting (a process used to make S-hyperdoped Si)
RBS	Rutherford backscattering
RIXS	resonant x-ray emission spectroscopy
SEM	scanning electron microscope image
SIMS	secondary ion mass spectroscopy
SRH	Shockley-Read-Hall recombination statistics
TEM	transmission electron microscope
UPS	ultra-violet photoemission spectroscopy
VB	valence band

XAS	x-ray absorption spectroscopy
XES	x-ray emission spectroscopy using non-resonant excitation
XPS	X-ray photoemission spectroscopy
xTEM	cross-sectional transmission electron microscope

Contents

Chapter 1

Introduction

1.1 Motivation

At the moment of writing this thesis, current CO_2 concentrations in earth's atmosphere are at 395 ppm, up from the pre-industrial level of 270 ppm [145]. CO_2 levels of 450 ppm are considered "dangerous" with respect to climate change [45]. One way to reduce CO_2 emissions and prevent catastrophic climate change is to replace fossil fuels with renewable sources. Solar is an attractive option because this renewable resource is enormous (36,000 TW), especially when compared to wind energy (72 TW) [5]. Less than 0.1% of the solar resource is needed to meet global energy needs. Currently, renewable energy only accounts for a very small fraction of total energy consumption.

If solar is to scale up and provide TW/year levels of production, solar cells need to be cheap, efficient, and made from elements that are earth-abundant. Earth-abundance is a critical component of any solar technology, because scaling to manufacturing levels of TW/year requires that the elements that make up a solar cell must exist in sufficient quantities. In this thesis, we'll explore the material properties and potential efficiency improvements that result from hyperdoping a Si solar cell with S impurities. Incorporating S at supersaturated concentrations via hyperdoping can potentially increase the efficiency of a Si solar cell because S enables the utilization of the wider portion of the solar spectrum; this is achieved because S alters the elec-

tronic band structure of Si and creates of an intermediate band within the Si band gap. Hyperdoping Si with S (both Si and S are earth abundant elements) is done using fabrication techniques currently used in the solar industry, thus keeping additional fabrication costs to a minimum. This material system has many characteristics that make it a promising candidate for making solar cells that are cheap and can be produced at TW/year.

1.2 Losses in a Solar Cell

The vast majority of solar cells made commercially are based on a p-n junction structure. This device structure consists of layers of two differently doped layers: a p-type layer that is juxtaposed next to a n-type layer. Metal contacts on front and back allow extraction and transport of collected charge. A schematic of the physical structure of a standard p-n junction solar cells is produced in Figure 1-1.

The electronic band diagram of a the p-n junction shown in Figure 1-2, along with several of the primary loss mechanisms present in a solar cell. In Figure 1-2, an electric field exists between the p-type region on the left and the n-type region on the right. This electric field, which arises from from the difference in Fermi energy between the two differently doped regions, is what allows charge to be separated. This electric field pushes photo-generated electrons and holes to the n-type and p-type layers, respectively. While there are many losses in a solar cell, only the two largest losses will be addressed in this introduction: non-absorption and thermalization. These two loss-mechanisms are the two major losses that intermediate band solar cells aim to reduce.

Non-Absorption Losses

The first step in creating solar electricity is absorbing light. Generally, for a photon to be absorbed in a semiconductor, the photon needs to have an energy that is greater than the band gap energy. In Figure 1-2, these losses are shown as a red photon (loss mechanism #1) that does not get absorbed and is thus not utilized by the solar device

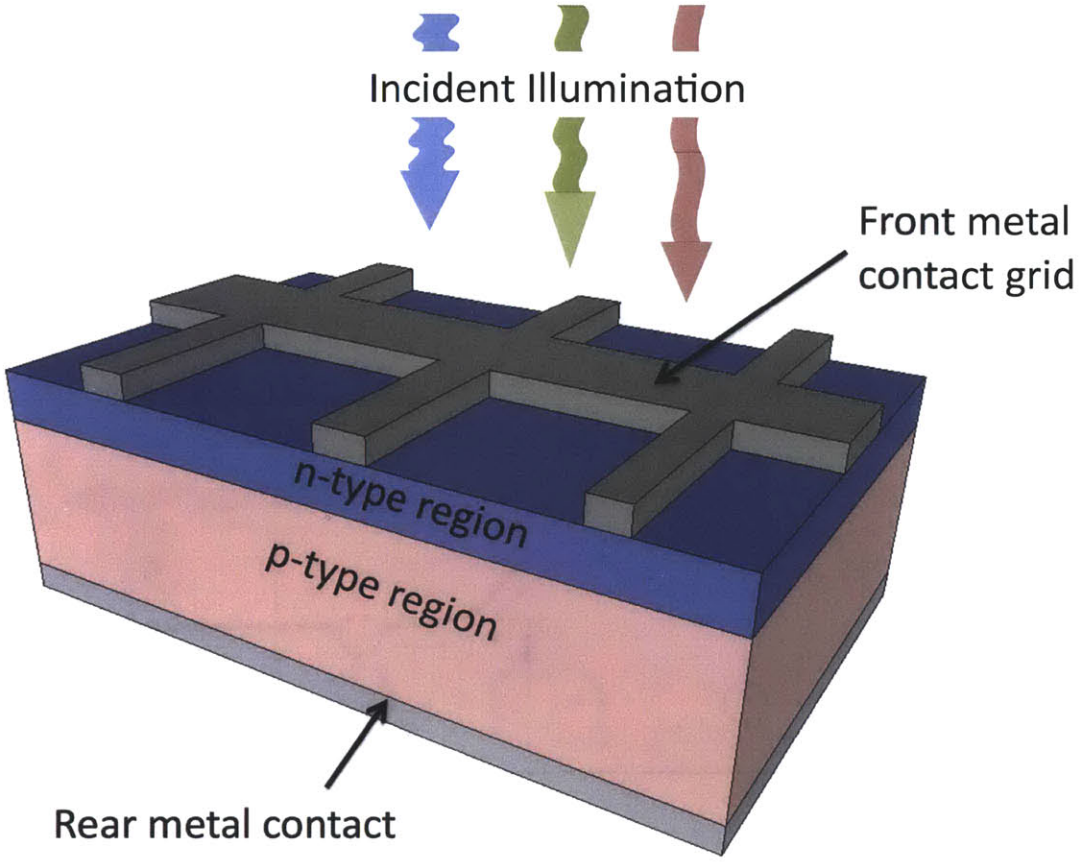

Figure 1-1: A cross-section of a typical p-n junction solar cell. Not shown are the textured surfaces or the front optical coating, often referred to as an anti-reflection coating.

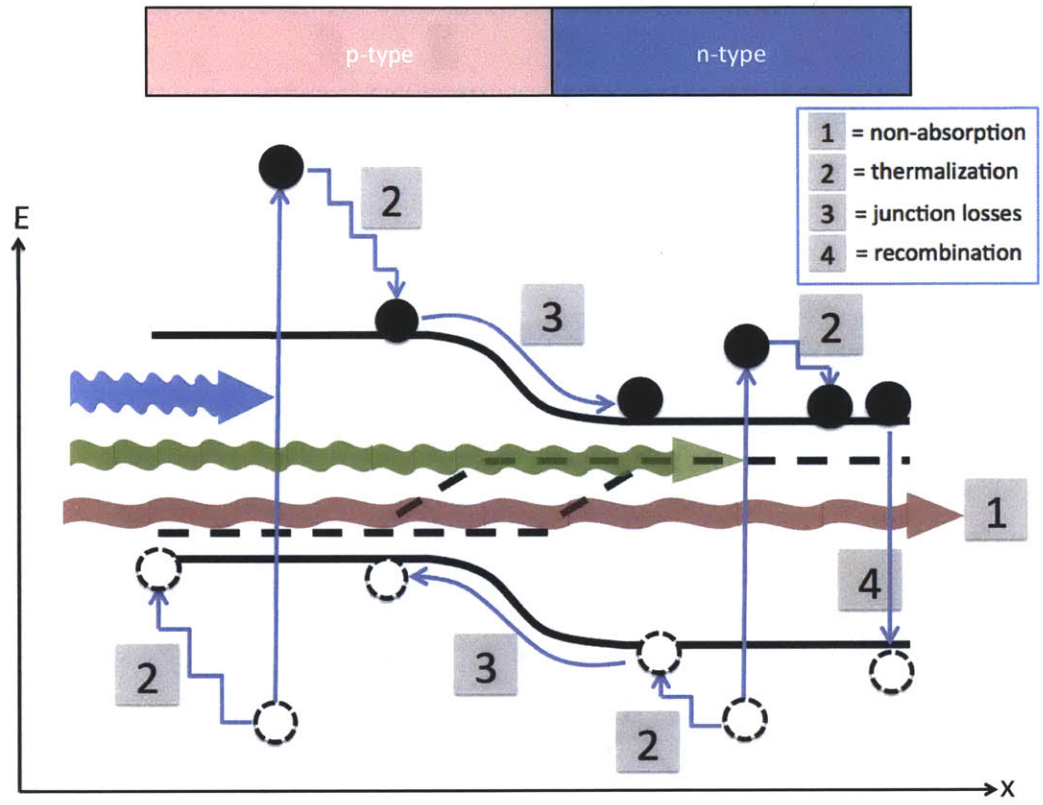

Figure 1-2: Band structure of a *pn* junction solar cell during operation and several important loss mechanisms: (1) non-absorption of photon with energy less the band gap energy, (2) thermalization of photo-excited carriers, (3) charge separation and junction losses, and (4) recombination of excess carriers. The upper and lower bold lines represent the conduction band minimum and valence band maximum, respectively. The dotted lines represents both the Fermi energies and quasi-Fermi energies in the region of high electric field (also known as the depletion region.)

to produce electricity. In contrast, both the green and blue photons are absorbed and create both mobile electrons and holes. In a silicon solar cell, non-absorption losses can be quite significant. In Figure 1-3 the solar spectrum (AMG1.5) that is incident on the earth's surface is reproduced. The photons that have an energy below the silicon band gap energy (1.12 eV), are thus lost due to non-absorption are highlighted in red. The area in red in Figure 1-3 accounts for over a third of all incident photons from the sun. This thesis will focus on possible ways to capture this lost portion of the solar spectrum for Si solar cells.

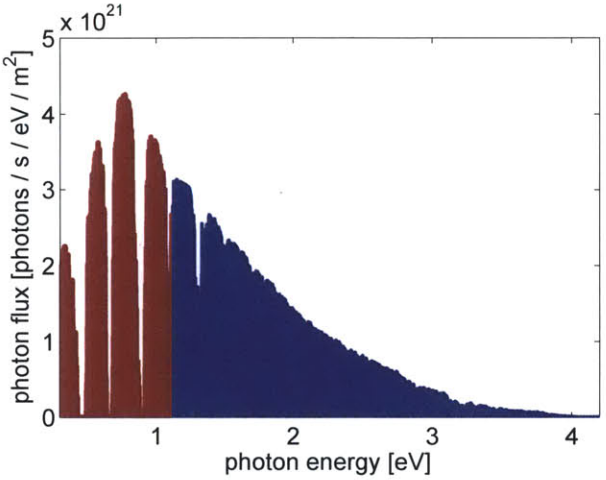

Figure 1-3: The AM1.5G solar spectrum is plotted above with non-absorbed photons in a silicon solar cell highlighted in red. These highlight losses account for over a third of the entire spectrum.

Thermalization Losses

After a photon creates a mobile electron and hole, the two charge carriers have an excess of kinetic energy. This excess energy is quickly lost to heat as the carrier runs into other silicon atoms and loses a portion of this kinetic energy to the silicon lattice as phonons. This process, known as thermalization, stops when the electron or hole's energy reaches the conduction band minimum or valence band maximum, respectively. This loss mechanism is shown in Figure 1-2 as process # 2, and the amount of energy lost per photon absorbed is approximated as the difference between the photon energy and the band gap energy. These losses are quite dramatic for

blue light in a Si solar cell; a blue photon has an energy that is bout 3 times larger than the silicon band gap, and thus only about two thirds of that photon's energy is lost to thermalization. For red light, only about a third of the energy is lost to thermalization. If we look at the entire solar spectrum, on average about 60% of a given photon's energy is lost to thermalization in a Si solar cell.

1.3 High Efficiency Concept: Intermediate Band Solar Cell

For the single junction device described in the previous section and displayed in Figure 1-2, the conversion efficiency of sunlight into electricity is limited primarily by the two factors discussed in the previous section, thermalization and non-absorption. The thermodynamic limit of a single junction photovoltaic device, the Shockley-Queisser limit [129], takes into account these losses, as well as a few other loss mechanisms that are not mentioned here (radiative recombination and junction losses). There are many strategies to overcome this fundamental limit. One is to stack multiple single junction devices with different band gaps on top of each other, often referred to as a multi-junction solar cell. Each layer is made of a solar cell with a different band gap; the largest band gap is used on the top layer and the bottom layer has the smallest band gap. This strategy reduces the losses of both thermalization and non-absorption. Non-absorption losses are reduced because below-band gap light that passes the top layer can get absorbed by a subsequent layer with a smaller band gap. Thermalization losses are reduced because different band gap materials are used to capture different portions of the solar spectrum more effectively, the top layer which has a large band gap converts blue light efficiently, while the bottom layer which has a smaller band gap collects infrared light efficiently.

While multi-junction cells can achieve efficiencies (>40%) that exceed the Shockley-Queisser efficiency limit, they are often made using very expensive growth process and can be very complex to manufacture because the different absorber, window, and

buffer layers that need to be grown. A similar idea to a multi-junction is the intermediate band solar cell, which has a simpler device structure and consists of a single junction. In an intermediate band solar cell, a band of electronic states are introduced within the band gap of the material. This enables the generation of free-carriers using two photons with energy below the band gap; the first photon promotes an electron from the valence band to the intermediate band, then from the intermediate band to the conduction band.

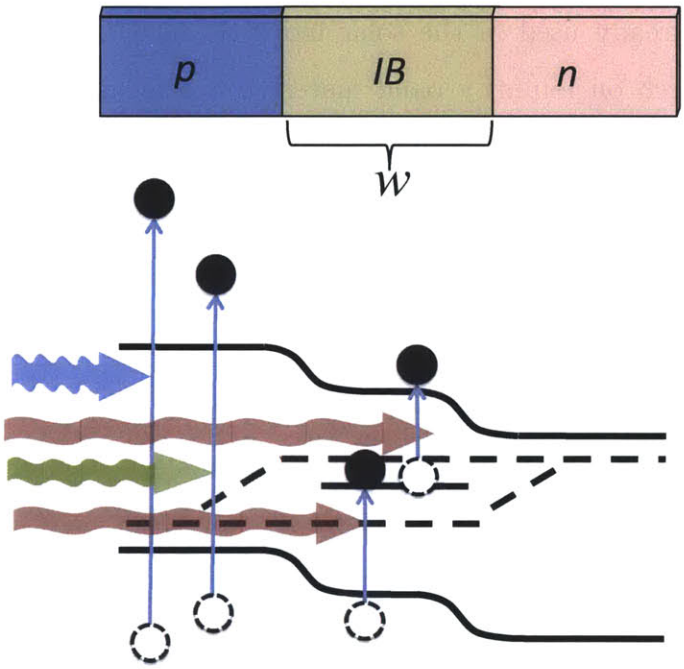

Figure 1-4: A p-IB-n planar device structure (shown above) and the corresponding energy band diagram (shown below) for an intermediate band solar cell.

An intermediate band solar cell has the advantage that the physical structure is simpler than a multi-junction device. Detailed balance calculations have revealed that this idea can outperform a two-cell multi-junction, often referred to as a tandem solar cell. Calculations by Luque estimate a 63% [73] maximum efficiency. With concentration, Bremner and Honsberg predict similar theoretical efficiencies under concentration: 65% [13].

The challenge to making intermediate band solar cells has been creating a material that has a band within it's band gap, as shown in Figure 1-4. There have been several proposed methods for creating an intermediate material. These methods include using quantum dots, [80, 79] highly mis-matched alloys, [127, 153, 71] or creating an impurity-band [63, 75, 74, 77].

This thesis will focus on impurity band materials, because they have the ability to be manufactured in large quantities and scale to TW levels of production. Both quantum-dot based devices and highly-mismatched alloys require special deposition and growth methods. However, impurity band materials can be made using methods and tools that are already used in the solar industry, such as ion implanters and laser melting. Research on impurity band materials has focused on finding appropriate dopants that can be used to form a band of electronic states within the band gap as well optimizing methods for incorporating these dopants at supersaturated concentrations.

1.4 Impurity Band

Using deep-level impurities is one way that has been proposed to create an intermediate band material. In fact, it was one of the first proposed method of overcoming the detailed balance limit of p-n junction solar cell, as it was mentioned in the original paper by Shockley and Queisser [129]. Below is an excerpt from their original paper:

> An example of a new area in which a detailed balance treatment is needed is the proposal that a solar cell may be improved by adding traps to it to absorb the longer wavelength radiation.

To create the band structure described in Figure 1-5 and reference [73], we can introduce impurities with energy levels within the band gap. In normal silicon solar cells, deep levels lead to increased recombination via Shockley-Read-Hall recombination (SRH) [130, 44], and thus a decreased efficiency. However, if the recombination activity of these impurities is inherently low, or can be suppressed via a theoretical

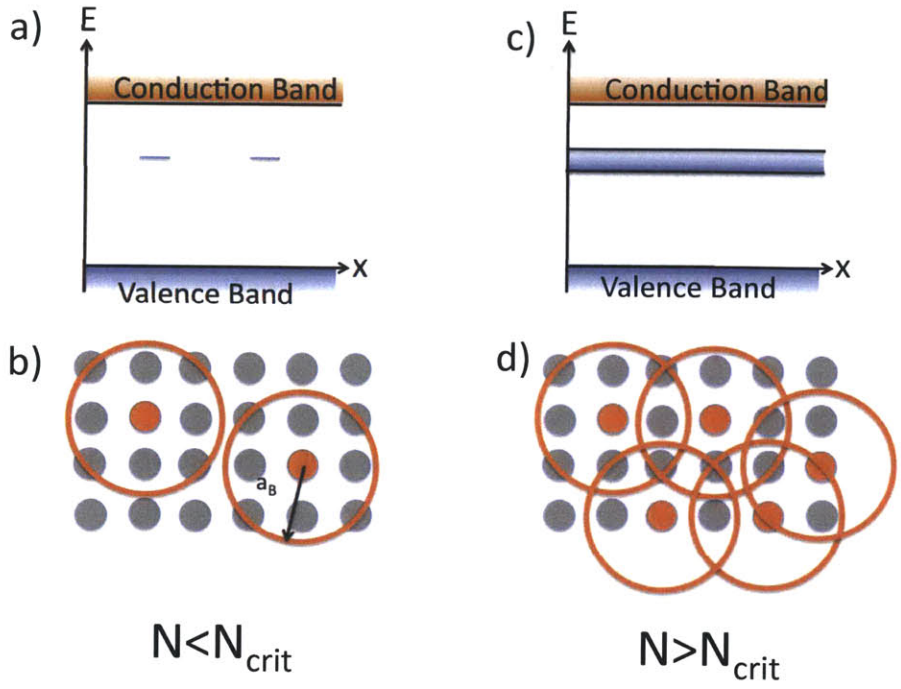

Figure 1-5: The band diagram for deep-level impurities in a semi conductor are shown in (a) and (c) for concentrations below and above the IMT critical concentration. A 2-D representation of the silicon lattice is shown in (b) and (d). These deep level donor or acceptor states have wave functions that have some finite radius, which is represented by the orange circles of radius, a_B. At concentrations above the IMT, the radii overlap, as shown in (d). At concentrations below the IMT, these wave functions do not overlap, and the donor/acceptor electrons/holes are strongly bound to their impurity nucleus, as shown in (b). The IMT described in this figure is known as a Mott transition.

mechanism called "lifetime recovery" [74, 77], then a solar cell that utilizes an impurity band material can potentially break the thermodynamic efficiency limit for a single band gap material[129].

Lifetime recovery is a theory that describes how to suppress the recombination activity of these deep-level impurities. Lifetime recovery theorizes that SRH recombination via deep-level impurities is suppressed when the impurity concentration exceeds the critical concentration for metallic impurity band formation [74]. On an energy band diagram, deep-level impurities at dilute concentrations create energy

states that are very localized in real space, as shown in Figure 1-5a. At very low concentrations, electrons or holes that exist at these energy levels are trapped, or immobile. A 2-D representation of the silicon lattice is shown in Figure 1-5b, where the silicon atoms are represented by grey dots, and the impurity atoms by orange dots. The deep-level electron or hole maintains a strong Coulombic attraction to the impurity atom and is bound by a radius, a_B. Alternatively a_B can be thought of as the acceptor/donor hole/electron's wave function, which is localized to the impurity atom. If these deep level impurities are incorporated at sufficiently high levels, these donor/acceptor wave functions begin to overlap and become delocalized, as shown in Figure 1-5d. This transition is known as an insulator to metal transition (IMT), where the donor/acceptor electrons/holes are no longer bound to their impurity atom, and a metallic impurity band forms (see Figure 1-5c). It has been theorized that at impurity concentrations above the IMT, when a metallic impurity forms, non-radiative recombination will be suppressed; this idea is often referred to as "lifetime recovery" [74, 77]. However, this theory has not been successfully reduced to practice, and the subsequent subsection discusses the empirical work to date on this theory.

One of difficulties in testing this hypothesis of lifetime recovery is physically incorporating impurities at concentrations high enough to drive an IMT. Generally, this IMT critical concentration exceeds the equilibrium solid-solubility limit. One type of IMT is known as a Mott transition, and is the transition described in the previous paragraph and in Figure 1-5. As described previously, this type of transition occurs when donor or acceptor wave functions begin to overlap, which occurs when the impurity concentration reaches some critical threshold, N_{crit}.

$$N_{\text{crit}}^{1/3} a_{\text{B}} = C_0 \tag{1.1}$$

In equation 1.1, the value of C_0 was predicted to be around 0.2 by Mott [84], but has empirically been shown to be 0.26 [29]. For a hydrogen-like donor, the Bohr radius, a_{B} can be approximated by the donor binding energy by:

$$a_{\mathrm{B}} = \frac{e^2}{2\epsilon_{\mathrm{r}} E_{\mathrm{d}}} \tag{1.2}$$

Both equations 1.1 and 1.2 are combined to yield an estimate of the Mott IMT critical concentration, N_{crit}. This theory works very well for shallow impurities and has been demonstrated for a variety of semiconductor:impurity systems, such as Si:P, Si:As, Ge:Sb, Ge:As, and Ge:P [3, 20]. Generally, this critical concentration exceeds the equilibrium solid-solubility limit for deep-level impurities. This trend is shown in figure 1-6, which plots the equilibrium solid-solubility for elements in Si as a function of their donor or acceptor binding energy [64, 22, 52, 78]. Generally speaking, the deeper the energy level that the impurity introduces in Si, the lower the solubility. One of the ways to create super-saturated solutions is a process called hyperdoping (which is explained in detail in chapter 2) and has been performed on a variety of elements in silicon to create these meta-stable alloys that are super-saturated with dopants [137, 101, 138, 110, 100, 109].

One of the major motivations for using hyper-doping is the ability to reach concentrations high enough to drive an IMT in hopes to test this lifetime recovery hypothesis. It is important to note that the Mott transition is not the only form of IMT, and may not describe materials described in this thesis, as will be discussed in subsequent chapters. Additionally, the estimate of a_{B} in equation 1.2, while quite accurate for shallow impurities, is currently untested for deep-level impurities. The plot shown in 1-6 is meant to show the trend that increased concentrations are necessary to drive an IMT for dopants with deeper levels. In fact, the IMT for both S and Se is considerably lower than the Mott critical concentration [147, 31]; however the IMT seen in chalcogen-doped Si may not be Mott-like, and the estimate of a_{B} may be inaccurate. From Figure 1-6, we can see that hyperdoping allows the incorporation of dopants at orders of magnitude above the equilibrium solid solubility limit.

Most of the work on impurity band materials has focused on characterizing the electronic, structural, and optical properties of hyperdoped materials. Almost all the work to date has been performed on Si:Ti [99, 4, 96, 122, 37, 100, 97, 98, 95, 35, 58,

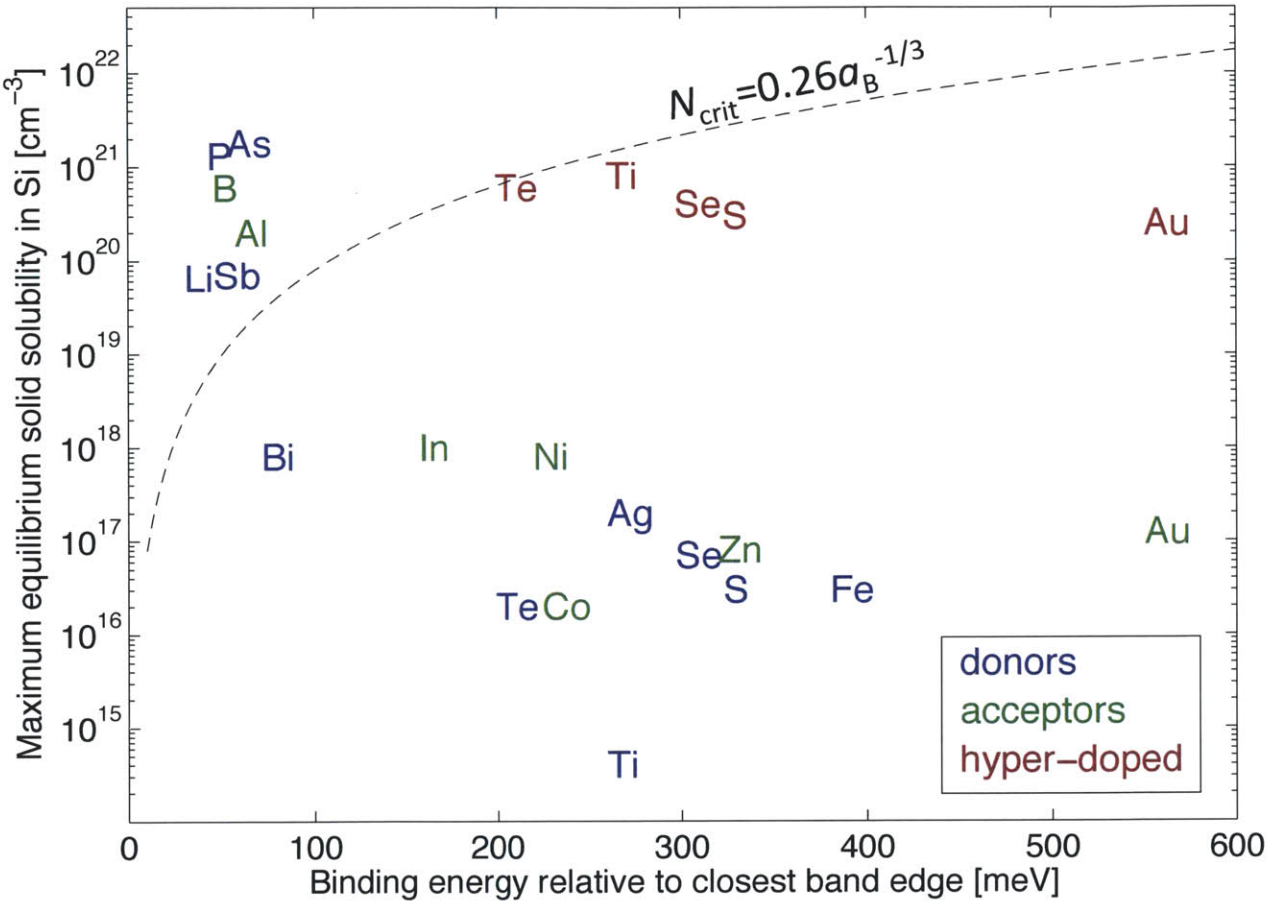

Figure 1-6: Equilibrium Solid solubility limits of different elements in silicon. Hyperdoping allows incorporation of dopants at beyond the equilibrium concentrations, resulting in meta-stable alloys. Thin dotted black line is the estimate for the Mott critical concentration using Equations 1.1 and 1.2.

102, 19] and Si:S [60, 105, 112, 111, 31, 135, 101, 106, 147, 32, 10]. The work has focused on identifying the electronic transport mechanisms at low temperatures to determine the critical concentration for an IMT [147, 31, 102], quantifying the sub-band gap absorption [35, 60, 135, 101, 10], measuring photo-conductance or photo-resonse of a diode [120, 112, 111, 105], or investigating the electronic band structure using fluorescence techniques [135, 105]. The only group to demonstrate the two-photon process in an impurity-band material was in a ZnTe:O-based device [144, 143]; however the effect was very small.

Despite this large body of literature, there has been no definitive confirmation of lifetime recovery and no high-efficiency solar cell devices have been fabricated. The next section discusses the current state of the literature surrounding lifetime recovery.

1.4.1 Lifetime Recovery

Empirical work on verifying the lifetime recovery theory has focused on the Si:Ti system. Lifetime measurements performed on wafers which had a thin (<200nm) layer of Si:Ti on its surface have shown an increasing measured lifetime with increasing Ti concentration [4]. However, these lifetime measurements did not directly measure the lifetime of the Si:Ti layer (the majority of photo-excitation was in the substrate), and only demonstrated an increasing lifetime with increased Ti concentration, and did not show the "recovery" when Ti concentrations exceeded the Mott limit [84]. Proper demonstration of lifetime recovery should be able to show two distinct impurity concentration ranges with two different trends in lifetime: (1) a concentration range described by Shockley-Read-Hall (SRH) recombination where lifetime decreases with increased impurity concentration and (2) a range of impurity concentration above a critical threshold where lifetime has improved with increased concentration (*i.e.* the recovery). The trend for lifetime in the low-concentration range is shown schematically in left of Figure 1-7; at concentrations below the IMT, defect states are isolated and lifetime decreases with increased impurity concentrations, as described by SRH recombination statistics [129]. At concentrations above the IMT, the trend with lifetime is currently unknown, as shown in the right of Figure 1-7. At concentrations

above the IMT, a steady increase or a discontinuous increase in lifetime would suggest that lifetime recovery is real, while the continued decrease in lifetime would demonstrate that lifetime recovery is not real.

Additionally, a critique has been published [58] that suggests these results from reference [4] may be misinterpreted and other unexplored effects may be affecting the lifetime measurements. More recent work on Si:Ti has made lifetime recovery claims similar to Reference [4] using low-temperature capacitive techniques [19]. However in Reference [19], no confirmation that the samples were single-crystal was presented; in previous publications by the same group, samples with high Ti concentrations produced in an identical manner were micro-crystalline [100, 95], and the electronic properties of these materials may have been dominated by these structural defects or metal precipitates that segregated into the crystal grain boundaries.

While there has been no definitive experimental work that has demonstrated lifetime recovery, recent theoretical work suggests that lifetime recovery is impossible and that even at dopant concentrations above the IMT lifetime will "not be significantly reduced from the independent dopant limit" [63]. Whether or not lifetime recovery exists, a photovoltaic device that incorporates an absorber layer with deep-level dopants can have an enhanced efficiency as long as the figure of merit of the impurity-band layer is sufficiently high. In the next sub-section, the figure of merit, which describes the efficacy for an impurity-band material, will be discussed and explained.

1.5 Figure of Merit for an IBPV Absorber Layer

Reference [63] describes in detail a figure of merit for an impurity-band (IB) photovoltaic absorber layer, but a brief description is reproduced here. This figure of merit is a dimensionless parameter that describes whether an IB materials can provide an efficiency boost over a conventional p-n junction solar cell when incorporated into a standard cell to form a p-IB-n device structure (see Figure 1-4). For an IB layer to be effective, it needs to generate both free electrons and holes from photons with

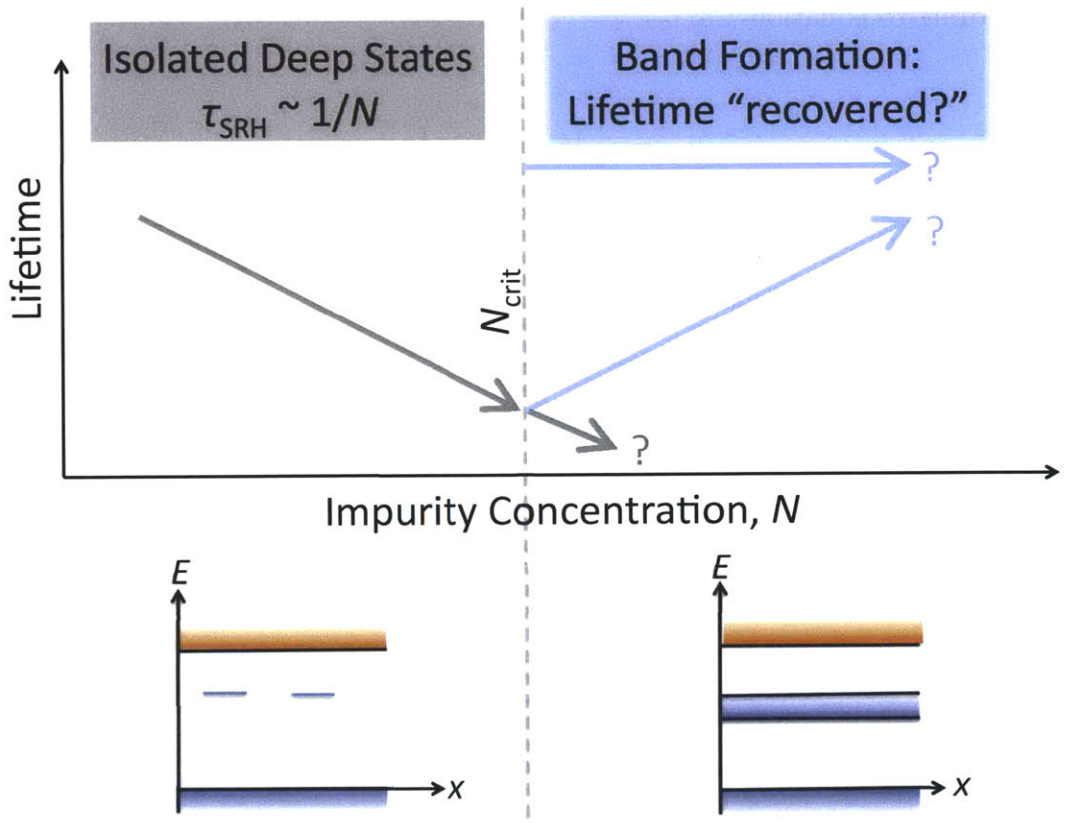

Figure 1-7: A schematic of how lifetime scales at different concentrations of deep-level impurities. At concentrations below the IMT, lifetime decreases according to SRH recombination. It is currently unexplored how lifetime scales at concentrations above the IMT; a steady or discontinuous increase in lifetime would be indicative of lifetime recovery (blue lines), while a continual decrease would indicate that SRH recombination still describes the recombination statistics (grey line).

energy below the band gap energy of the host semiconductor; these photo-generated electrons and holes then need to traverse the IB layer to their respective neighboring n or p regions prior to recombining. The figure of merit, $\nu_{e,h}$, describes the effectiveness of an IB material to generate and then transport electrons or holes into the n or p regions, respectively. The value of $\nu_{\mathrm{e,h}}$ must be calculated for both electrons and holes, according to equation 1.3.

$$\nu_{\mathrm{e,h}} = \frac{1}{c^2} V_{\mathrm{bi}} \mu_{\mathrm{e,h}} \tau_{\mathrm{e,h}} \alpha_{\mathrm{e,h}}^2 \tag{1.3}$$

The non-dimensional figure of merit, $\nu_{\mathrm{e,h}}$, describes the ratio of the recombination lifetime for electrons and holes, $\tau_{\mathrm{e,h}}$, to the transit time, $t_{\mathrm{e,h}}$, of electrons or holes to exit the IB layer. A successful IB material must have a carrier lifetimes, $\tau_{\mathrm{e,h}}$, that are longer than $t_{\mathrm{e,h}}$.

The power of this parameter is that it can be calculated from measured quantities for both types of carriers; this consists of electron or hole lifetimes ($\tau_{\mathrm{e,h}}$), electron or hole mobilities ($\mu_{\mathrm{e,h}}$), and the absorption coefficient for the generation of holes via VB-IB transitions (α_{h}) or electrons via IB-CB transitions (α_{e}). For a planar p-IB-n device structure, it is assumed that the built-in voltage, V_{bi} is providing an electric field across the IB that is sweeping electrons or holes that are photo-generated from sub-band gap light to neighboring n or p layers, respectively. The transit time for an electron or hole to escape the IB layer, $t_{\mathrm{e,h}}$, is therefore related to the mobility, $\mu_{\mathrm{e,h}}$, built-in voltage, V_{bi}, and IB layer thickness, w, by $t = w^2/(\mu V_{\mathrm{bi}})$. The IB layer needs to absorb the majority of the incident sub-band gap light, so it should be several absorption lengths thick, thus $w = c/\alpha_{\mathrm{e,h}}$, where c defines the IB layer thickness in number of absorption lengths.

Note that this figure of merit describes a drift-driven device; in a diffusion limited device the value of V_{bi} could simply be the thermal voltage, kT/q. Reference [63] suggests that a value of c=2-3 makes the IB layer sufficiently thick and that for the IB photovoltaic (IBPV) device to have a higher efficiency than a single junction device, it must have $\nu >> 1$. The majority of this thesis will focus on evaluating

ν for the Si:S system from experimental measurements. When incorporating an IB materials into a photovoltaic device, it must have a sufficiently high figure of merit; however this is not the only requirement, and further criteria are described in the next section.

1.6 Requirements for an Impurity Band PV Material

The requirements for a impurity band material to provide a boost in efficiency when incorporated into a *p-n* junction device, the material must have the following properties:

1 An impurity band must be separate in energy from either the VB or CB [76].

2 Low energy photons must be able to promote both from the VB to the IB, and from the IB into the CB in order to create both electrons and holes in the CB and VB, respectively [68].

3 The figure of merit, $\nu_{\mathrm{e,h}} = \frac{1}{c^2} V_{\mathrm{bi}} \mu_{\mathrm{e,h}} \tau_{\mathrm{e,h}} \alpha_{e,h}^2$, which describes an IB material's ability to both generate carriers via sub-band gap photons and transport these carriers out of the IB before recombining, must be sufficiently high. The material must possess a $\nu >> 1$ for both electrons and holes generated via IB$\rightarrow$CB and VB$\rightarrow$IB transition, respectively.

If any one of these requirements is not met, then the material is not a candidate IBPV material. It is important to note that this list is not exhaustive, and even if a material system passes each all of the above requirements, this is not sufficient to claim that will enhance the conversion efficiency when implemented into a *p-n* junction solar cell, and demonstration in a full working device is the only way to demonstrate an efficiency enhancement.

1.7 S-doped Si as a candidate Impurity Band Material

S-doped Si at supersaturated concentrations has been studied extensively for over a decade, and one of its potential applications has been IBPV. While the properties and background of this material system will be given a more thorough treatment in the next chapter, a brief introduction with it's relevance to IBPV will be given here.

S is known to exhibit deep levels within the band gap [53], and based on optical absorption and low-temperature transport data is a candidate for an IB absorber layer. Using hypderdoping, supersaturated concentrations of 0.5% atomic S have been attained in single-crystal Si [137]. At these hyperdoped concentrations, samples exhibit strong sub-band-gap absorption where over half of the incident light below band gap light (0.5-1 eV photons) are absorbed in a layer that is less than 350 nm thick [25, 60, 148, 135]. In one instance (although this result has not been reproduced), photodiodes made from S-doped Si exhibit strong detectivity at photon energies below the band gap of Si [16]. Additionally, metallic conductivity at very high S concentrations is observed, [147] which is a promising indication of the formation of a dopant-induced metallic band. However, the IMT seen in Si:S may be attributed to a degeneracy of the IB and CB at high concentration instead of the formation of a metallic impurity band within the gap, and this will be further discussed in Section 2.6.

In this thesis, the list in Section 1.6 will be used to evaluate the Si:S and it's potential to create an IB PV device. Experimental techniques described in this thesis will be used primarily to evaluate both criteria #1 and #3 for Si:S. In chapter 3, x-ray emission spectroscopy will be used to study the band structure of Si:S at different doping concentrations and annealing temperatures. In chapter 4, we'll use optical spectroscopy to determine the position and bandwidth of the S-induced IB as a function of S concentration. Finally, transport measurements in chapter 5, and the optical measurements in chapter 4 allow estimation of ν_e for IB$\rightarrow$CB transitions in Si:S. The measured value of ν_e for Si:S is deemed to low for IBPV applications.

Chapter 6 presents a new methodology for choosing candidate IB to study materials using information known about the semiconductor:impurity system at dilute concentrations.

Chapter 2

Previous Work on S-doped Si

In this chapter, we'll discuss the past work done on S-doped Si. A lot of early work focused on doping Si with S using thermal processes, which meant that the maximum attainable S concentrations was limited by the equilibrium solid solubility limit of 5×10^{16} cm^{-3} [131]. Recent work has focused on using a process known as hyperdoping, which allows for the creation of meta-stable alloys that are super-saturated with S dopants.

2.1 S-doping at Dilute Concentrations

Some of the earliest electrical and optical work was done by Carlson [17] on samples which were annealed for several days at 1200°C in the presence of S in an evacuated glass tube, thus saturating the samples with S. Carlson identified deep levels introduced by S in Si using both Hall measurements and spectrally-resolved photoconductivity measurements. Carlson confirmed that S acts as a donor in Si and found trap energies in the ranges of 0.2-0.4 eV. Further optical characterization by Krag done at low temperature identified both ground and excited state energies of both neutral and singly ionized S atoms [62]. Once models were developed for the photoionization optical cross-section for deep levels in a semiconductor, the most cited being the Lucovsky's formula [72], past research focused on fitting spectrally resolved photoconductivity data to trap energies [116, 92, 126, 30, 107]. Utilizing photoionization of

deep-level impurities, many researchers focused on making photodetectors that were responsive to sub-band gap light, but were unsuccessful at getting photoresponse for temperatures above 95K [126, 82, 46].

The most definitive work to date on S-doped Si was performed by Grimmeiss and Janzén [41, 40, 53], who used deep-level transient spectroscopy (DLTS), low-temperature optical absorption measurements, and low-temperature photoconductivity. Grimmeiss and Janzén compiled these results to empirically determine and categorize all the ground and excited electronic states of sulfur for different atomic configurations in a Si lattice. Low temperature photoconductivity and DLTS determined the energy difference between the ground state of a S donor and the conduction band minimum. A figure from Reference [53] is re-produced in Figure 2-1. S, which is a double-donor in silicon, has different binding energies for both neutral (S^0) and singly-ionized (S^+) single-substitutional defect states, as shown in Figure 2-1. Note that the ionized donor site has a larger binding energy which is a result of increased Coloumbic attraction between the ionized core and the second donor electron. Similar trends are found for the S dimer (S_2^0 and S_2^+) and various other complexes of S in Si ($S_C^0(x_i)$ and $S_C^+(x_i)$). Many of the excited states related to these S-centers were measured using optical spectroscopy (mainly Fourier transform infrared spectroscopy). Most of these excited state transitions were found to be less than 50 meV [53] from the conduction band for S^0. Many of these methods employed to understand the optoelectronic properties from of S in Si at dilute concentrations will be used in this thesis, mainly photoconductivity and FTIR optical absorption measurements.

2.2 S-hyperdoping of Si: Survey of Fabrication Methods

Two methods have been developed to hyperdope Si with S and create supersaturated solid solutions. Both involve using very short pulses of laser light to melt the surface; after melting, the rapid cooling of the Si surface is able to outpace kinetics of segre-

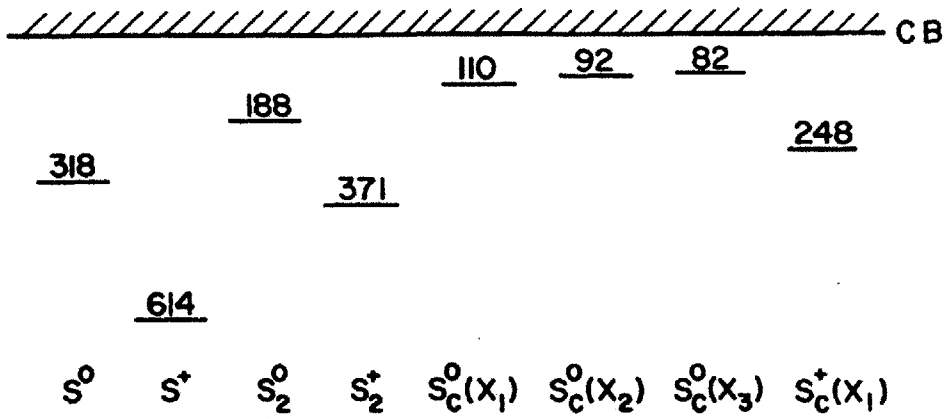

Figure 2-1: The different binding energies relative to the CB minimum for different S donor complexes in meV. Figure reproduced from Reference [53].

gation and yield a supersaturated solid solution. The first method involves rastering femtosecond-laser pulses over a silicon surface in the presence of SF_6 that results in a surface that is made up of conical spikes [48, 148, 128]. The resultant physical structure of this surface layer is a mix of amorphous pockets and small crystalline grains [25]. Infrared photodiodes made using this method of S-hyperdoping have resulted in devices that possess detectivities comparable to commercially available Ge photodiodes [16].

The second method uses S ion implantation followed by a nanosecond-laser pulse. The laser pulse consists of a large, homogenized beam that melts the surface that then recrystallizes into a smooth, specular surface that is supersaturated with S dopants. This method of ion implantation followed by pulsed laser melting (PLM) will be the only hyper-doping method used to fabricate samples in this thesis. Because PLM material is single crystal and free of extended defects, it makes accurate electronic and optical characterization possible, which is why it was studied in this thesis. The PLM fabrication method is capable of making surface layers that are supersaturated with dopants at concentrations well above the equilibrium solid-solubility limit because the resolidification speed is much faster than the kinetics of segregation and

the resolidification front can effectively "trap" solutes at high concentrations in the solid solution. An excellent overview of the kinetics of this process can be found in Reference [6]. Additionally, References [109, 113, 61, 151] provide a nice overview of experimental results that verify the kinetic model.

2.3 Sample Fabrication Employed in this Thesis

Hyperdoping with S is performed as a multi-step process, outlined figure 2-2. First S ions ($^{32}S^{+}$) are implanted into the surface of a silicon wafer. If the S dose is below 3×10^{15} cm^{-2}, then Si^{+} is implanted at 85 keV at a dose of 3×10^{15} cm^{-2} to amorphize the surface prior to S implantation. This is done to ensure that the subsequent laser processing is always performed on an amorphous surface, regardless of starting S concentration. Additionally, because the stopping depth of S ions in silicon is different for amorphous and crystalline Si, pre-amorphizing also ensures that the S concentration depth profile has the same shape for all samples of different S implant doses. Si substrates used in this thesis are p-type (10-20 $\Omega-$cm, double-side polished, 700 μm thick, Czochralski-grown, and <100> orientation). The implantation of $^{32}S^{+}$ is done at 95 keV, which results in an implant depth of around 100nm. The implanter ion gun is angled at 7° off normal incidence to prevent channeling. This implantation creates an amorphous, S-rich surface layer.

Next, the laser melting is performed using a XeCl excimer laser, which delivers short pulses (25 ns at full width at half maximum, 50 ns total duration) of 308 nm light to the surface of the sample. The light pulse is homogenized so that the intensity of the light pulse is spatially uniform over a 2×2 mm^2 area.[1] This laser pulse melts the surface of the sample to a depth that is below the region that is damaged by the sulfur implant (around 350-400 nm.) This molten region then epitaxially re-solidifies at rate between 1-10 m/s. This rapid re-solidification is fast enough that it is able to outpace segregation kinetics and trap S atoms at concentrations that exceed the

[1]Less than a 5% root-mean square intensity variation is measured using a CCD camera that images the beam intensity of the XeCl laser.

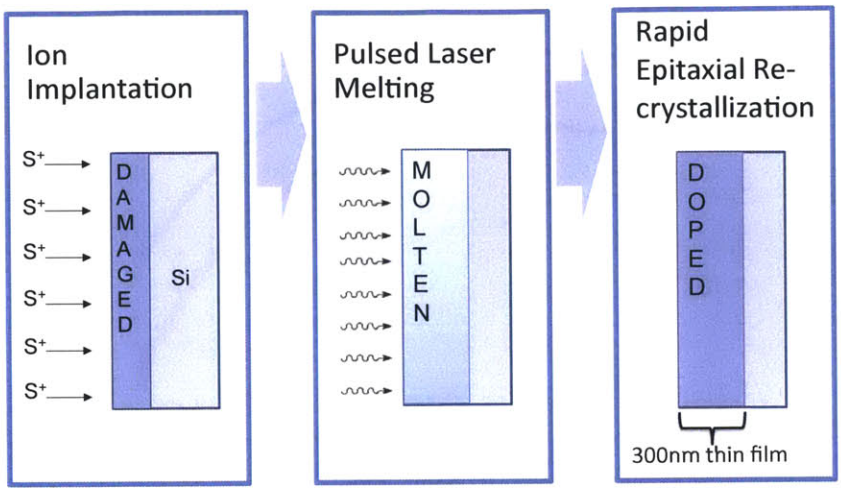

Figure 2-2: A schematic of the pulsed laser melting (PLM) method used to hyperdope Si with S.

equilibrium solid solubility limit; additionally, it is also slow enough to allow epitaxial solidification. Four consecutive laser pulses (fluences of 1.7, 1.7, 1.7, and 1.8 J/cm^2) are used to create a S profile that is relatively uniform for the first 200 nm from the surface, and then the next 150 nm contains a smoothly decrease in S concentration. Secondary ion mass spectrometry reveals the S concentration as a function of depth in Figure 2-3 for different S implant doses. More information and details on the fabrication procedure of these materials can be found in Reference [137].

2.4 Physical Structure

S-hyperdoped Si fabricated using PLM is single crystal, optically flat, and free of extended defects [7, 113]. Lattice resolution cross-sectional transmission electron micrographs (xTEM) revealed that the S-hyperdoped surface layer is single-crystal [137, 60]. An xTEM image from [137] is reproduced in Figure 2-4. The PLM technique has a history of producing crystalline materials that are supersaturated with dopants. For a damaged amorphous surface layer, when the laser pulse is sufficiently short and the melt is sufficiently deep so as to melt down to the crystalline, un-altered

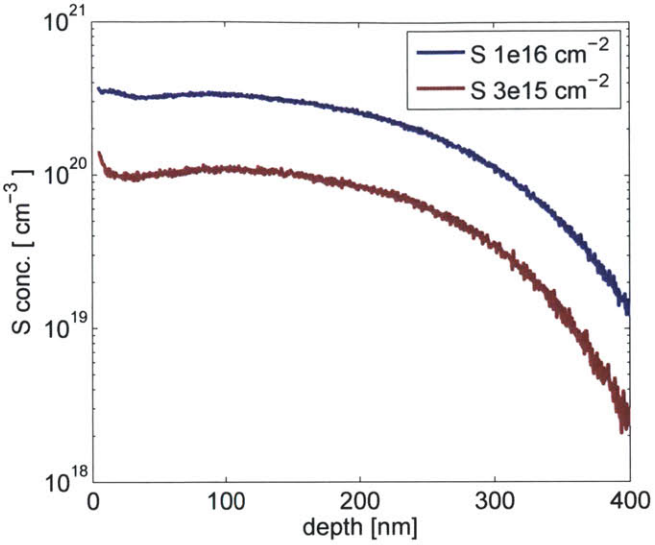

Figure 2-3: S concentration as a function of depth for different S implant doses into Si.

substrate, the resulting structure is single crystal and free of extended defects [88, 89, 151, 152]. The only observed extended structural defects in PLM materials results from a process called cellular breakdown. Cellular breakdown is characterized by the formation of large precipitates and formation of a high density of structural defects, and is easily detected using electron backscatter diffraction (EBSD) and happens when the liquid/solid interface becomes unstable during the re-solidification process. Cellular breakdown can occur when dopant concentrations get too high. The samples prepared in this thesis via PLM have been fabricated using identical methods found in previous literature [101, 137]; this past work [101, 137] used EBSD and xTEM to verify that samples were single crystal and had not undergone cellular breakdown.

The one type of defect that may be present in these samples are interstitial point defects or vacancies. Both xTEM and EBSD would not spot these. Point defects were studied using Rutherford bascattering in channeling mode (c-RBS). During these measurements, minimum backscattered yield from c-RBS measurements demonstrated that the ratio of random atoms to aligned was 4%, compared to 2.5% for a non-implanted sample [137, 60]. The backscatter yields could be reduced to that of a non-implanted sample if annealed at 550° C, which indicates that there is likely a

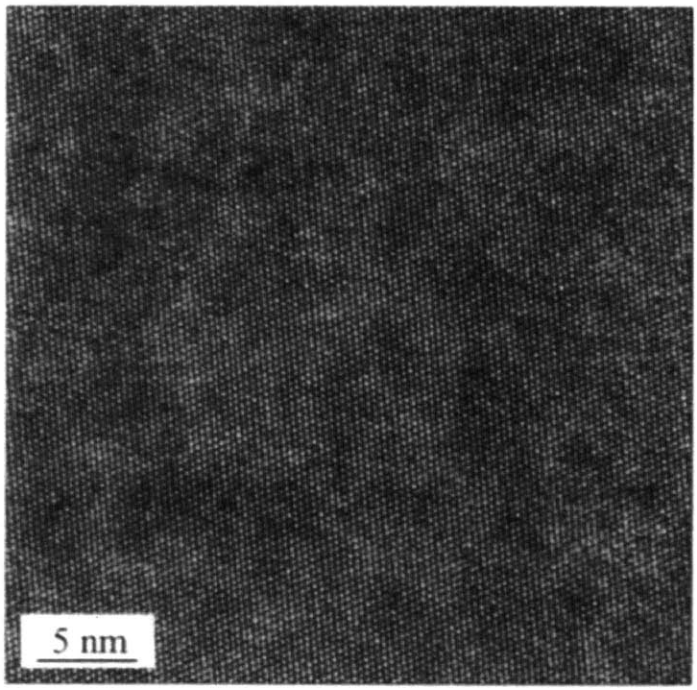

Figure 2-4: An xTEM image from Reference [137] that displays the S-implanted region after PLM and confirms single-crystallinity of samples after PLM processing.

presence of point defects (possibly interstitials) that exist after PLM.

2.5 Optical Absorption

One of the first measured properties of S-hyperedoped silicon was the optical absorption, and emphasis was given to photon energies below that of the silicon band gap. Measurements of both reflection, R_{m}, and transmission, T_{m}, down to photon energies of 0.5 eV demonstrated anomalously high absorption for photons with sub-band gap energies, as shown in Figure 2-5. At the highest S implantation dose (1×10^{16} cm^{-2},) over a third of the incident photons with energies measured below the band of silicon gets absorbed in a layer that is less than 350 nm thick [10, 60]. The sub-band gap absorption roughly scales linearly with S concentration [10].

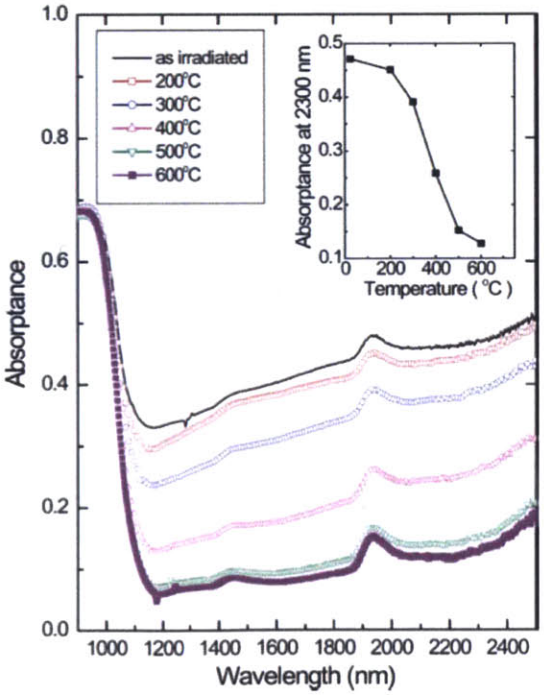

Figure 2-5: Strong sub-band gap absorption is deactivated with annealing. Note that bumps in data are an artifact of the measurement. Figure reproduced from Reference [60].

Because these S-hyperdoped Si samples are super-saturated, they are meta-stable. Annealing deactivates the sub-band gap absorption, and it has been speculated that this is due to precipitate formation [142]. In figure 2-5, the absorptance, $A = 1 - R_{\mathrm{m}} - T_{\mathrm{m}}$, is plotted as a function wavelength for S-hyperdoped samples that have been annealed at different temperatures. Note that the data in 2-5 has some features at 1450 and 1900 nm, which are due to a failure to normalize the data with an appropriate baseline reflectance standard. This has been corrected in subsequent publications [135].

The sub-band gap absorption seen in S-hyperdoped Si is attributed to a transition of a S-donor electron being promoted to the CB [123]. Because S is a double donor in Si, each S atom introduces two electronic states (a spin-up and spin-down state,) which are both occupied by the two donor electrons. This means that it is likely that there are few unoccupied states in the S-induced impurity band[2] (IB) that would allow a VB to IB transition. This has been studied theoretically using density-functional theory (DFT) [123], which enables calculation of the absorption strength of different optical transitions involving a S-induced impurity band (IB). The DFT study also looked at counter-doping (adding B or Al) to partially deplete the S-induced IB. At a 1:1 ratio of S:B and S:Al, the VB to IB transition was negligible, but the strength of the IB-CB transition was significantly reduced. The relevant data from reference [123] is reproduced in figure 2-6.

2.6 Electrical Transport and Doping

Temperature-dependent Hall measurements performed by Winkler yielded the mobility and sheet carrier concentration of the electron majority carriers as a function of S implantation dose [146]. The data from Winkler's thesis are reproduced in figure 2-7. These transport measurements indicate that PLM treatment of a Si surface that has received a S implantation dose of 1×10^{16} cm^{-2} (and has a peak S concentration of

[2]Note that impurity band here does not necessarily mean a metallic band where electrons and holes are mobile at zero temperature. An impurity band here is defined as a range of electronic energy levels that are introduced by a deep-level impurity (such as S.)

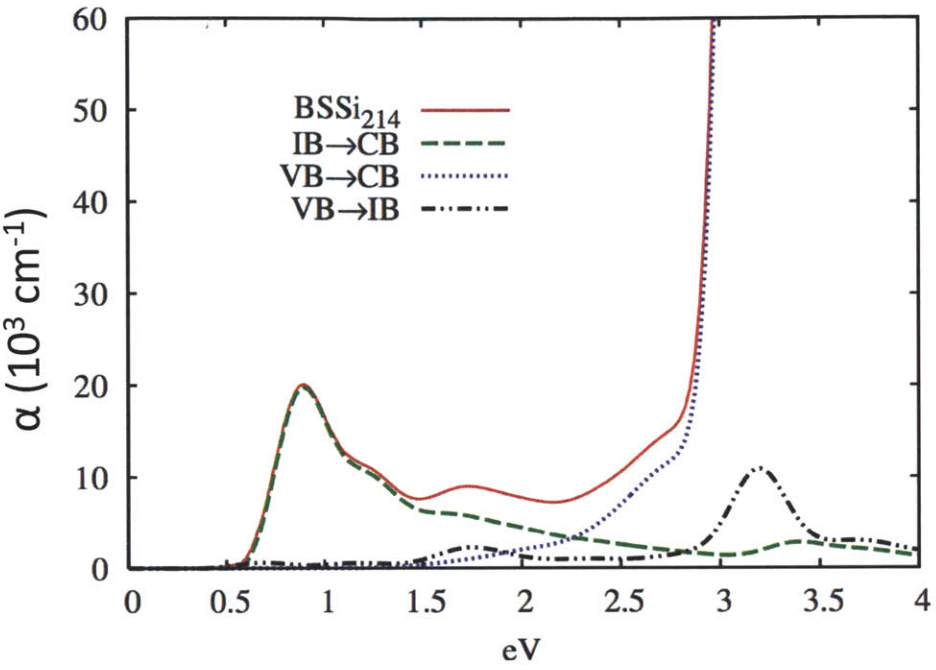

Figure 2-6: DFT-calculated absorption strengths of VB→IB and IB→CB transitions for Si that is both doped with equal amounts of S and B. Figure reproduced from [123].

3.8×10^{20} S cm^{-3} yields a doped region that is metallic (i.e. conducts at zero temperature). This is best understood upon inspection of the temperature dependence of the sheet resistance in figure 2-7, where at low temperature only the 1×10^{16} cm^{-2} dose sample maintains a constant resistance with decreased temperature. Sheet carrier concentration measurements from Hall effect also indicate that there is no carrier freeze-out for the metallic sample which received a 1×10^{16} cm^{-2} dose. While these measurements are only performed down to a temperature of 22K, additional sheet resistance measurements taken down to below 2K indicate that an implantation dose 1×10^{16} cm^{-2} does create a metallic layer [147].

The 3×10^{15} cm^{-2} dose sample does not exhibit a carrier freeze-out at temperatures below 50K as measured by Hall effect; however, despite this fact, the sample is indeed an insulator as its conductivity trends toward zero at zero temperature. At

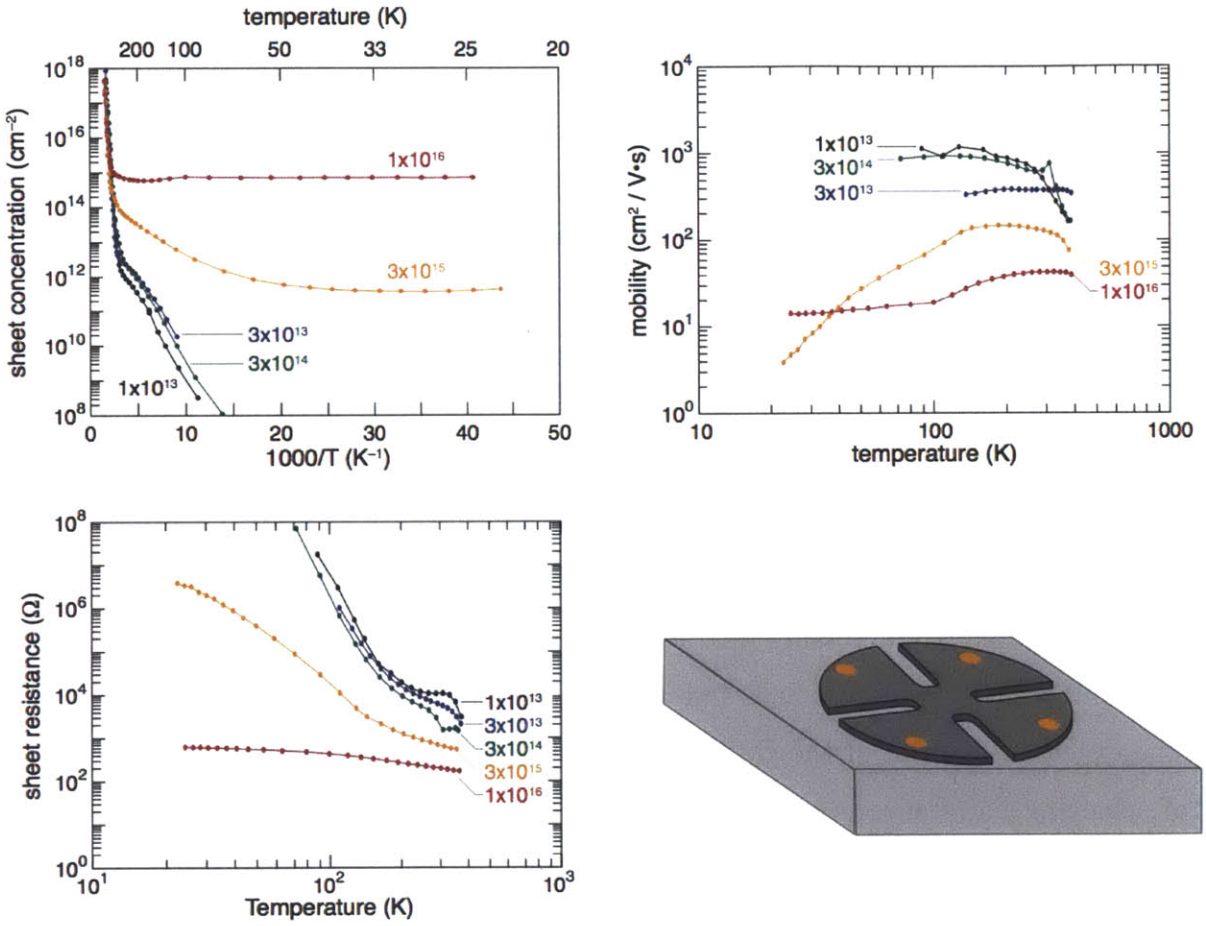

Figure 2-7: Temperature dependence of the electronic transport properties for Si doped with S at different implantation doses. The sample geometry used for Hall measurement is shown in the bottom right. Figure is reproduced from Reference [146].

low temperature, the transport in the 3×10^{15} cm^{-2} sample is dominated by hopping conduction [85, 49, 103, 86] and explains the seemingly anomalous temperature dependence of sheet carrier concentration and mobility from the Hall measurements. Hopping conduction describes the process of charge transfer between localized energy regions that are within the band gap, and has also been referred to as "impurity band conduction" [23]. The probability of hopping, or moving from one localized energy trap state to another neighboring one, is a function of several things, but the most relevant parameters are the distance between localized trap states, temperature, and the availability of empty traps. As localized trap states get closer together, the probability of hopping to an adjacent state increases, which is why this behavior is only seen in the insulating sample with the highest concentrations . The process is often described as a thermally-activated tunneling, which is why the mobility of the 3×10^{15} cm^{-2} sample decreases with decreasing temperature in the low-temperature regime where hopping conduction dominates.

While this transport data is a promising indication that a metallic S-induced IB has formed within the band gap of silicon at a dose of 1×10^{16} cm^{-2}, the IMT seen may be due to a band crossing (*i.e.* a merging of IB and the CB). DFT predicts that the IMT seen in Se-doped Si is indeed a band crossing [31], as seen in figure 2-8. The exact mechanism of the IMT is only important when discussing the prospects of achieving lifetime recovery. If the IMT is due to a band crossing, then the band structure becomes unsuitable for IBPV, and lifetime recovery is not possible in these materials.

2.7 Photoexcitation and Carrier Recombination

A lot of work has tried to create IR photodiodes on Si hyperdoped with S using the PLM process to replicate the detectivity reported by Carey *et al.* [16]. Thus far, no significant sub-band gap photo-response has been seen in these materials. Measurements on photodetectors [120] and photoconductivity measurements [111, 105] have not seen sub-band gap response that is above the noise floor of these measure-

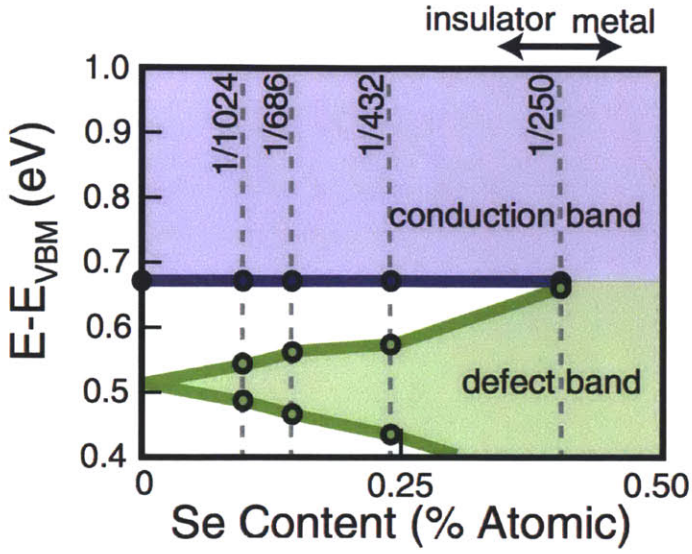

Figure 2-8: The energetic position and width of the impurity band as a function of Se content in Si as calculated by DFT [31].

ments. Photoconductivity measurements performed on silicon on insulator wafers for S-hyperdoped material did not yield a response at photon energies below the band gap of silicon [106]; based on the noise floor of this measurement, an upper bound on the mobility lifetime ($\mu_e \tau_e$) product of electrons promoted from S-donor states into the conduction band was estimated to be $< 1 \times 10^{-7}$ cm^2/V. Chapter 5 of this thesis will focus on the methods and strategies for measuring the photo-excited transport properties of these S-doped PLM materials.

2.8 Conclusion

S donors in Si at dilute concentrations are very well characterized and understood; the chemical state of donors, the binding energy of donor electrons, the photoionization cross-section are all well known for S in Si at low concentrations. However, when research in preparation for this thesis began, very little was understood about how these different properties would change at supersaturated, or hyperdoped concentrations. This thesis aims to explore these changes and relate them to photovoltaics.

Chapter 3

Band Structure Studied by X-Ray Emission Spectroscopy

While the electronic structure of Si:S was well understood at dilute concentrations, the electronic structure at hyperdoped concentrations was not well understood. To study the electronic structure of S-hyperdoped Si and understand how it changes with S concentration and annealing temperature, X-ray emission spectroscopy (XES) was used to study the electronic structure of S-hyperdoped Si.

XES is a synchrotron-based method that effectively images the partial occupied density of states (DOS) of a material. The technique was used to look at the S-induced donor electronic states within the band gap of Si. Emission features above the VB maximum are seen and their relation to the presence of the S dopants is established. These spectra also show a discrete change in the electronic structure of the material when the S concentration exceeds the critical concentration for the IMT, and are correlated with the strength of the sub-band gap absorption.

3.1 Introduction to XES

One of the advantages of this technique is that it is a photon-in, photon-out process; this means that it is much less surface sensitive than techniques that are photon-in, electron-out such as x-ray photoemission spectroscopy (XPS) and ultra-violet photoe-

mission spectroscopy (UPS). In these XES measurements, the combined attenuation length of the incoming and outgoing photons is 30 nm at 45° incidence [47]. In comparison, the inelastic mean free path of electrons detected in XPS or UPS measurements would be less than 1nm [108]. Traditional XPS and UPS experiments on these materials have not been able to probe beneath the surface oxide, which is why XES was used.

During an XES measurement, soft x-rays from a synchrotron source irradiate the sample. The incident x-ray energy is high enough to either promote an electron from a core level into an unoccupied electronic state or eject it from the material (excite into the continuum), as shown in figure 3-1a. This photonic promotion of a core electron leaves behind a core hole, and the subsequent relaxation of a VB electron into that core hole releases a photon, as shown in figure 3-1b. The spectral intensity of the emitted photons is related to the partial occupied DOS.

XES measurements can take the form of non-resonant (XES) or resonant inelastic x-ray emission spectroscopy (RIXS). In a non-resonant measurement, the excitation source energy is able to eject core electrons into the continuum. During a RIXS measurement, the excitation source is controlled and swept over different energies that promotes electrons from a core state into the conduction band. Additionally, integrating the entire emission spectrum as a function of excitation energy, is a technique called x-ray absorption spectroscopy (XAS), and is a way of probing the unoccupied density of states (i.e. the CB). Essentially, each XAS data point is the integration along a slice of a RIXS map taken at a specific excitation energy.

In these measurements, the core levels of interest are the $2p_{\frac{1}{2}}$ and $2p_{\frac{3}{2}}$ electrons, which have binding energies between 99-100 eV [141]. The $2p_{\frac{1}{2}}$ core level has a binding energy that is 0.6eV larger than the $2p_{\frac{3}{2}}$ level [69]. This effect is known as "spin orbit coupling". The fact that these core levels are split, means that "echoes" will appear in the emitted spectrum; an electron of a given energy in the valence band can either fluoresce to the $2p_{\frac{3}{2}}$ core hole, or it can fluoresce to the $2p_{\frac{1}{2}}$ core hole and emit a photon that is 0.6 eV higher in energy. The emission from the occupied VB states into the $2p_{\frac{1}{2}}$ and $2p_{\frac{3}{2}}$ holes are known as "Si $L_{2,3}$" emission.

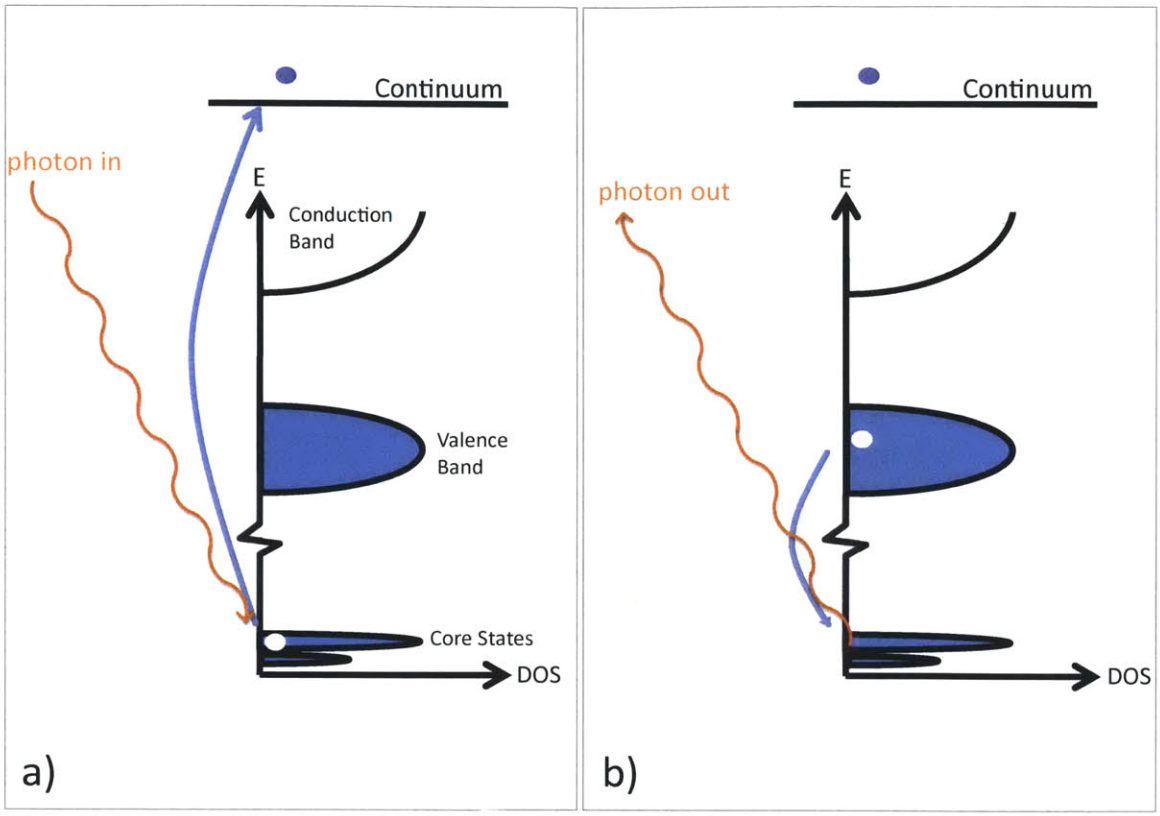

Figure 3-1: An overview of the absorption, then fluorescence processes involved in XES are shown above. First, soft x-rays promote an electron from the core state into an unoccupied state (a). In this excited state, a valence band electron recombines with the core hole and releases a photon (b). The spectra of the emitted photons yields information about the occupied partial DOS of the sample.

3.2 Sample and Experimental Details

Samples are prepared using the methodology described in section 2.2. The ion implantation doses used for sample fabrication are listed in table 3.1. The sample which did not receive a S implant will be referred to as the "Si reference" sample. The Si reference sample was taken from a wafer that matched the specifications of the substrates of all samples (full description of substrate specifications is given in section 2.2). Two samples with the highest (1×10^{16} cm^{-2}) S dose were annealed for 30 min in an N2 atmosphere at 400° C and 900° C, respectively. The S concentration depth

profiles for two highest doses (3×10^{15} and 1×10^{16} cm^{-2}) were measured using SIMS. The peak S concentrations of the lowest two doses (3×10^{14} and 1×10^{15} cm^{-2}) were estimated using linear extrapolation from the highest two doses. Samples which have not been annealed will be referred to by their peak concentration and samples which have been annealed will be referred by their annealing temperature.

S Implant Dose [cm^{-2}]	Peak S Concentration [cm^{-3}]	Annealing Temperature		
		No Anneal	400° C	900° C
-	-	×		
3×10^{14}	1.4×10^{19}	×		
1×10^{15}	4.0×10^{19}	×		
3×10^{15}	1.2×10^{20}*	×		
1×10^{16}	3.8×10^{20}*	×	×	×

Table 3.1: Enumeration of the samples that are reported in this chapter. Peak S concentrations measured by SIMS are marked with an *.

The optical properties of all samples were measured using a spectrophotometer equipped an integrating sphere for wavelengths out to 2.5 μm. Both transmission, T_{m}, and reflection, R_{m}, were measured of each sample listed in table 3.1. For reflectance measurements, a silver mirror was used as reference standard.

XES measurements were performed at the Advanced Light Source, Lawrence Berkeley National Laboratory, using the soft x-ray fluorescence spectrometer at Beamline 8.0.1 [56]. The energy scale was calibrated by measuring elastically scattered Rayleigh lines at five energies across the measurement window. The excitation energy was calibrated by measuring the x-ray absorption spectrum of a Si reference.

Non-resonant XES measurements used an excitation source of x-rays with energy of 120 eV, which is enough energy to promote electrons from the silicon $2p_{\frac{1}{2}}$ or $2p_{\frac{3}{2}}$ core levels into the continuum. XES spectra were normalized by the integrated area of the spectra from 80-102 eV and setting the integral intensity to unity. To subtract noise from the detector, a linear background was fit to the high energy region where no emission should occur ($>$ 102 eV) and then subtracted from each spectrum.

3.3 Results and Discussion from Non-resonant XES measurements on Si:S

The spectral normalized absorptance, $A = (1 - R_{\mathrm{m}} - T_{\mathrm{m}})/(1 - R_m)$, of all the samples are shown in figure 3-2. Spectra for non-annealed samples (see Figure 3-2a) show that sub-band gap absorption increases with increased S concentration, which agrees with previous measurements [10]. Spectra for annealed samples which had received the highest sulfur dose (see Figure 3-2b) show that increasing annealing temperature decreases sub-band gap absorption, which is consistent with previous work [60].

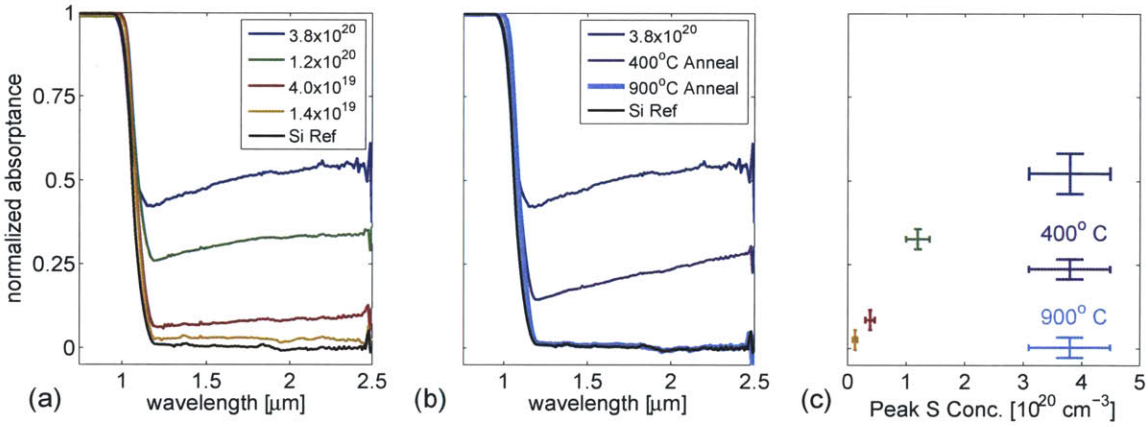

Figure 3-2: (a) Normalized absorptance for different peak S concentration and (b) for samples with the highest S concentration that are annealed at different temperatures. (c) The normalized absorptance is averaged over the wavelength range 1500-2500nm and plotted for all samples as a function of S concentration. Figure is reproduced from Reference [135].

Figure 3-3a shows the Si $L_{2,3}$ XES spectra of the Si reference sample and the 3.8×10^{20} S cm^{-3} sample over the entire energy range measured. The two VB spectra reveal that the high S-doping does not significantly affect the overall electronic structure below emission energies *ca.* 99eV. The peaks seen in the VB emission spectra for Si at ca. 89, 92 and 95 eV are generally attributed to valence bands having an s, s-p, and p symmetry, respectively [117]. However, major changes are seen in the emission spectra at energies above 99 eV. The region highlighted by the gray box in figure 3-3a is magnified in figures 3-3b and 3-3c which shows the emission originating from

states above the VB as a function of S concentrations and annealing temperature, respectively. The appearance of two sets of peaks above the VB edge is due to the Si 2p spin-orbit splitting of 0.62 eV [69]. The spectra in Figure 3-3b were measured at a shallower detector angle than those in 3-3c, resulting in an enhanced energy resolution for the former set.

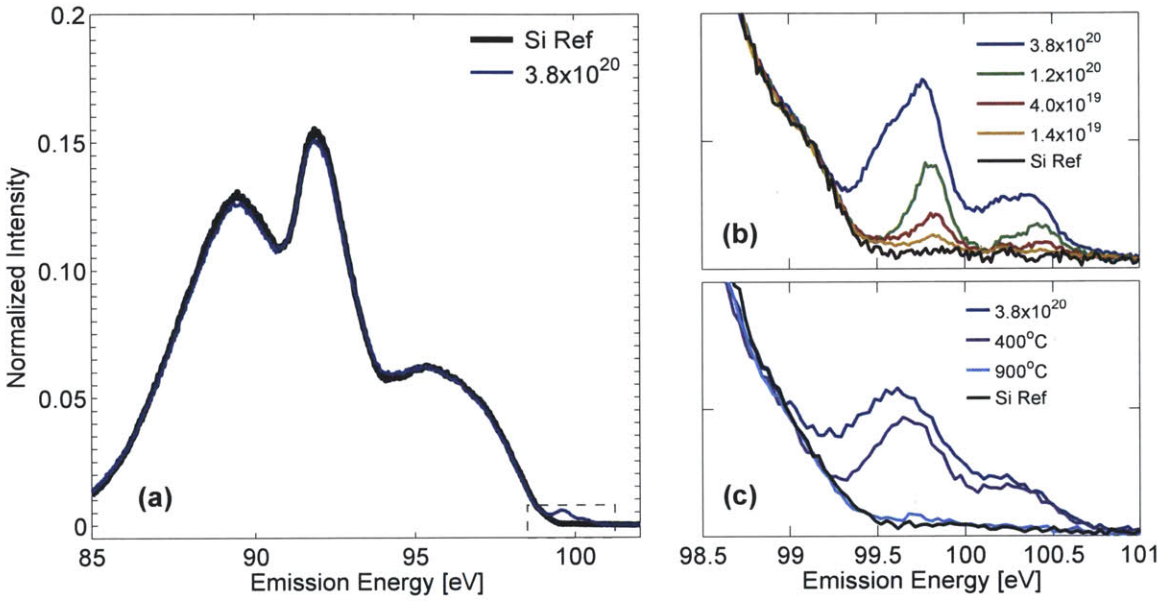

Figure 3-3: (a) Si $L_{2,3}$ XES spectra of the Si reference and a Si sample doped with S at a peak concentration of 3.8×10^{20} cm^{-3}. Magnified view of the emission seen above the VB maximum for samples of (b) varying concentration (in cm^{-3}) and (c) 3.8×10^{20} cm^{-3} S samples annealed at varying temperatures. Y-axes tick marks denote equal value changes. Figure is reproduced from Reference [135].

Voigt functions were fit to the XES spectra to quantify the independent contributions of the Si VB and the above-edge portions of the spectra, as shown in Fig. 3-4. Two Voigt functions (centered at 98.3 eV and 99.1 eV) were used to approximate the shape of the VB emission. Pairs of Voigt functions with a constant shape - FWHM of 0.27 eV, spin-orbit splitting of 0.62 eV - were used to approximate the above-VB emission features. The spectral energy width of the Voigt functions represent a convolution of the energy resolution of the detector, and the bandwidth of the 2p core levels. Excellent agreement of the fit can be achieved, suggesting that the spectra indeed only require one pair of Voigt peaks for satisfactory description,

with the exception of the highest concentration sample, which requires two pairs of spin-orbit-split Voigt peaks, with the second set centered 0.2 eV below the main peaks.

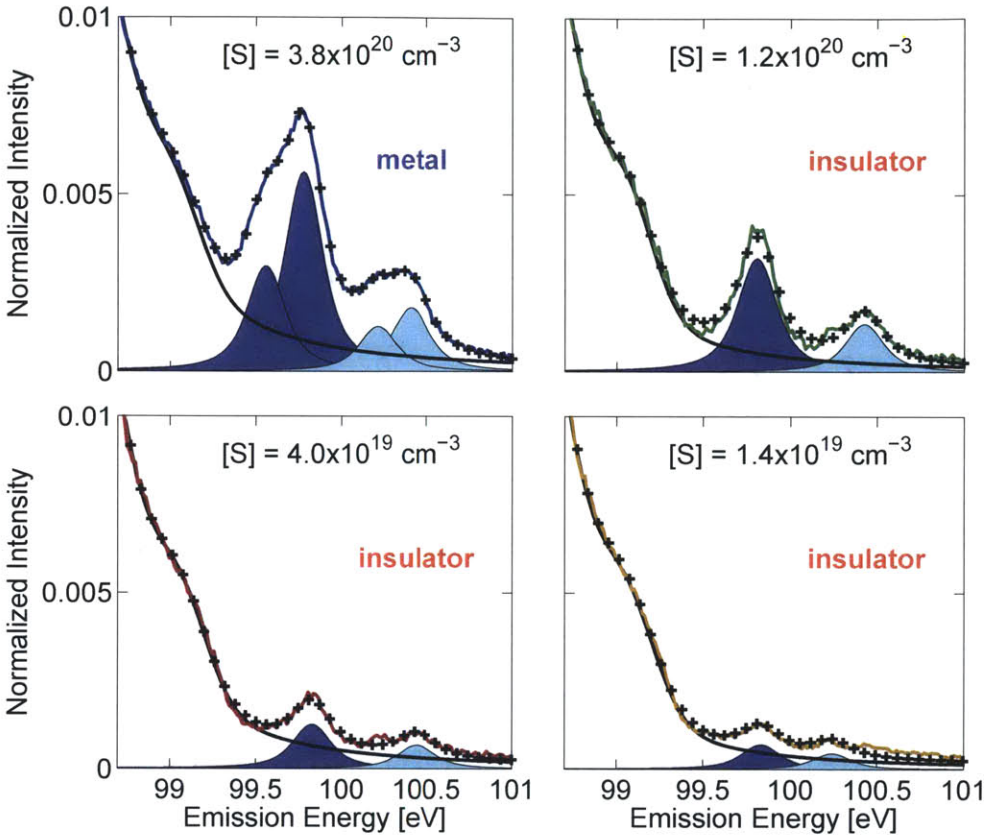

Figure 3-4: Si $L_{2,3}$ XES spectra from Figure 3-3b, along with Voigt-lineshape fits (black crosses). The VB emission fit is shown as a thin black line, and the S-induced emission features are shown as filled light and dark curves, representing L_2 and L_3 contributions, respectively. Peak S concentration is reported in the top right of each graph. The sample with S concentration above the critical insulator-to-metal concentration [147] is labeled "metal," while those below are labeled "insulator." Figure is reproduced from Reference [135].

Figure 3-5 shows that the area of the above-VB XES features increases linearly with S concentration. This trend indicates that the XES emission features are a result of the presence of S atoms in the Si samples. Additionally, XES measurements performed on a control sample (PLM-processed Si-implanted Si wafer) produced a spectrum that was indistinguishable from the Si ref., which is shown in figure 3-6.

Thus, we conclude that the emission features are not related to PLM-induced defects, but are a result of the S dopants.

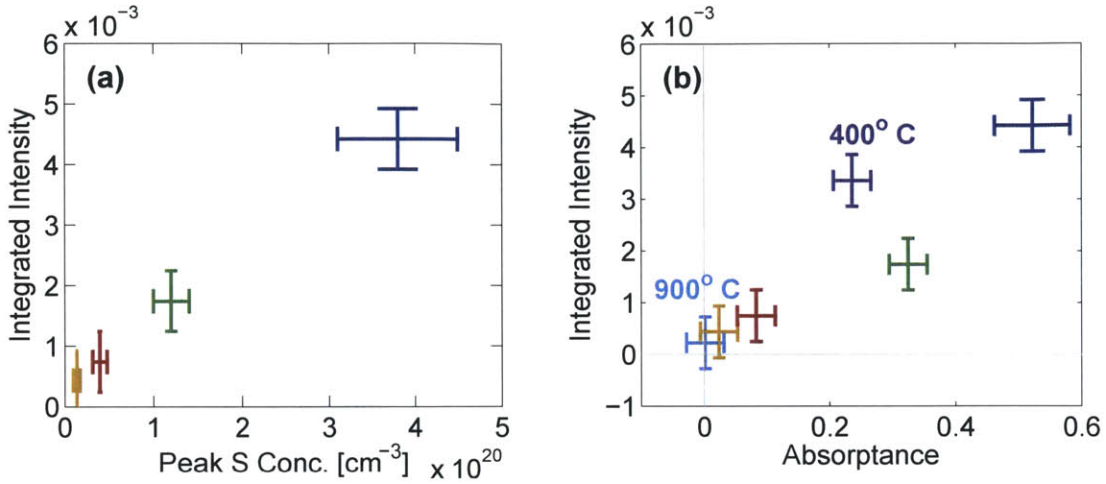

Figure 3-5: Area of the above-VB XES emission feature, plotted against (a) peak S concentration for samples of varying dose and (b) average normalized absorptance in the region from 1500 to 2500 nm. Figure is reproduced from Reference [135].

As the S concentration surpasses the critical value ($3.1 \pm 1.3 \times 10^{20}$ cm^{-3}) for the insulator-to-metal transition [147], the shape of the S-induced Si $L_{2,3}$ emission features changes. The spectra in figure 3-4 are labeled metal or insulator depending on whether their S concentrations lies above or below this critical value [147], respectively. The insulating samples (1.4×10^{19}, 4.0×10^{19}, and 1.2×10^{20} cm^{-3} peak S concentrations) all exhibit an L_3 XES peak centered around 99.7 eV that grows in amplitude, but not in width. However, the expected metallic sample (3.8×10^{20} cm^{-3}) exhibits an XES emission feature with a different spectral shape, and fitting requires a second pair of Voigt functions, as mentioned.

The intensity of the S-induced XES features not only correlates with the sulfur concentration, but also with sub-band gap optical absorption, as shown in Figure 3-5a. Previous work [137] demonstrated that thermal annealing deactivates sub-band gap optical absorption. Figure 3-3c shows a decrease in S-induced XES emission intensity with increasing annealing temperature, suggesting the features are related to sub-band gap absorptance. In Figure 3-5b, the relationship between absorptance and S-induced XES emission feature area is quantified for un-annealed and annealed 3.8×10^{20} S cm^{-3}

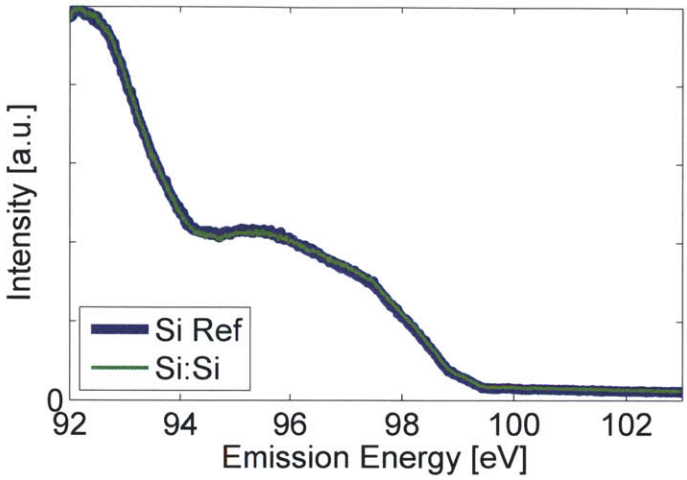

Figure 3-6: Si $L_{2,3}$ XES spectra of a Si-implanted Si sample and the Si Reference sample. The Si-implanted Si sample received an implant dose above the amorphization threshold and was subsequently re-crystallized using PLM.

samples. Figure 3-5b demonstrates that strong sub-band gap absorption correlates with strong above-VB XES emission features, with slight differences between the annealed and un-annealed samples.

SIMS data [110] indicate that anneals performed at similar temperatures and times do not change the S distribution at length scales greater than the SIMS depth resolution. Thus, the intensity decrease of the S-induced XES feature (see Figure 3-3c) is not due to S evaporation from the surface or diffusion into the substrate. Instead, it is suggestive of an annealing-induced chemical state change of S, which results in an electronic structure change. This is consistent with extended x-ray absorption fine structure studies of chalcogen-doped Si [91]. This theory will be explored further in Section 4.6.

3.4 Similarities in Electronic Structure of Si:S to Si:Se and Si:Te

Similar above-VB emission features are seen in samples that are doped with other chalcogens, as shown in Figure 3-7. The spectra shown in figure 3-7 are for samples

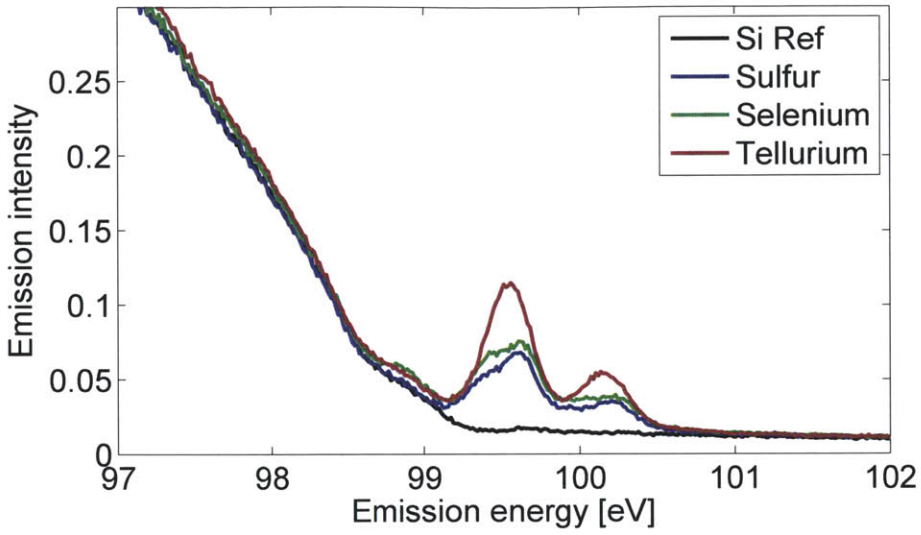

Figure 3-7: XES spectra of samples containing S, Se, and Te which all received the same atomic implant dose of the respective chalcogen atom at 1×10^{16} cm^{-2}.

which received implant doses of 1×10^{16} cm^{-2}. The Se and Te samples were implanted at energies of 176 and 245 keV, respectively. The Se concentration of the sample measured is known to be above that of the IMT critical concentration [31], which may explain the fact that the spectral shape is similar to that of the S sample, which is also at a concentration above the IMT. This is an indication that the electronic structures of the Se and S doped samples are similar. Currently the IMT critical concentration for Si:Te is unknown.

3.5 Possible Origins on Emission Features

While it is clear that the emission features seen are related to the presence of S, the exact excitation-relaxation process during XES measurement is unknown for these materials. There are a couple theories, described below, that can explain the presence of these emission features. The theories described below are not mutually exclusive and could both be at play during the excitation-relaxation process. The fact that two competing processes may result in these emission features complicates the analysis and prevents any direct relation between the S-induced DOS and the emission features

seen in XES.

3.5.1 Origin I: XES Images Occupied DOS

The first theory is the most obvious one: the emission features reflect the ground electronic state of the Si:S system. These feature intensities scale linearly with S concentration, indicating that they are induced by the S dopants. This linear scaling is also consistent with the theory that the emission is representative of the occupied DOS. We also see that sub-band gap optical absorption correlates with the above-VB emission under varying dopant dose and sample annealing conditions, as shown in Figure 3-5. The scaling of sub-band gap absorption with above-VB emission intensity is consistent with the idea that absorption is tied to deep levels introduced by S atoms.

The transition in spectral shape seen across the IMT is also consistent with this theory and can be explained by the IMT seen in this system, which results in the ionization of many S donors. Work done by Winkler [147, 146] indicate that the donor ionization ratio increases dramatically across the critical concentration for the IMT. Studies done at dilute S concentrations show that ionized S atoms introduce electronic states farther from the conduction band than those of neutral S (see Ref. [53] or Figure 2-1) and may thus result in lower-energy emission when probed via Si $L_{2,3}$ XES. Alternatively, the spectral-shape change could reflect a broader distribution of impurity states: as the inter-atomic distance between S-donors decreases, overlap of the S-donor electron wave functions increases. Increased wave function overlap may increase the bandwidth of electronic energy levels introduced by S dopants and could lead to a comparable broadening of the XES emission features. While both these theories are plausible, the latter is unlikely to be true. In the next chapter, we'll use optical measurements and see that there is indeed broadening of S-induced states at concentrations near the IMT, but these states move closer to the CB; in XES, a shift toward the CB would exhibit a peak shift toward higher energy, which contradicts the trend seen XES in Figures 3-3 and 3-4. Thus, the more likely explanation is that the emission of the sample with concentration above the IMT is that emission is occurring from ionized S atoms, which exhibit deeper binding energies [53].

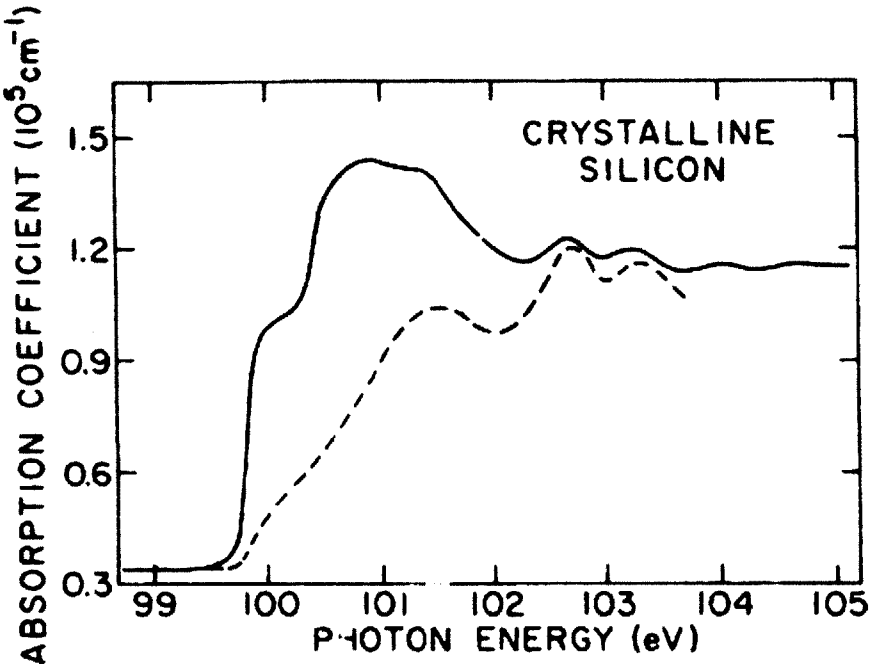

Figure 3-8: The measured $L_{2,3}$ XAS spectrum (solid line) is compared to a joint density of state calculation of the 2p core and the unoccupied DOS (dashed line). Figure is reproduced from Reference [15]. The sharp onset of the measured XAS spectrum is attributed to the presence of a core-exciton.

3.5.2 Origin 2: Dopant-enhanced Exciton Emission

Similar but weak emission features above the VB edge at similar energy have been observed previously in crystalline Si and were solely attributed to emission from a core-exciton [18, 132, 28]. In fact, the sharp onset of the Si $L_{2,3}$ XAS spectrum is attributed to an exciton and explains why XAS onset occurs at lower energy than is explained by the partial DOS of the CB. A figure from an article by Brown [15] which is reproduced in 3-8, highlights this discrepancy between theory and measurement; a comparison of the XAS spectrum of Si to the CB DOS concludes that the XAS edge rises much faster than the CB DOS. Essentially, the core-exciton is an emission feature that is not representative of the ground joint DOS of Si, but is merely an electronic energy state that exists in the presence of a core hole. These exciton

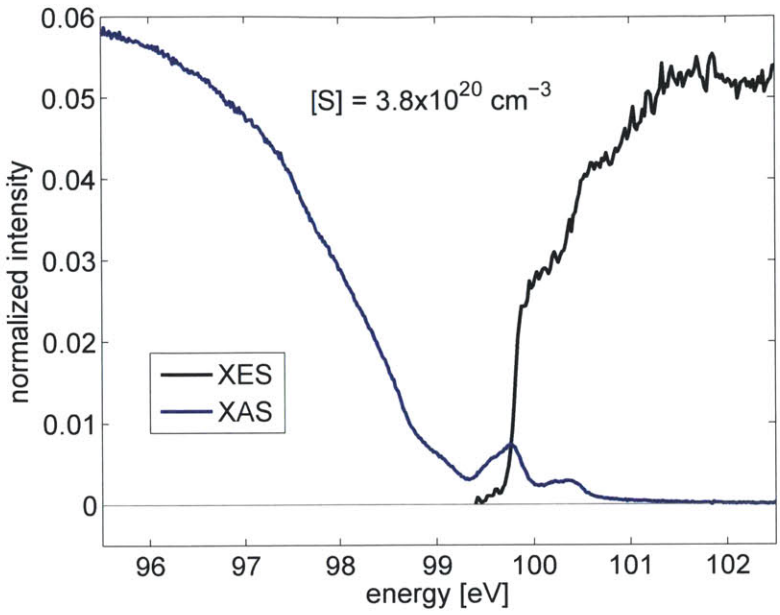

Figure 3-9: The XES and XAS spectra are shown for a Si sample with a peak S concentration 3.8×10^{20} S cm^{-3}.

emission features are considered to be intrinsic (*i.e.* are independent both of the excitation beam energy and intensity [18]). This intrinsic nature of the core-exciton makes it difficult to determine the root cause of the emission features seen in Si:S.

Measured XAS spectra for a Si sample containing 3.8×10^{20} S cm^{-3} show that the absorption onset of XAS occurs at a similar energy to the above-VB emission feature, as shown in figure 3-9. While the linear scaling between emission intensity and S concentration seen in figure 3-5a demonstrate the emission features are S induced, the influence of the core-exciton is something that cannot be excluded from the interpretation and may certainly have a large influence on the overall shape and intensity of these emission features.

3.6 Conclusions

While we can't extract an exact binding energy or image the occupied DOS from these measurements, they do indicate the presence of deep level states[1] introduced by S and that these states are indeed correlated with the sub-band gap absorption. We also see a discrete change in the electronic structure that is consistent with the IMT. Also, these measurements show that the overall VB structure was not substantially perturbed by the presence of S atoms at hyperdoped concentrations and provides further confirmation that these samples are indeed crystalline.

There are many difficulties in using XES to understand the band structure of this material and trying to extract binding energies or a DOS of the S-induced electronic levels. This is primarily because of the presence of a exciton in both the emission and absorption spectra, and the spin-orbit coupling. Due to the excitonic nature of the XAS absorption edge and it's enhanced onset to lower energy, it is difficult to determine the energy of the CB edge from an XAS spectra. Additionally, locating the position of the VB edge is difficult because of the spin orbit coupling that yields emission the superposition of the L_3 and L_2 spectra. The energy resolution of the technique is rather limited, and at its best is around 150 meV (due to a combination of the detector energy resolution and the emission bandwidth due to lifetime broadening). This energy resolution is on the order of the binding energies expected for S in Si, which means that no meaningful binding energies can be extracted. Additionally, the excitation-relaxation process in the Si $L_{2,3}$ emission may be influenced by the presence of a core-exciton, and work continues by my colleagues (acknowledged below) who are trying to determine the role excitons play in these emission features using hard X-ray photoemission spectroscopy and RIXS.

[1]This statement is confirmed by recent, unpublished hard X-ray photoemission spectroscopy studies and the optical measurements performed in the next chapter.

3.7 Acknowledgements

The work presented in this chapter is part of a large collaboration that spans an ocean. Joseph Sullivan conceived of the experiments, with initial help from Bonna Newman. Regan Wilks, Marcus Bär, Clemens Heske, Lothar Weinhardt, Dan Recht, Mike Aziz, and Tonio Buonassisi all helped with data analysis. Dan Recht and Aurore Said performed PLM to fabricate samples. Lothar Weinhardt, Clemens Heske, Yufeng Zhang, Monika Blum, Regan Wilks, Stefan Krause, Wanli Yang, Clemens Heske, Marcus Bär, and Joseph Sullivan all contributed to the acquisition of measurements at the synchrotron.

Chapter 4

Understanding Band Structure Through Optical Measurements

4.1 Motivation

In this chapter, optical spectroscopy methods will be used to determine absorption coefficient, α, for Si:S and understand the position and bandwidth of the IB at different S concentrations and annealing conditions. Fourier Transform Infrared spectroscopy (FTIR) is used to measure both the reflection and transmission of light through various samples, and the optical parameters are extracted using a thin film optical model. In these experiments sub-band gap light promotes electrons from the IB to CB (see figure 4-1b), and analyzing the strength of that transition for different photon energies can tell us both the position and width of the IB. The latter information is relevant because increased S concentrations can lead to IB broadening, as depicted in figure 4-1a, and discussed in section 2.6. If there is too much broadening, then the IB merges with the CB, and the material is no longer useful as an IBPV absorber layer.

The results from this chapter will serve two purposes. First it will determine α as a function of photon energy, which we can use to understand the band structure and width of the IB as a function of doping concentration. Based on this information, we can choose the S concentration range which still maintains a separation between the IB and CB. Second, these measured values for α will be used to estimate ν_e

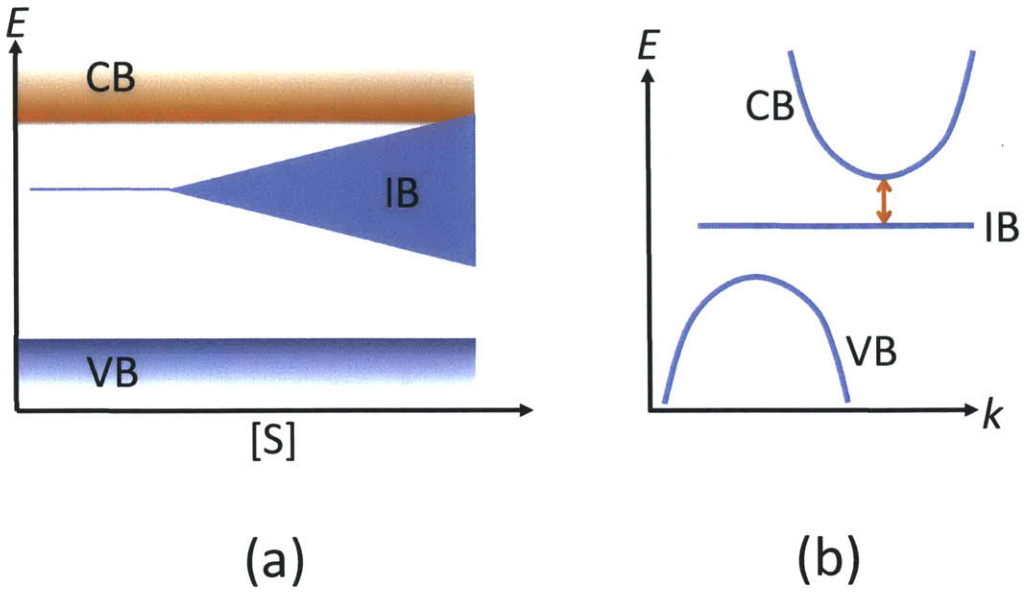

Figure 4-1: (a) A schematic of the energy band diagram illustrating the broadening of energy levels introduced by the S atoms at increasing S concentration, and (b) the transition excited during FTIR measurements shown on an E vs. k diagram.

(see section 1.5 and equation 1.3) and determine the future potential of this material system for IB PV applications.

4.2 Experimental Methods

Samples were made in the manner described in Section 2.2. A sample consisting of the same silicon wafer but without the S implanted layer is used as an optical reference to determine the complex index of refraction of the substrate, and will be referred to as the "Si substrate" sample. This sample was fabricated by taking a S-implanted wafer and etching off more than 1 μm to remove the implanted sulfur region using a reactive ion etcher; after etching, the surface remained optically smooth and remained a specular reflector.

A set of samples which received S implantation dose of 1×10^{16} cm^{-2} and had a peak S concentration of 3.8×10^{20} cm^{-3} were reserved and annealed at different temperatures. They were annealed in a rapid-thermal annealer for 100 seconds in an

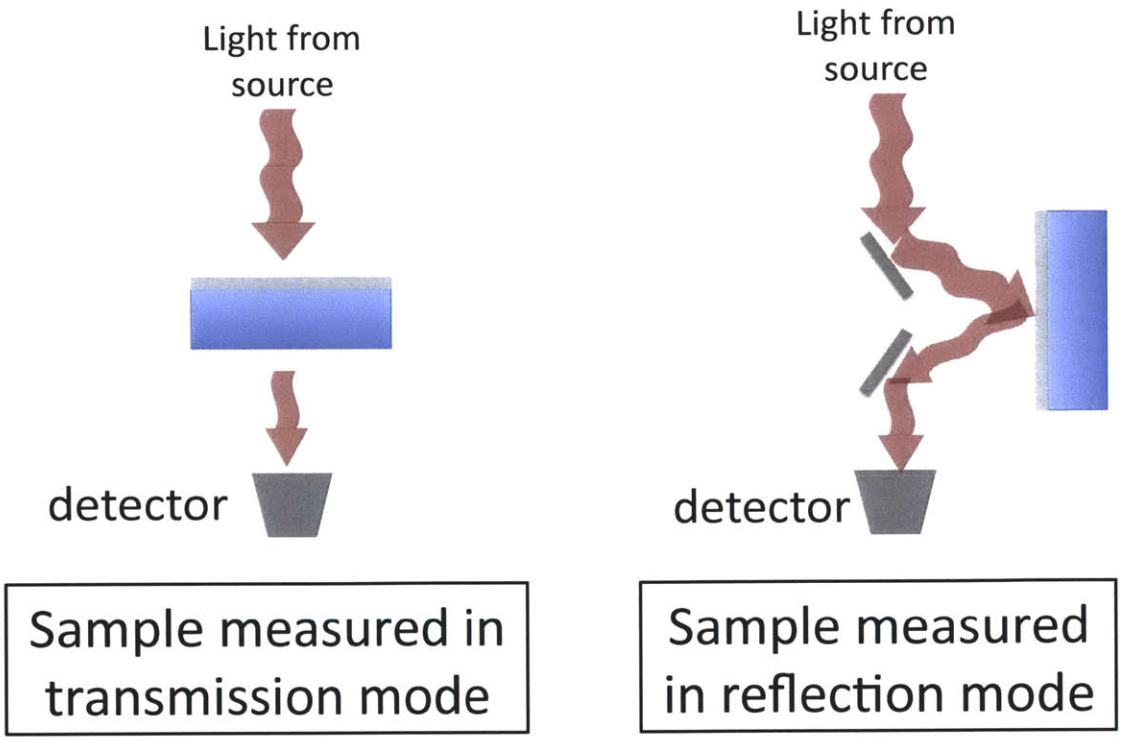

Figure 4-2: A schematic of the measurement setup for FTIR in both transmission and reflection modes are shown on the left and right, respectively. Mirrors are used to direct the beam in reflection mode. The angle of incident light is 12° in reflection mode. In the samples above, the thin hyperdoped layer is shown in grey, and the substrate is shown in blue.

Ar atmosphere at temperatures of varying from 500-900 K.

The measurements performed in this chapter utilized a Perkin Elmer Lamda 950 FTIR, and were performed in both transmission and reflection mode. During transmission measurements, the S-rich surface was facing toward the source at a normal angle. During reflection measurements the samples were measured at 12° incident angle from the incoming beam. See figure 4-2 for a schematic of the measurement. Both reflection and transmission measurements represented here are the result of 50 consecutive scans averaged together (both the sample scan and the background scan.)

The beam from the IR source in the FTIR is greater than 2 cm in diameter. Because the S-doped region is only a 2×2 mm^2 area, apertures were used to appropriately measure the S region. For the transmission measurements, a thin piece of Al sheet metal with a 1.5×1.5 mm^2 square removed was used as an aperture. For reflectivity measurements, the aperture (which was supplied by the OEM) was a

diffusely reflecting plastic disk. During a reflectivity measurement, any light that gets reflected off the aperture and into the detector distorts the measurement and falsely increases the measured reflectivity from the true reflectivity; thus the aperture disk is designed to be diffuse to limit the amount of spurious light that gets reflected off the aperture into the detector.

A piece of polished Si with 100 nm of e-beam evaporated Au was used as a reflectance standard. While silver can make an excellent standard, deposited silver without a protective coating can tarnish over time, which reduces the mirror's reflectivity at low photon energies. Protected mirrors have a protective coating that reduces reflectivity at long wavelengths and are unsuitable for FTIR measurements. While Au is not a suitable standard for optical measurements in the visible spectrum, it is suitable for the measurements presented here, where wavelengths of 1400 nm and above are used.

Samples were thoroughly cleaned before measurements to ensure that no organic residues were affecting the measurement. First samples went through a Piranha etch (3:1 solution of sulfuric acid and hydrogen peroxide) to remove any organics. Then samples were placed in 10% HF solution to remove the oxide formed during the previous acidic etch. The samples were then rinsed in DI water and thoroughly dried using a N_2 gun. This cleaning process was found to be necessary to get repeatable results.

Only samples without any surface damage were used for these measurements. If scratches were found on a sample, an alternate was acquired. Because these measurements were not performed with an integrating sphere, the samples must be completely specular reflectors to accurately measure all reflected and transmitted light. Any diffuse component of the reflectivity or transmissivity would not be captured in the measurement. The same standards were applied to the Au reflectance standards.

4.3 Extracting $n + ik$ from Measured Values

To extract the optical constants for this material, an optical model for the sample is developed. The models presented in this section simulate the FTIR measurements and extract the complex index of the hyper-doped Si layer from the measured values of R_{m} and T_{m}. The models account for reflections from the front and back surfaces of the sample, absorption in the Si substrate, and utilizes thin film Fresnel equations to describe the optical interaction in the hyperdoped layer. The front surface is modeled as a multi-layer stack of graded index to account for the S concentration variation. To obtain the optical properties of the hyperdoped surface region, two sets of transmission and reflection measurements are required; one set is performed on a Si substrate without any S on the surface to determine the optical properties of the underlying substrate, and the second set of measurements is performed on a sample with the hyperdoped surface region present. Figure 4-3 and 4-4 provides a schematic of the optical interactions that are accounted for in the model. The complex index ($\tilde{n} = n + ik$) of air, the hyper-doped layer at peak S concentration, and the substrate are denoted $\tilde{n}_1$, $\tilde{n}_2$, and $\tilde{n}_3$, respectively. Air is assumed to be a constant index of unity, and non-absorbing, thus we set $\tilde{n}_1 = 1$. However, for completeness of the equations, the index of air is still referenced in its complex form, $\tilde{n}_1$, in the following equations.

Additional background is given in this chapter to aid any future researchers who wish to perform this analysis. An excellent reference on modeling thin film optical measurements is provided in Orad Stenzel's *The Physics of Thin Film Optical Spectra* (2005).

4.3.1 Thick Absorbing Slab

In this sub-section we will derive the equations that describe the measured quantities of transmission, T_{m}, and reflectance, R_{m}, through a thick slab of material, which are depicted in Figure 4-3. This analysis is necessary to extract the index of the substrate, $\tilde{n}_3 = n_3 + ik_3$. The slab is assumed to be absorbing and is specularly reflecting on both

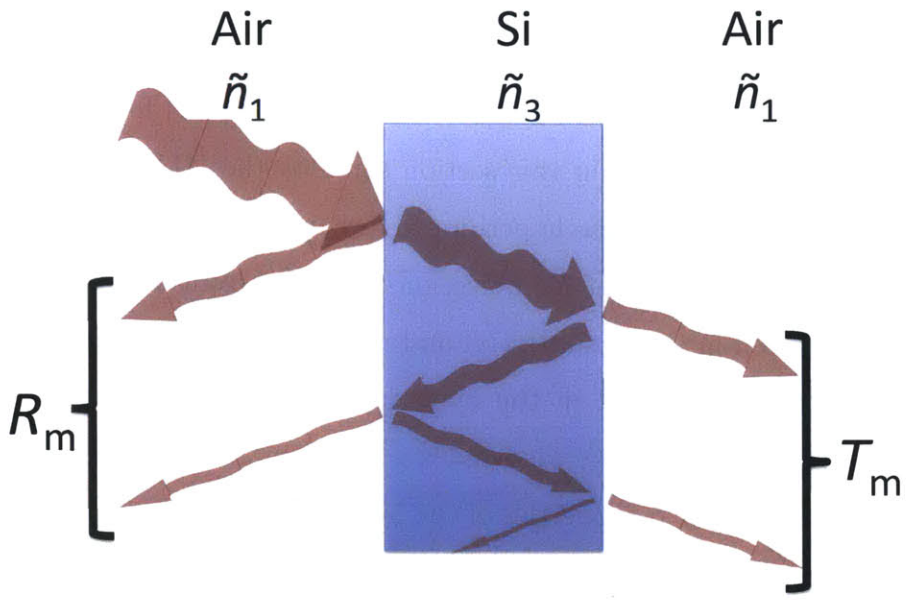

Figure 4-3: Ray-tracing of the many pathways incident light ends travel when an optically-thick slab is measured in FTIR. The summation of all the light rays leaving the sample to the left are accounted for in R_{m}; in turn the summation of all light rays exiting to the right are accounted for in T_{m}.

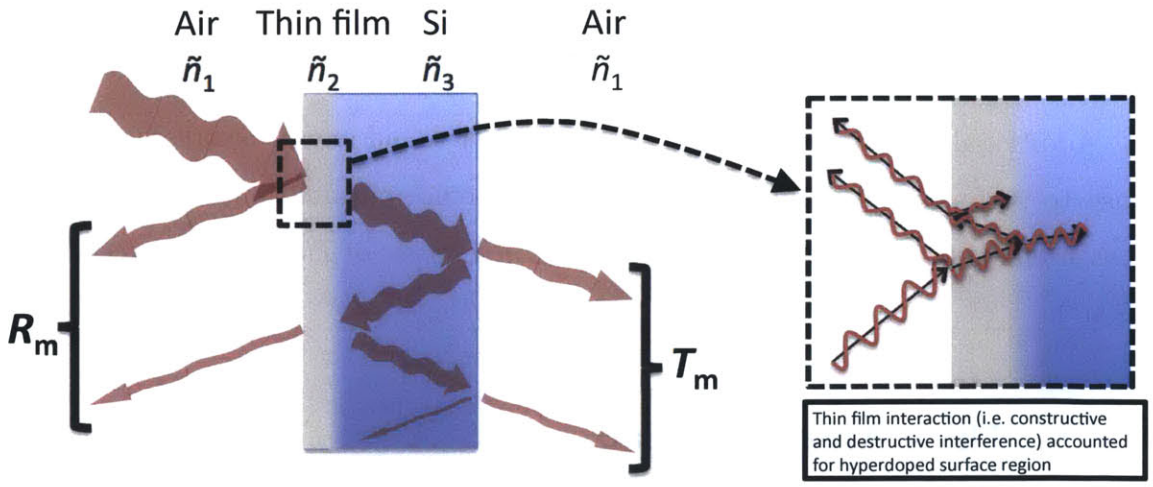

Figure 4-4: Schematic of optical interactions accounted for in measuring hyperdoped Si samples. The summation of all the light rays leaving the sample to the left are accounted for in R_{m}; in turn the summation of all light rays exiting to the right are accounted for in T_{m}.

the front and back surfaces. The term "thick" here means that the slab is thicker than the coherence length of the wavelengths of light used in these measurements and that the Fresnel equations are inappropriate to describe the propagation of light through the material.

To start our analysis, we'll look at an example of light moving from one absorbing medium, with complex index $\tilde{n}_i = n_i + ik_i$, into another absorbing medium, $\tilde{n}_j = n_j + ik_j$. We represent the magnitude of the intensity of the reflected wave at normal incidence in equation (4.1); this quantity is known as the *reflectivity*. Note that this is different from the measured value R_{m} which accounts for the total number of reflected rays and is referred to as the *reflectance*.

$$R_{ij} = \frac{(n_i - n_j)^2 + (k_j - k_i)^2}{(n_i + n_j)^2 + (k_i + k_j)^2} \tag{4.1}$$

Light also is absorbed and loses intensity as it travels though a medium. This is described by Beer-Lambert's law, which describes that the attenuation of the intensity, I, of light as a function of position, x.

$$I = I_0 e^{(-\alpha x)} \tag{4.2}$$

The absorption coefficient, α, is defined in Equation 4.3 using the complex component of $\tilde{n}$ (also known as the extinction coefficient, k) and the wavelength of light measured in vacuum, λ_{vacuum}.

$$\alpha = \frac{4\pi k}{\lambda_{vacuum}} \tag{4.3}$$

Now we have all the equations needed to describe optical measurements performed on thick slabs. Our example system is one that represents one of the most common form of optical measurement: a thick slab of material that is surrounded by the same medium on both sides, as shown in Fig. 4-3. Generally this would be a slab with smooth surfaces that is surrounded by air, but the derivation done here will be for a general case, where the media surrounding the sample is absorbing and has a complex index. The measured reflectance and transmittance (labeled as R_m and T_m

in Figure 4-3), will be a function of the reflection at each interface and the absorption coefficient of the material. Using equations (4.1), (4.2), and (4.3) we can calculate the intensity of each of the light rays shown in the diagram found in Figure 4-3; the measured reflectance and transmittance will be summation of the intensities of all the rays exiting to the left or right as shown in Figure 4-3, respectively. The intensity of all the reflected and transmitted rays are shown in the summations in equations (4.4) and (4.5), where the thickness of the sample is d.

$$\begin{aligned} R_{\mathrm{m}} &= R_{13} + (1 - R_{13})^2 R_{13}(e^{-\alpha_3 d})^2 + (1 - R_{13})^2 R^3 (e^{-\alpha_3 d})^4 + \ldots \\ &= R_{13} + (1 - R_{13})^2 \sum_{n=1}^{\infty} (R_{13})^{2n-1} (e^{-\alpha_3 d})^{2n} \end{aligned} \tag{4.4}$$

$$\begin{aligned} T_{\mathrm{m}} &= (1 - R_{13})^2 e^{-\alpha_3 d} + (1 - R_{13})^2 R_{13}^2 (e^{-\alpha_3 d})^3 + (1 - R_{13})^2 R_{13}^4 (e^{-\alpha_3 d})^5 + \ldots \\ &= \sum_{n=1}^{\infty} (1 - R_{13}) R_{13}^{2(n-1)} (e^{-\alpha_3 d})^{2n-1} \end{aligned} \tag{4.5}$$

Note that the reflectivity moving from medium 1 to 3 and moving from 3 to 1 are identical in this case, and are thus both labeled as R_{13}. The summations in equations (4.4) and (4.5) can be simplified further. Treating the summations as geometric series yields equations (4.6) and (4.7).

$$R_{\mathrm{m}} = \frac{R_{13}(1 - e^{-2\alpha_3 d}(2R_{13} - 1))}{1 - e^{-2\alpha_3 d} R_{13}^2} \tag{4.6}$$

$$T_{\mathrm{m}} = \frac{(1 - R_{13})^2 e^{-\alpha_3 d}}{1 - e^{-2\alpha_3 d} R_{13}^2} \tag{4.7}$$

Substituting equations (4.1) and (4.3) into equations (4.6) and (4.7) allows you to solve for both n and k. A MATLAB solver is used to fit values of n_3 and k_3 , and the example is shown in figure 4-5. The measured spectral reflectance and transmittance is shown in the left plot in Figure 4-5, and the resulting numerical solver's solution

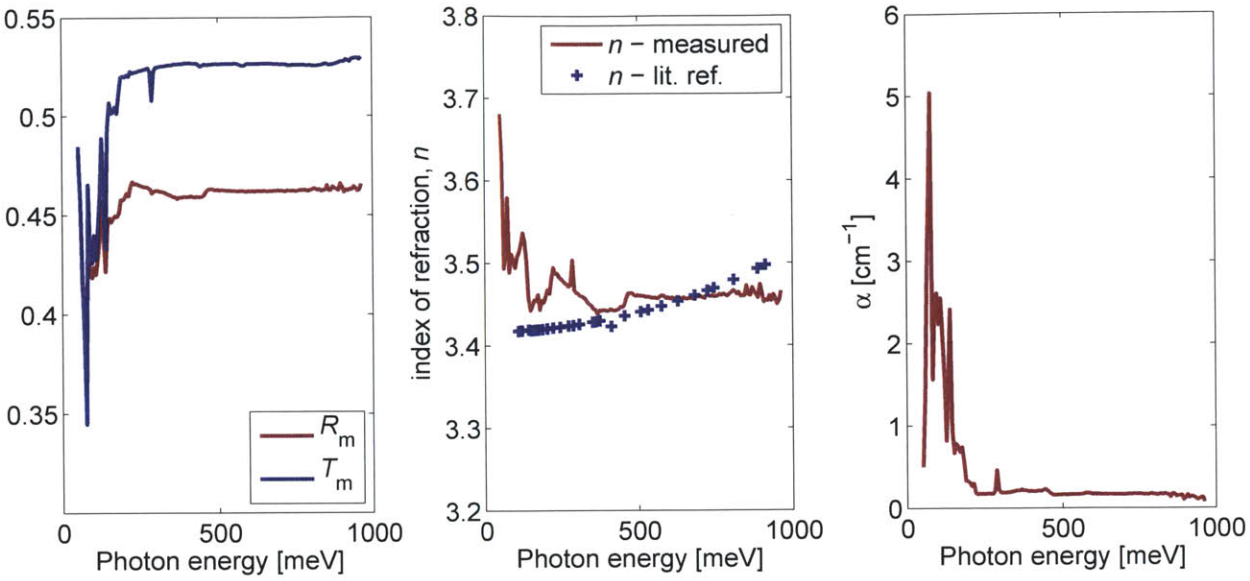

Figure 4-5: (left) The measured reflectance and transmittance of a thick silicon slab is used to calculate the (center) real part of the refractive index, and (right) the absorption coefficient of the substrate. Literature value for the real part of the refractive index for Si is from Reference [121].

for n and k are compared to literature values [121] in the center and right plots in Figure 4-5, respectively.

4.3.2 Thin Film Reflectivity and Transmittance

In this sub-section, we'll create the equations that determine the reflectivity of a thin film that is sandwiched between two different semi-infinite mediums. Constructive and destructive interference that occurs within a thin film and is related to the phase and amplitude of the electric field that accompanies propagating photons. We note that lower case letters, represent the reflectivity (r) or transmitivity (t) of the electric field at an interface, and not the intensity (R or T). The reflectivity and transmitivity of the electric field amplitude moving from medium i to j are given in equation 4.8) and (4.9), respectively. Note that equations (4.8) through (4.10) are for semi-infinite surface.

$$r_{ij} = \frac{\tilde{n}_i - \tilde{n}_j}{\tilde{n}_i + \tilde{n}_j} = \frac{(n_i - n_j) + i(k_i - k_j)}{(n_i + n_j) + i(k_i + k_j)} \tag{4.8}$$

$$t_{ij} = \frac{2\tilde{n}_i}{\tilde{n}_i + \tilde{n}_j} \tag{4.9}$$

The reflectivity of the electric field, r_{ij}, is related the reflected intensity or power, R_{ij}, we use the relation given in equation (4.10).

$$R_{ij} = |r_{ij}|^2 \tag{4.10}$$

Using a similar method to estimate the measured reflectivity and transmitivity of a thick slab (see derivation of equations (4.4) and (4.5),) we can estimate the thin film reflectivity and transmissivity of a thin film on a thick slab, given the material properties of each layer.

$$\begin{aligned} r_{123} &= r_{12} + t_{12}e^{i\delta}r_{23}e^{i\delta}t_{21} + t_{12}e^{i\delta}r_{23}e^{i\delta}r_{21}e^{i\delta}r_{23}e^{i\delta}t_{21} + ... \\ &= r_{12} + \frac{t_{12}r_{23}t_{21}e^{2i\delta}}{1 - r_{21}r_{23}e^{2i\delta}} \end{aligned} \tag{4.11}$$

$$\begin{aligned} t_{123} &= t_{12}e^{i\delta}t_{23}(1 + r_{21}r_{23}e^{2i\delta} + (r_{12}r_{23}e^{2i\delta})^2 + ...) \\ &= \frac{t_{12}t_{23}e^{i\delta}}{1 - r_{21}r_{23}e^{2i\delta}} \end{aligned} \tag{4.12}$$

In equations (4.11) and (4.12), we define δ as the complex phase, which helps describe the constructive and destructive interference in the film, as well as the attenuation that arises from absorption. The complex term δ is defined by equation (4.13).

$$\delta = \frac{2\pi\tilde{n}_2 d_2}{\lambda_{\text{vacuum}}} \tag{4.13}$$

Using equations (4.11) and (4.12), we can calculate the reflectance and transmit-

tance of the film between two semi-infinite media (i.e. the reflected and transmitted intensity or power.)

$$R_{123} = |r_{123}|^2 \tag{4.14}$$

$$T_{123} = \frac{Re(\tilde{n}_3)}{Re(\tilde{n}_1)}|t_{123}|^2 \tag{4.15}$$

Note that the operator $Re(\tilde{n})$ pulls out the real component of a complex number. R_{123} and T_{123} represent the reflectance and transmittance through a thin film of complex index, $\tilde{n}_2$ that is sandwiched between two semi-infinite layers of indices $\tilde{n}_1$ and $\tilde{n}_3$

4.3.3 Multi-layer Thin Films

The matrix method is a simple way to model multiple thin film stacks with ease. It yields the same information as found in equations (4.11) and (4.12), and the resultant field intensity reflectivity and transmitivity is representative of the entire stack. Here, we will go over the equations for the reflectivity and transmitivity for a thin film stack between two semi-infinite media.

A matrix for a single film is defined as:

$$M_j = \begin{bmatrix} cos(\frac{2\pi\tilde{n}_j d_j}{\lambda_{\text{vacuum}}}) & -\frac{i}{\tilde{n}_j} sin(\frac{2\pi\tilde{n}_j d_j}{\lambda_{\text{vacuum}}}) \\ -i\tilde{n}_j sin(\frac{2\pi\tilde{n}_i d_j}{\lambda_{\text{vacuum}}}) & cos(\frac{2\pi\tilde{n}_j d_j}{\lambda_{\text{vacuum}}}) \end{bmatrix} \tag{4.16}$$

For a stack of thin films, we simply multiply the matrices to yield the resultant matrix for the entire stack. Note that subscript 'j' denotes the index or position of the layer while the variable 'i' denotes square of root of negative one. For a stack of h films, where the h^{th} film is the on the bottom of the stack and the $j = 1$ film is

closest to the incident light, we use Equation (4.17). Note that the incident light can be entering from either the air or the substrate and $i = 1$ can either represent the surface layer or the deepest layer of the hyperdoped region, respectively.

$$M_f = \begin{bmatrix} m_{11} & m_{12} \\ m_{21} & m_{22} \end{bmatrix} = \prod_{j=1}^{h} M_j \tag{4.17}$$

We can then use M_f to evaluate the field reflectivity of this thin film stack that is sandwiched between media of indices $\tilde{n}_1$ and $\tilde{n}_3$. It is given below.

$$r_{1f3} = \frac{2\tilde{n}_1}{(m_{11} + m_{12}\tilde{n}_3)\tilde{n}_1 + m_{21} + m_{22}\tilde{n}_3} \tag{4.18}$$

$$t_{1f3} = \frac{(m_{11} + m_{12}\tilde{n}_3)\tilde{n}_1 - (m_{21} + m_{22}\tilde{n}_3)}{(m_{11} + m_{12}\tilde{n}_3)\tilde{n}_1 + m_{21} + m_{22}\tilde{n}_3} \tag{4.19}$$

To calculate the reflectivity and transmitivity of the intensity or power of a thin film stack, use equations (4.14) and (4.15) and replace r_{123} and t_{123} with r_{1f3} and t_{1f3}, respectively.

4.3.4 Extracting $n + ik$ for Hyperdoped-Si

When analyzing the measured reflectance and transmittance of a hyper-doped silicon sample, we treat the sample as a multi-layer thin film system sitting on a thick substrate. The analysis in this subsection combines the information from previous subsections to create a model for analyzing optical spectra of hyper-doped silicon samples.

The hyper-doped layer is modeled as a thin film stack with a graded index. To estimate the complex index for each layer, we use the mixed media approximation, which assumes that the complex dielectric of the mixed media is a weighted average of the respective densities of the components in the mixture.

$$\tilde{\epsilon}_{\text{eff}} = \sum_j \rho_j \tilde{\epsilon}_j \tag{4.20}$$

For a sulfur-doped sample, we use the mixed media approximation to estimate the change in $\tilde{n}$ for the regions of varying S concentration. The sulfur concentration as a function of depth is reproduced in figure 4-6b. For this analysis, we assume that complex dielectric scales with the sulfur concentration, as shown figure 4-6b, and the equation below:

$$\tilde{\epsilon}_i = (n_i + ik_i)^2 = \frac{[S]}{[S]_{\text{peak}}}\tilde{\epsilon}_2 + \left(1 - \frac{[S]}{[S]_{\text{peak}}}\right) \tag{4.21}$$

In the above equation, $\tilde{\epsilon}_i$ represents the complex dielectric of thin film layer i, and $\tilde{\epsilon}_2$ represents the complex dialectric for the peak S concentration (represented by $i = 1$ in our model.)

We can then use an analysis similar to that used to derive equations (4.6) and (4.7) to create a model where the front and back surface have different field reflectivities and transmitivities.

$$R_{\text{m}} = |r_{1\text{f}3}|^2 + \frac{|t_{1\text{f}3}|^2 |r_{31}|^2 |t_{3\text{f}1}|^2 e^{(-2\alpha_3 d_3)}}{1 - |r_{1\text{f}3}|^2 |r_{31}|^2 e^{(-2\alpha d_3)}} \tag{4.22}$$

$$T_{\text{m}} = \frac{|t_{1\text{f}3}|^2 |t_{31}|^2 e^{(-2\alpha_3 d_3)}}{1 - |r_{3\text{f}1}|^2 |r_{31}|^2 e^{(-2\alpha_3 d_3)}} \tag{4.23}$$

The sample system consists of a graded thin film of HD-Si (subscript f) on the surface of an optically thick substrate (subscript 1) that is surrounding by air on both sides (subscript 3). The thickness of the substrate is given by d_3, and the coefficients r_{ijk} and t_{ijk} are determined using the matrix method from Equations 4.18 and 4.19. Also note that r_{ij} and t_{ij} are given by equations (4.8) and (4.9), respectively. Also note that the substrate index, $\tilde{n}_3$, is determined by measuring the substrate alone and performing an analysis similar to figure 4-5 and described in Section 4.3.1.

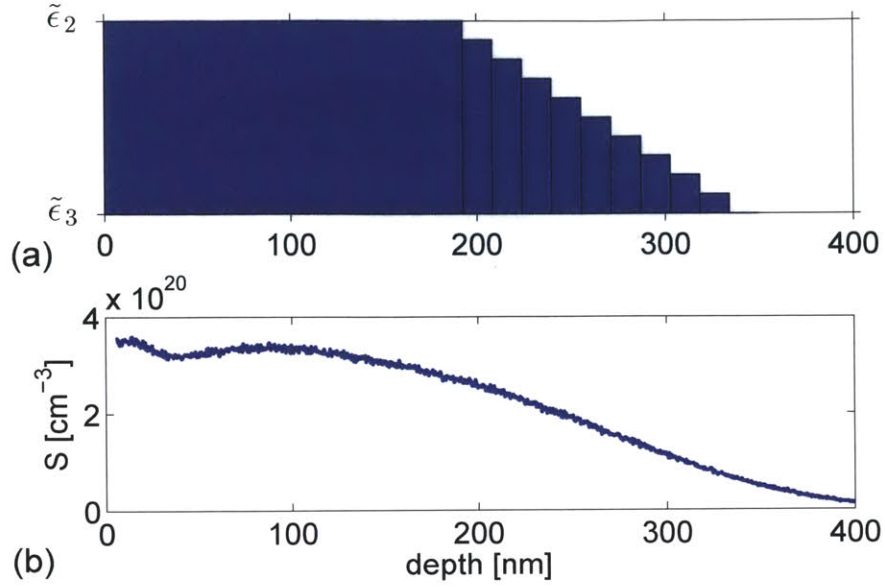

Figure 4-6: (a) The measured S concentration as a function of depth and (b) the scaling of the dielectric of each layer used in the model.

All the models and equations above assume normal incidence, but the actual reflectance measurement is performed at 12° off-normal incidence. This discrepancy between model and the actual measurement is assumed to be negligible because the incident beam is unpolarized. Unpolarized light consists of both TM and TE waves, and their effect on reflectance measurements is to either decrease or increase the measured reflectance, respectively. At this shallow angle, the angular dependence causes less than 0.5% change from the normal incidence for both TM and TE waves.

4.3.5 Vibrational Modes Present in Measured Spectra

The raw measured values of R_m and T_m for samples which have received different implantation doses of S are shown in Figure 4-7. At energies 200 meV and below, the measured spectra are dominated by absorption of various vibrational modes of non-S impurities in the samples. These peaks are seen in both the R_m and T_m spectra for both the Si substrate sample (i.e. sample without S hyperdoping) and samples with S hyperdoping. This indicates that there are no prominent vibrational modes that are introduced by S. This is also true for annealed samples, which exhibit the same

vibrational modes found in the substrate. A list of the observed vibrational modes in these samples and their presumed origins based on literature are enumerated in table 4.1.

FTIR Absorption Peaks in Samples		Literature FTIR Absorption Peaks		
Energy [meV]	Wavenumber [cm^{-1}]	Wavenumber [cm^{-1}]	Source	Reference
76	611	613	O_i symmetric stretch mode	[81]
92	739	735	SiC amorphous*	[11]
110	887	885	Longitudinal V-O	[81]
119	963	900-1000	VO_3 complexes	[81]
137	1107	1107	O_i antisymmetric stretch mode	[81]
162	1306	1304	B-H "D-mode"	[81]

Table 4.1: Enumeration of all vibrational modes seen in samples both T_m and R_m and likely sources of those modes from the literature. The mode marked with an * was seen in un-annealed Si samples that were ion-implanted with C.

Note that in the transmission spectra, there is some considerable noise in the spectra between 200 and 280 meV (1200-2200 cm^{-1}), and account for $\pm 3\%$ error, which is enough to create rather large changes in the extracted values of $n_2 + ik_2$ and makes repeatability difficult. Different strategies of binning data to effectively average adjacent data points were tried, but this unacceptably distorted the spectra. This error is most likely due to fluctuations in humidity because water vapor absorbs very strongly at these photon energies [55, 157].

Because of the strong absorption from different oxygen related vibrational modes in the substrate and water vapor in the air, extraction of the optical properties of the hyperdoped layer is error-prone at photon energies below 280 meV. For these reasons, only extracted values of 280 meV and above will be extracted and reported in this thesis. If future work requires getting optical information down below 280 meV using FTIR on hyperdoped silicon, samples made on float zone wafers[1] and implementing a system that can purge the FTIR chamber with dry nitrogen would enable consistent and accurate measurements down to 170 meV.

[1]Float zone wafers are oxygen free. Czochralski-grown wafers (which are use for substrates in this thesis) can have up to 10^{18} cm^{-3} oxygen atoms in them.

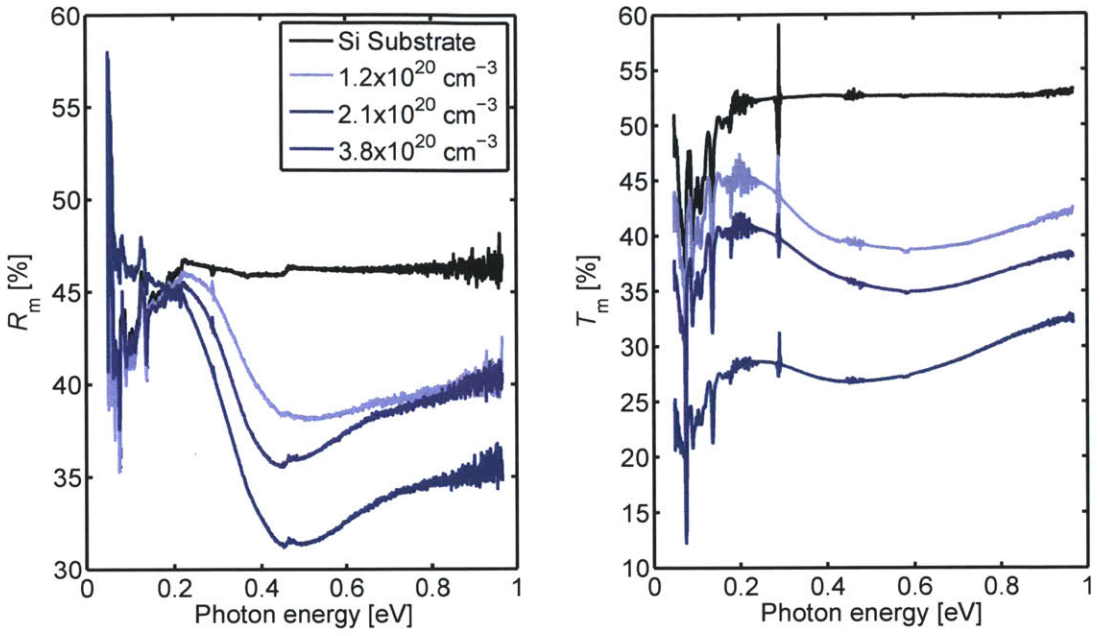

Figure 4-7: Measured reflectance, R_{m}, and transmittance, T_{m}, of samples of varying peak S concentrations.

4.3.6 Analysis of Measured Spectra and Comments on Error in $n + ik$ Extraction

Using equations 4.22 and 4.23, we can extract the absorption coefficient and the index of refraction of hyper-doped silicon layers from the measured spectra. An example of this for samples which received S doses of 3×10^{15} and 1×10^{16} cm^{-2} and have a peak concentration of 1.2×10^{20} and 3.8×10^{20} cm^{-3}, respectively, are shown in figure 4-8. These results are consistent with previous ellispometry results by Pan [101]. Pan's results were performed on silicon on insulator wafers which had a thin S hyperdoped top layer. Pan's results indicate that S-rich regions were index matched with the silicon beneath it for the photon energies measured (770 meV and above). The results presented here from FTIR show that for 770 meV and above, the index is matched very closely to the substrate underneath, with major variations occurring at energies below 770meV. Pan also extracted an absorption coefficient around 1×10^4 cm^{-1} for photons energies between 770 and 1100 meV for a sample with peak S concentration of 1.5×10^{20} cm^{-3}, which is very close to the absorption coefficient

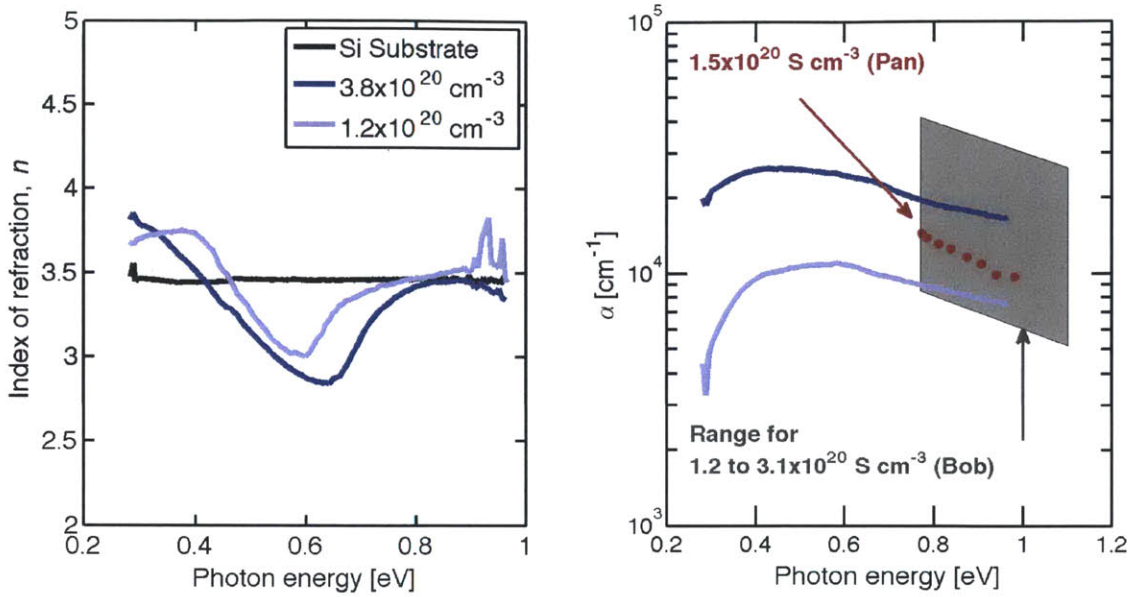

Figure 4-8: The real part of the index of refraction, n, which is computed from T_{m} and R_{m} is shown on the left for both the Si substrate sample and hyperdoped samples with a peak S concentrations reported in the legend. The absorption coefficient, α is shown on the right for the hyperdoped samples. References for Pan and Bob are found in References [101] and [10], respectively.

estimated in figure 4-8 for a sample with peak S concentration of 1.2×10^{20} cm^{-3}. Additionally, in figure 4-8, the absorption coefficient reported by Pan [101] and the range of values reported by Bob [10] for S concentrations between 1.2 to 3.1×10^{20}cm^{-3} are shown. Absorption coefficients reported by Bob are average values for the range of 600 to 1100 meV, and are not given spectrally. Good agreement between the FTIR results in this thesis and past measurements is demonstrated.

The use of the multi-layer graded index was necessary to match the previous estimate of Pan [101]. Initially a single-layer model was used, but this did not yield an n_2 that was indexed matched with silicon above 770 meV. While the switch to a multi-layer model from a single-layer model had a large effect on n_2, it had a very small effect on the spectral shape of α_2.

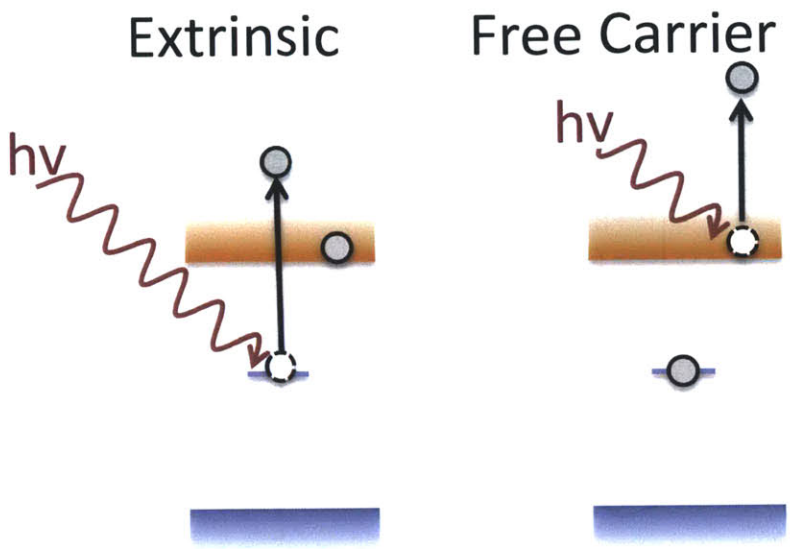

Figure 4-9: Possible absorption mechanisms in S-hyperdoped Si.

4.4 Removing Free Carrier Absorption

To understand the band structure and trap energies introduced by S, it is necessary to remove any absorption components that are not related to the promotion of S donor electrons from trap states. To do this, we assume that the absorption is made up of both extrinsic and free-carrier absorption. The two absorption events are described in Equation 4.24 and Figure 4-9.

$$\alpha = \alpha_{\text{extrinsic}} + \alpha_{\text{FCA}} \tag{4.24}$$

S Implant Dose $[\text{cm}^{-2}]$	S Peak Conc. $[\text{cm}^{-3}]$	Annealing Temp. K	μ_e $[\frac{\text{cm}^2}{\text{Vs}}]$	n_{sheet} $[\text{cm}^{-2}]$
3×10^{15}	1.2×10^{20}	N/A	162	7.54×10^{13}
6×10^{15}	2.1×10^{20}	N/A	103	1.41×10^{14}
1×10^{16}	3.8×10^{20}	N/A	36	7.52×10^{14}
1×10^{16}	3.8×10^{20}	500	45	8.54×10^{14}
1×10^{16}	3.8×10^{20}	600	42	1.25×10^{15}
1×10^{16}	3.8×10^{20}	700	61	7.42×10^{14}
1×10^{16}	3.8×10^{20}	800	107	2.87×10^{14}
1×10^{16}	3.8×10^{20}	900	200	8.30×10^{13}

Table 4.2: List of mobilities and sheet carrier concentration for samples studied in this chapter.

The majority carriers in S-doped samples are electrons. Free carrier absorption in these samples is determined by the refractive index (n), the CB effective mass for electrons (m^*), the density of free carriers in the conduction band (denoted n_e to avoid confusion), the conduction band mobility (μ_e), and other physical constants (ϵ_0, c, and e). Table 4.2 lists values measured by Hall effect for both mobility and sheet carrier concentration, that are used to calculate α_{FCA} in equation 4.25.

$$\alpha_{\text{FCA}} = \frac{e\lambda^2 n_e}{4\pi\epsilon_0 c^3 n m^{*2} \mu} \tag{4.25}$$

Then for silicon, the free carrier absorption [125] is given by Equation 4.26.

$$\alpha_{\text{FCA}} = \frac{n_e \lambda^2}{\mu_e} 10^{-16} \tag{4.26}$$

Where λ is in μm, μ_e is in $\frac{\text{cm}^2}{\text{Vs}}$, n_e is in cm^{-3}, and α_{FCA} is in cm^{-1}. The value of n_e is estimated by $n_e = n_{\text{sheet}}/d_{\text{eff}}$, where effective layer thickness, d_{eff} is set to 270 nm, which is the distance from the surface to the middle of the tail region region defined in Figure 4-6. Free carrier absorption makes up a very small portion of the overall absorption. A comparison of α_2 for all measured samples with and without free carrier absorption removed can be found in Figures 4-10. At a photon energy of 280 meV, samples that received a dose of 1×10^{16} S cm^{-2}, free carrier absorption was accounted for up to nearly 10% of absorption, while samples below this concentration had a maximum of 1.5% contribution from free carrier absorption at $280meV$.

4.5 Spectral Fits for Samples of Varying S Concentration

In this section, results from optical measurements outlined in the previous section are used to extract α as a function of photon energy for different S concentrations. Fits to the absorption spectra yield insight into how the band structure changes as a function of sulfur concentration; this will be used to determine what S concentrations maintain a separation between the IB and the conduction band. Additionally, the

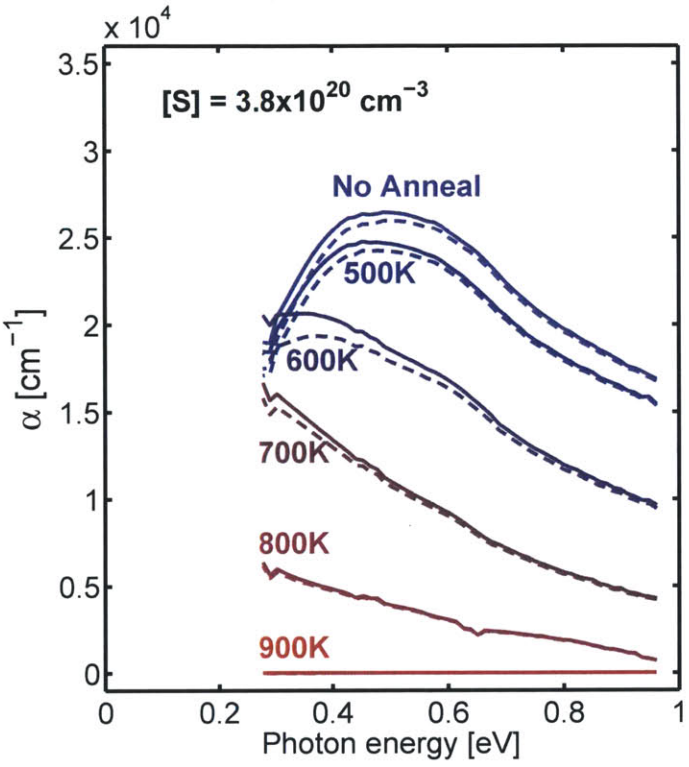

Figure 4-10: Comparison of absorption coefficient spectra with and without free carrier absorption (α_{FCA}) subtracted for samples which received a S dose of 1×10^{16} cm^{-2} and annealed at different temperatures for 100 seconds in an Argon atmosphere. Solid lines are unaltered, while dotted lines have α_{FCA} subtracted.

results outlined below yield α, which is used to calculate ν.

The sub-gap absorption is modeled as the excitation of an electron from a trap state to the conduction band (which is assumed to be a parabolic band). The extrinsic absorption coefficient for sub-gap light is assumed to be a product of the number of traps, N_T, and their optical cross-section, σ_{O_e}. If each S atom introduces g deep levels, then N_T/g would be equal to the S concentration.

$$\alpha_e = N_T \sigma_{O_e}(\hbar\omega) \tag{4.27}$$

In the above equation, σ_{O_e} is the optical cross section and is a function of the photon energy, $\hbar\omega$. The spectral dependence of the σ_{O_e} depends on the nature of the trap state, the matrix elements describing the transition, and the band to which excitation occurs. An excellent review of the different forms σ_{O_e} can take and their derivations are outlined in Reference [51]. Absorption coefficient of S in silicon is best fit by a "forbidden vertical transition", and the functional form is often referred to as the Lucovsky formula [72, 42]. The Lucovsky formula is reproduced below:

$$\sigma_{O_e} \propto \frac{(\hbar\omega - E_T)^{3/2}}{(\hbar\omega)^3} \tag{4.28}$$

The above equation describes the excitation from a single discrete trap level to a parabolic band (see figure 4-1b), and has been used to fit optical cross-sections for deep levels in Si in the past [94, 50], including S [116]. The peak value of the optical cross-section reported in References [30, 116, 43] matches very well to the values measured here (within a factor of 2). More recent data of Te donors shows a very similar spectral dependence of the optical cross-section [39]. To account for broadening of the trap levels with increased S concentration (see Figure 4-1a), the equation 4.28 is convoluted with a Gaussian distribution of trap energies, which have a mean trap energy of E_T and standard deviation of E_σ, as shown in equation 4.29. A Gaussian distribution estimates the trap state distribution because it resembles the shape of Se-induced DOS at high concentration, as calculated in previous DFT studies [31].

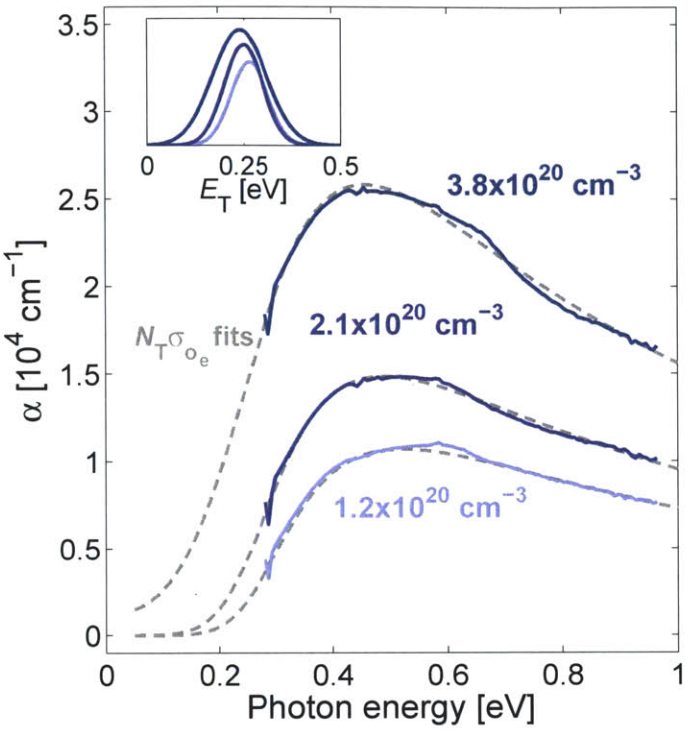

Figure 4-11: Spectral fits using the Gaussian-convoluted Lucovsky formula to the absorption coefficient for Si doped with different concentrations of S. Free carrier absorption is subtracted using equation 4.26.

$$\sigma_{O_e} \propto \frac{1}{E_\sigma \sqrt{2\pi}} \int_0^\infty \frac{(\hbar\omega - E)^{3/2}}{(\hbar\omega)^3} exp\left(-\frac{(E - E_T)^2}{2E_\sigma^2}\right) dE \tag{4.29}$$

The graphical results of the spectral fits to α, as well as the fit parameters are shown in figure 4-11 and table 4.3, respectively. Error bars show range of fitting parameters that yield a coefficient determination, R^2 above 0.98.

S Implant Dose $[cm^{-2}]$	S Peak Conc. $[cm^{-3}]$	Trap Energy, E_T $[meV]$	Trap Std. Dev. E_σ $[meV]$
3×10^{15}	1.2×10^{20}	265 ± 5	47.5 ± 10
6×10^{15}	2.1×10^{20}	250 ± 5	50 ± 10
1×10^{16}	3.8×10^{20}	240 ± 10	70 ± 10

Table 4.3: Numerical values from spectral fits using the Gaussian-broadened Lucovsky formula (Equation 4.29) to Si doped with S at various concentrations.

A normalized trap distribution for each S concentration is plotted in the inset of

Figure 4-11 to yield a visualization of the modeled trap distribution from the spectral fits. The highest S concentration sample exhibits a very small optical gap, which is consistent with broadening leading to trap states that are degenerate or near-degenerate with the conduction band. This concentration is consistent with IMT seen in this material system [147] and the change in electronic structure observed in x-ray emission spectroscopy [135]. Because an IBPV absorber layer requires that the IB maintains a separation in energy from either band edge, the highest concentration sample is deemed to have an unsuitable band structure for IBPV. This indicates that the IMT in S-doped Si is not useful for making IBPV device. A similar gradual broadening is seen in the Si:Se system around the concentrations of the IMT [31].

It is important to note that the trap-state energy broadening described in Equation 4.29 can also be modeled by an increase in electron-phonon coupling, and is mathematically described by replacing E_σ^2 with $2kTd_{\mathrm{FC}}$, where d_{FC} is the Franck-Condon parameter.[54, 21] However, it seems unlikely that electron-phonon interactions are the major driving force behind the broadening. Previous spectrally-resolved temperature-dependent photoconductivity measurements performed under bias (where S atoms were ionized with $E_{\mathrm{T}} \approx 0.6\mathrm{eV}$) and in short-circuit mode (S atoms were neutral $E_{\mathrm{T}} \approx 0.3\mathrm{eV}$) indicated that spectral broadening due electron-phonon coupling was strong in ionized S impurities,[43, 107] but negligible in neutral S impurities.[43] Because optical measurements reported here are not performed under bias, S atoms are presumed to be neutral and the effect of optical broadening due phonon-electron coupling is deemed negligible. Despite this, even if the broadening seen in Figure 4-11 is due to an increase in the electron- phonon coupling, it would signify that thermal capture and emission cross-sections are enhanced for this shallow S level at higher S concentrations; this would also be detrimental to the performance for an IBPV material due to enhanced defect-related recombination.

4.6 Optical Properties of Annealed Si:S and Relationship to Chemical State Change of Dopants

The absorption spectra of annealed samples presented in this thesis fits within a broader context of the work done previously on similar S-doped Si materials that have studied sub-band gap optical absorption deactivation with annealing. In the next sub-section, we'll discuss annealing work done on both S-hyperdoped samples prepared using both fs-lasers and PLM, respectively to provide context, and then expand on this understanding using the FTIR work presented here.

4.6.1 Previous Work on Understanding Optical Deactivation of Si:S upon Annealing

The deactivation of the sub-band gap absorption has been observed in and documented in both Si hyperdoped with S by PLM [60] and by fs-laser irradiation [148, 25, 24, 128]. The mechanisms for the optical deactivation has been studied more extensively in the fs-laser doped materials. In a study by Tull [142], the change in sub-band gap absorption for fs-laser S-doped Si was measured for samples annealed for both different times and temperatures. Tull reported that both increasing time and annealing temperature lead to a decrease in absorption. Tull estimated the S diffusion length for each of these time temperature profiles and found that sub-band gap absorption was deactivated when the estimated diffusion length was around 10 nm. Tull hypothesized that small optically inactive precipitates were forming. This short length scale ($10nm$) of diffusion and precipitation may be why SIMS profiles of annealed samples up to 823K show no noticeable change in S concentration [110].[2]

Further evidence of precipitation has been reported by Newman [91] using x-ray absorption fine structure (EXAFS) on Si:Se fabricated using fs-lasers. Newman's analysis of EXAFS spectra of samples annealed at different temperatures indicated that the local chemical environment of the Se dopants was changing with increased

[2]See figure 3.3 in referenced document.

annealing temperature and a strong correlation between the pre-annealed chemical state and the optical absorption was established. Further EXAFS work by Newman [90] indicates that the majority of Se atoms were likely in a precipitate $SiSe_2$ state when fully annealed.

4.6.2 Optical Analysis of Annealed Si:S Samples: Modeling of Optical Data using a 3 State System

In section 4.5, defect levels at ca. 250 meV were identified in Si:S samples at various dopant concentrations that had not undergone any annealing. However, as annealing progresses, the shape of the absorption spectra changes, with the most notable change being that the peak in the absorption spectra shifts to lower energy, as seen in figure 4-10. This may be indicative of optically active defects forming that have a binding energy that is lower than ca. 250 meV. To investigate this, the absorption coefficients (with free carrier absorption subtracted) of the annealed samples were assumed to be the superposition of electrons being promoted to the CB from trap states at two different energies. The first trap state, we'll call state A and will be described as having an average trap energy $E_{\mathrm{T_A}}$ and distribution with standard deviation E_{σ_A}. Both values for $E_{\mathrm{T_A}}$ and E_{σ_A} will be set to values found in table 4.3 for the sample with 3.8×10^{20} S cm^{-3} and be described by equation 4.29. The second trap state, for simplicity, was assumed to be a discrete level with a shallower binding energy of $E_{\mathrm{T_B}}$, and is described by equation 4.28. We'll call this trap level state B. This model is summarized by the equation below:

$$\begin{aligned}
\alpha_{\mathrm{e_A}} &= I_\mathrm{A} \frac{1}{E_{\sigma_\mathrm{A}}\sqrt{2\pi}} \int_0^\infty \frac{(\hbar\omega - E)^{3/2}}{(\hbar\omega)^3} exp\left(-\frac{(E - E_{\mathrm{T_A}})^2}{2E_{\sigma_\mathrm{A}}^2}\right) dE \\
\alpha_{\mathrm{e_B}} &= I_\mathrm{B} \frac{(\hbar\omega - E_{\mathrm{T_B}})^{3/2}}{(\hbar\omega)^3} \\
\alpha_\mathrm{e} - \alpha_\mathrm{FCA} &= \alpha_{\mathrm{e_A}} + \alpha_{\mathrm{e_B}}
\end{aligned} \tag{4.30}$$

The constants I_A and I_B are scaling factors that represent a convolution of the

optical cross-section strength of a single trap state and the number trap states; they have units of $(\text{eV})^{3/2}$ cm^{-1}. A value of 100 meV was used for E_{T_B} because that was the value that yielded the lowest cumulative R^2 value for all fits.[3] The results of fits are shown in figure 4-12, which demonstrate good agreement between the theory presented in equations 4.30 and the measured optical properties. All fits had an R^2 value of 0.98 or higher (with the exception of 800K annealed sample, which had a value of 0.95).[4]

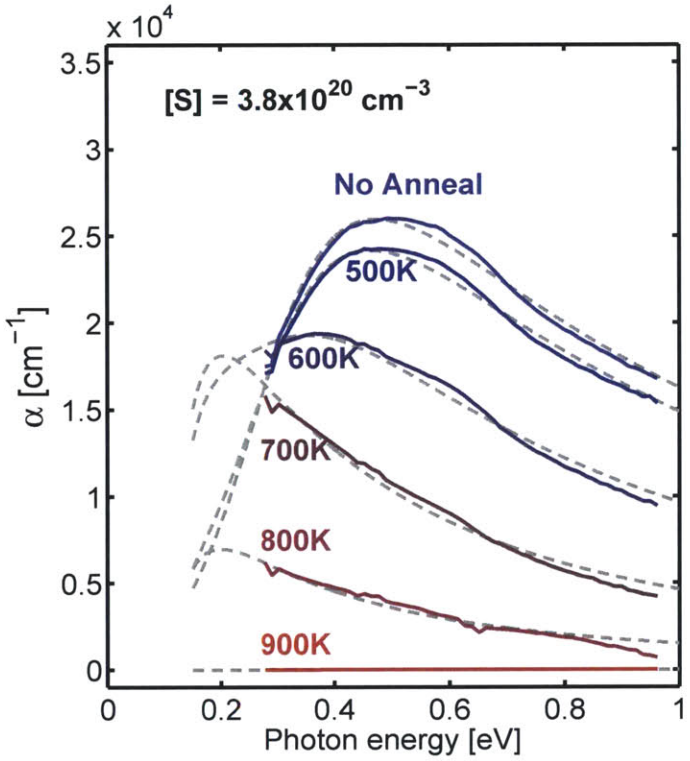

Figure 4-12: Samples which received a S dose of 1×10^{16} cm^{-2} were annealed at different temperatures for 100 seconds in an Argon atmosphere. Fits are made using equation 4.30 and are shown as dotted gray lines. Free carrier absorption has been removed from measured spectra and represent the quantity $(\alpha_\text{e} - \alpha_\text{FCA})$ from Equation 4.30.

[3]Values of E_{T_B} between 70-130 meV yielded R^2 values of > 0.98 for all samples except the 800 K anneal, which only had R^2 value of > 0.95 for the energy ranges 70-110 meV.

[4]It is important to note that replacing α_{2_A} with a discrete trap state does not improve the fits made in the previous section (maximum R^2 value of 0.94 was attained on the non-annealed sample). In other words, the broadening of the ca. 250 meV trap state is necessary to model the optical absorption spectra observed in the non-annealed sample, and the same spectral shape cannot be made to using two discrete energies.

The relative contributions from both α_{e_A} and α_{e_B} to the measured quantity $(\alpha_e - \alpha_{FCA})$ are given in Figure 4-13 where I_A and I_B are plotted a function of annealing temperature. As the annealing temperature is increased to 700 K, the contribution of the absorption that is attributed to state A decreases, and the contribution from state B increases. At higher annealing temperatures, sub-band gap absorption vanishes altogether and the contribution from state B vanishes as well.

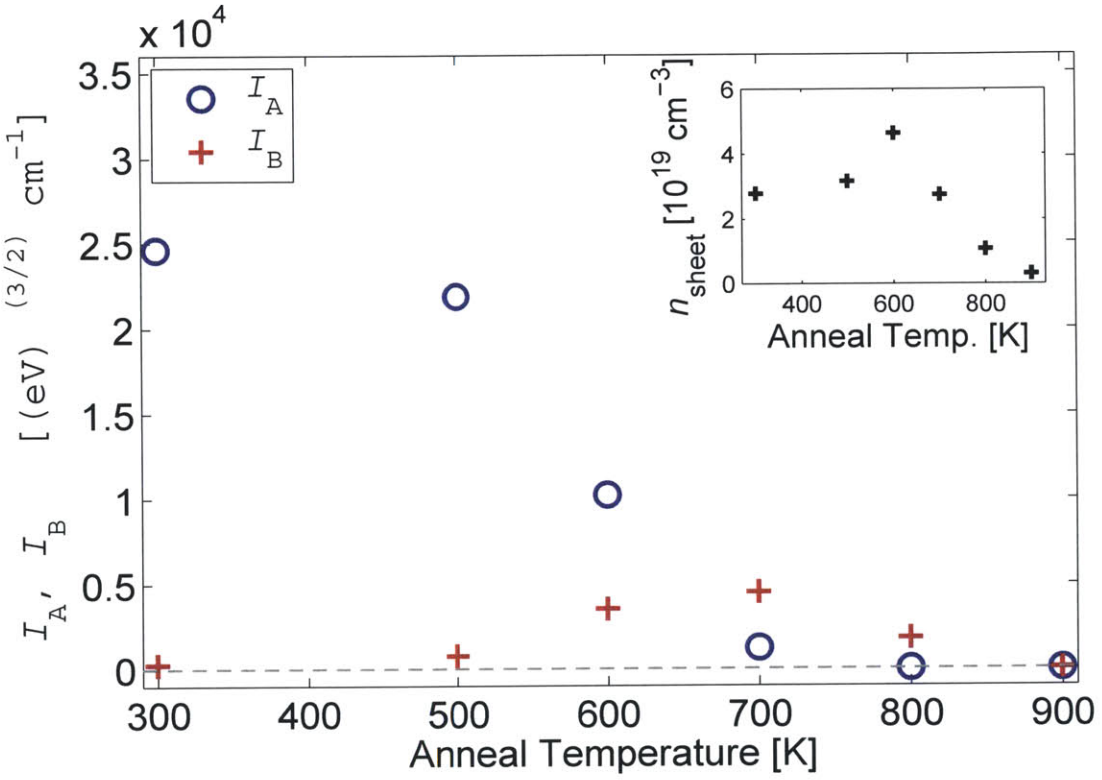

Figure 4-13: Resultant fit parameters I_A and I_B (see Equation set 4.30) from spectral fits shown in Figure 4-12. Inset shows carrier concentration, n_{sheet}, which is estimated by dividing sheet carrier concentration, n_{sheet} from table 4.2, by an effective layer thickness of 270 nm.

The transition from state A to B seen from 300 to 700 K can is not inconsistent with the theory of clustering and precipitation. Previous work done by Grimmeiss and Janzén [41, 40, 53] (see overview in section 2.1) demonstrated that the electron binding energy of S donor sites decreases as the number of S atoms at a donor site increases. For example, moving from single-substitutional site (S^0), to a dimer (S_2^0), to a larger cluster $S_C^0(X_n)$, the binding energy of the S donor site decreases. A similar

trend is also seen in O thermal donors, which show decreasing donor binding energy with increasing cluster size [66, 67]. Thus, state B could represent a larger cluster of S atoms than state A.

Annealing at temperatures above 700 K, both state B and the overall sub-band gap absorption go to zero. One possible explanation is that as larger clusters form, there are fewer clusters altogether, thus reducing overall sub-band gap absorption coefficient to negligibly small values.

To further develop this model, further structural work would need to be performed to determine the chemical state of the S dopants and identify any precipitates, as well as identify and quantify any compensating defects. The electrical behavior (i.e. sheet carrier concentration) is not well correlated with optical data; sheet carriers may be influenced by compensating S defects that are optically inactive but also metastable. While past TEM work of annealed samples did not reveal the presence of any precipitates or S clusters that were visible [137], this is not too surprising as small precipitates may not provide enough contrast in TEM if the strain they induce is small. For example, microscopists studying O-related precipitates in Si had a hard time imaging these defects; successful identification of O-precipitates in Si required 8+ hours of annealing at very high temperatures to grow large enough precipitates that were visible in TEM [134, 33, 150].

4.7 Conclusion

The optical data presented in this chapter tells us how the band structure of this material system changes for different S concentration and annealing conditions. First, for samples that have a S concentration beyond the critical concentration to drive an IMT (ca. $3 \pm 1.2 \times 10^{20}$ cm^{-3}) [147], have an IB that is either degenerate or near-degenerate with the conduction band. Because a large optical and electronic gap is needed between the IB and the closest band edge for an IB absorber layer, Si doped with S to concentrations above 2.1×10^{20} S cm^{-3} are deemed unsuitable for IB PV applications. This demonstrates that the IMT is not desirable in the Si:S system for

developing an IBPV absorber layer.

Additionally, we see that for samples with S concentration below the critical IMT concentration, there is still significant broadening of the IB. This is certainly not surprising as transport at low temperature at these S concentrations occurs through a hopping mechanism [147], which indicates that there is already some interaction between S donor electron wave functions.

Finally, changes seen in the optical spectra of samples annealed at different temperatures are consistent with a diffusion/precipitation model. As samples are annealed, the optical spectra can be modeled as the photoionization of defect levels with a lower binding energy, which is consistent with the fact that S donor binding energies decrease as the number of S atoms in the cluster increases [41, 40, 53].

4.8 Acknowledgements

I would like to thank Gang Chen for the use of his group's reflectivity stage used for FTIR measurements, and I would specifically like to thank Wei-Chun Hsu for instruction on using the stage.

Chapter 5

Low-temperature Photoconductivity

5.1 Motivation and Introduction

In the previous chapter, we measured the absorption coefficient of Si:S, and determined that only S concentrations at or below 2.1×10^{20} S cm^{-3} yield an IB that is not degenerate or near-degenerate with the conduction band. For this reason, a sample with 1.2×10^{20} S cm^{-3} will be investigated to measure it's ability to generate free carriers using sub-band gap light.

During a photoconductivity measurement, light is used to induce a change in resistance of the sample. Usually the drop in resistance results from the creation of excess mobile charge carriers by direct optical excitation from an immobile or trapped state into a mobile or conductive state. This change in sample resistance, ΔR, can be converted into a change in conductivity of material, $\Delta\sigma$, based on the sample geometry. If the number of absorbed photons in the region of interest is known, it can be treated as a generation rate, G. Then, the mobility-lifetime product, $\mu\tau$, can be calculated from $\Delta\sigma = G\tau\mu e$.

A lot of work has been published on spectral photo-response of either photodiodes or planar photoconductive devices using S hyperdoped Si using PLM [105, 111, 120, 106], but no work has been able to achieve photoresponse from sub-band gap light.

Only in work by Persans [106] was any quantitative value placed on the mobility-lifetime product for electrons in the CB, $\mu_e\tau_e$, for S hyperdoped Si. Based on the noise floor of the measurement, Persans placed an upper bound of $2 \times 10^{-}7\frac{cm^2}{V}$ on $\mu_e\tau_e$. Using this upper bound and the absorption coefficient of Si with a S concentration that maintains a band structure suitable IB PV, we can estimate an upper limit of the figure of merit, ν_e. At a S concentration of $1.2 \times 10^{20}cm^{-3}$, we find $\nu < 5$.[1] Because this upper limit is still in the acceptable range for an IB PV material, no definitive statement can be said about this material's viability to make an efficient IBPV devices. For this reason, increasing the sensitivity of this measurement by an order of magnitude will help determine if $\mu_e\tau_e$ is high enough to yield $\nu > 1$. The next section will describe the process of designing a photoconductivity experiment with increased sensitivity.

5.2 Design of a Photoconductivity Experiment

Creating an experiment that can accurately measure $\mu_e\tau_e$ requires both maximizing the response of the measured value (i.e. a voltage or current) while reducing the influence of false positives. In a photoconductivity experiment where the majority carriers are electrons, the signal response scales as the ratio of the number of photo-excited excess carriers, Δn, to the number of dark carriers, n. There are also many non-photoconductive effects that can create spurious signals that also need to be avoided to get an accurate measurement. The ways to maximize Δn, minimize n, and curtail the effects of any false positives will be outlined in the following sub-sections. An excellent resource that dives into the details of different photoconductivity experiments is N.V. Joshi's book [57]. Another excellent resource that gives a brief overview of the different experimental techniques is found in Reference [14].

[1] A value of V_{bi} is assumed to be that of the band gap of silicon when estimating the upper limit, and $c = 2$.

5.2.1 Maximizing Δn

The number of light-generated carriers, Δn, is proportional to the generation rate, G, by $\Delta n = G\tau_e$. Therefore, one obvious way to increase Δn is to simply increase G by increasing the intensity of the light source. To achieve a high photon flux, we'll use a laser source for these measurements. A continuous wave (CW) laser is used because of the problems accompanied by a pulsed laser. A pulsed laser often has a much higher instantaneous power (a single mJ pulse that lasts a ns can have a MW peak power!) but when a short pulse ($< 10ns$) is used to generate carriers in a material with very short carrier lifetimes (such as S hyperdoped Si with $\tau_e < 1ns$) then the electrical signal is effectively a 100MHz-1GHz AC signal. At this high frequency range, the inductance and capacitance inherent in a metal wire used to measure the signal can be quite high and actually greatly attenuate the AC electrical signal.

5.2.2 Minimizing n_e

Another strategy for maximizing signal is to freeze out carriers by cooling the sample. For Si:S doped at 1.2×10^{20} S cm^{-3}, the dark carrier concentration decreases by a factor of 300 when cooled from room temperature to 35K (see Figure 2-7).

Despite this advantage, low-temperature measurements pose several problems. First, doing any electrical measurements in a cryostat requires running wires down to the sample. To avoid heat conduction through the wires that may heat the sample, the wires are wrapped several times around the sheaths of the first and second stage regenerators so that they are cold-sinked to cryostat. This means that the cables can be quite long, which makes doing high frequency measurements difficult. For example, the 3m of silver-plated copper wires used in the cryostat in these experiments attenuate a 10 MHz sine wave by 50%. Indeed, as mentioned in the previous subsection, this was the motivation for using a CW laser.

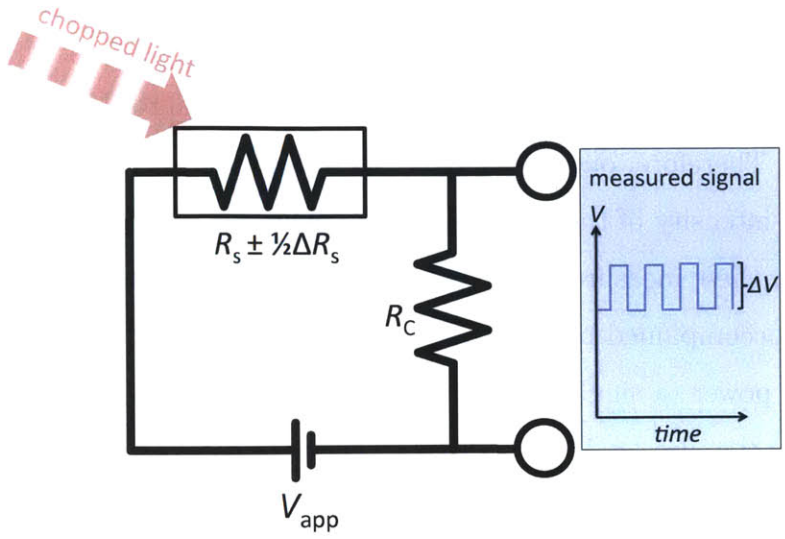

Figure 5-1: Equivalent circuit of the standard setup for a photoconductivity experiment.

5.2.3 Maximizing Measured Signal

To aid in optimizing the measured voltage signal in a photoconductivity experiment, a simple equivalent circuit diagram, shown in figure 5-1, will be used to analyze the system. The sample resistance will either be $(R_s + \frac{1}{2}\Delta R_s)$ or $(R_s - \frac{1}{2}\Delta R_s)$ if the sample is in the dark or under illumination, respectively. Note that ΔR_s is the difference between the illuminated and dark resistance, and R_s represents the average sample resistance. The resistor R_C is a comparative resistor, and is often represents the internal impedance of the voltage measurement instrument (such as an oscilloscope, which often has a 50Ω impedance, and is used in transient photoconductivity measurement). In the steady state experiments performed here, a lock-in amplifier was used, and R_C represents the resistance a standard axial-lead resistor, which was chosen to have a resistance near that of the sample. The actual measured AC voltage will be voltage across the resistor R_C, and the peak to peak change in measured voltage, we'll label ΔV, as shown in Figure 5-1.

$$\frac{\Delta V}{V_{\text{app}}} = R_{\text{C}} \left(\frac{1}{R_{\text{C}} + (R_{\text{s}} - \frac{1}{2}\Delta R_{\text{s}})} - \frac{1}{R_{\text{C}} + (R_{\text{s}} + \frac{1}{2}\Delta R_{\text{s}})} \right) \tag{5.1}$$

The value V_{app} represents an applied voltage that is kept constant. In order to maximize ΔV for a given R_C, we make the substitution $\delta = \frac{1}{2}\Delta R_{\text{s}}/R_{\text{s}}$ into equation 5.1, differentiate with respect to R_{s}, and then set the derivative to zero to find the local maximum for equation 5.1. The following is the result of that process:

$$\frac{R_{\text{s}}}{R_{\text{C}}} = \frac{(1-\delta)^{-1/2} - (1+\delta)^{-1/2}}{(1+\delta)^{1/2} - (1-\delta)^{1/2}} \tag{5.2}$$

For small signal ($\delta \to 0$), we take the limit which yields:

$$R_{\text{s}} = R_{\text{C}} \text{ for maximum signal} \tag{5.3}$$

This result, while trivial, should help dictate the sample geometry design. For example, if a transient measurement is going to be performed using an oscilloscope with a 50 Ω internal impedance then the contact geometry on the sample should be designed to yield a sample resistance of 50 Ω. However, optimizing the sample resistance is not the only consideration when designing a contact geometry, and often a more pressing issue is the one of inhomogeneous illumination, as discussed in the next sub-section. In these set of experiments, we'll be using a lock-in amplifier to make the majority of the measurements, which has a very high (> 10 MΩ) internal impedance, and we'll be using a resistor in parallel with the the lock-in terminals to help optimize the signal.

5.2.4 Proper Sample Metallization Geometry

A well designed photoconductivity experiment should be able to extract $\mu\tau$ from the measured values, and poor design of the contact geometry can prevent accurate measurement of these properties. Inhomogeneities in the illumination intensity can prevent any meaningful extraction of $\mu\tau$. We'll define two types of illumination inhomogeneity, *series* and *parallel*. To describe this effect, let's look at a sample

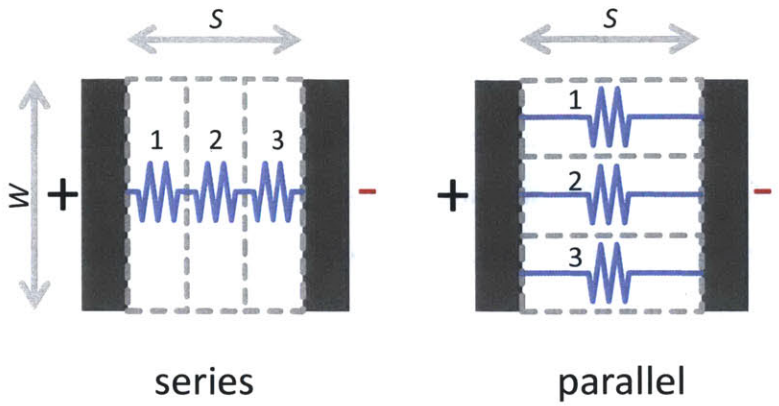

Figure 5-2: Model circuits for both series and parallel illumination inhomogeneity between two rectangular contact pads that are of length W and spacing separation S.

with two separated rectangular contact pads. The spaces in between the contact pads is split into 3 different sub-sections, one with a parallel configuration and one with a series configuration, as shown in figure 5-2. In this simple example, we'll assume that each sub-section has the same area and dark sheet resistance, $\rho_{\text{sheet}} = 1/(n_{\text{sheet}}\mu e)$. We'll also assume that illumination over a given sub-section is constant throughout and it's illuminated resistance can be calculated by assuming a uniform excess sheet carrier concentration Δn_{sheet} across the sub-section. We'll also assume that the illumination intensity is confined to within the three sub-section, and that the summation of all excess carriers for each subsection is the same for both examples (i.e. $\Delta n_{1_{\text{sheet}}} + \Delta n_{2_{\text{sheet}}} + \Delta n_{3_{\text{sheet}}} = \text{constant}$). Solving the very simple resistor network described in Figure 5-2 results in the following:

$$R_{\text{parallel}} = \frac{3S}{W\mu e}\left(3n_{\text{sheet}} + \Delta n_{1_{\text{sheet}}} + \Delta n_{2_{\text{sheet}}} + \Delta n_{3_{\text{sheet}}}\right)^{-1} \tag{5.4}$$

$$R_{\text{series}} = \frac{S}{3W\mu e}\left(\frac{1}{n_{\text{sheet}} + \Delta n_{1_{\text{sheet}}}} + \frac{1}{n_{\text{sheet}} + \Delta n_{2_{\text{sheet}}}} + \frac{1}{n_{\text{sheet}} + \Delta n_{3_{\text{sheet}}}}\right) \tag{5.5}$$

From the equations 5.4 and 5.5, we can see only R_{parallel} is immune to any inhomogeneity in illumination intensity. This shows that only if the illumination inhomogene-

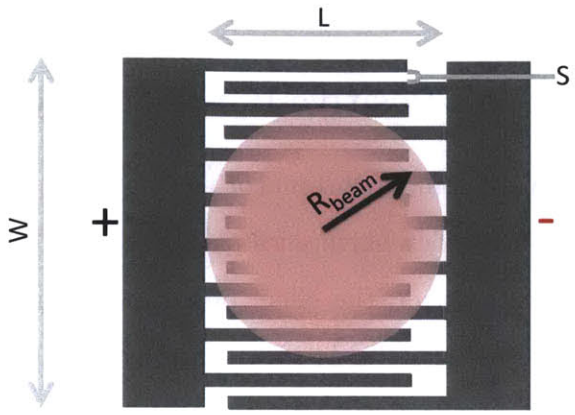

Figure 5-3: Interdigitated contact pattern with circular illumination beam. This contact geometry minimizes any effects of beam inhomogeneity and allows accurate extraction of $\mu\tau$.

ity occurs in a direction perpendicular to the contact geometry will inhomogeneity effects be negligible. Thus, to prevent this, it is best to keep S small in comparison to the length scales associated with inhomogeneities. For a circular illumination beam with a Guassian profile, this can be the full-width at half-maximum beam radius, R_{beam}. Thus a good rule of thumb is to keep the contact spacing between negative and positive terminals smaller than R_{beam}.

$$R_{\text{beam}} >> S \tag{5.6}$$

This is a major motivation for using an interdigitated contact pattern with narrow finger spacing (see Figure 5-3). For such a contact pattern, if the beam size is kept smaller than the area enclosed by all the fingers, but much larger than S, then an average photon flux ([photons per sec absorbed in sample]/[area enclosed by contacts]) can be used to estimate a generation rate. In figure 5-3, the total area enclosed by the contacts refers to $L \times W$. As long as the measured lifetime is assumed to be independent of the excess carrier density, this methodology can be used to calculate $\mu\tau$ using $\mu\tau = \frac{\Delta\sigma}{Ge}$ (where $\Delta\sigma$ is calculated assuming the overall change in conductance

represents a uniform change in conductivity).

5.2.5 Eliminating False Positive I: Non-monochromatic Light

Using a white light source with a monochromator to create monochromatic light can be problematic because higher order harmonics can pass through. This is especially noticeable when trying to understand the effect of sub-band gap photons, and some above-band gap light is present that leads to a spurious signals. Even with proper filtering, any small amount of unwanted wavelengths that get through can ruin a measurement, especially for highly sensitive measurements on materials with short lifetimes (such as PLM Si:S). This is one of the major driving forces for using a laser light source, which does not suffer from this problem.

5.2.6 Eliminating False Positive II: Internal Photoemission

At a metal semiconductor junction, the Fermi energy of the metal often sits somewhere near the middle of the gap of the semiconductor. If this is the case, then sub-band gap photons can photo-excite electrons from the metal into the CB of the semiconductor [26]. This is more prevalent in a lightly-doped semiconductors because an electric field can exist at the interface that can help move hot electrons from the metal into the semiconductor; this type of metal-semiconductor contact is often referred to as a Schottky contact or a Schottky diode. A schematic of this process is shown in Figure 5-4, which shows a Schottky diode under illumination. In fact, this effect has been used to make IR photodetectors on silicon that have response to photons with energy less than band gap [104, 154, 114]. Additionally measuring the photocurrent response of a Schottky contact as a function of photon energy is a technique called internal photoemission spectroscopy (IPES) that is used to estimate the band offset between both metal-semiconductors and semiconductor-insulator interfaces [1, 2, 93].

Because the main driving force behind internal photoemission is the creation of a field at the metal-semiconductor interface, one of the best ways to eliminate this is effect is to heavily dope the semiconductor under the metal contact. This removes

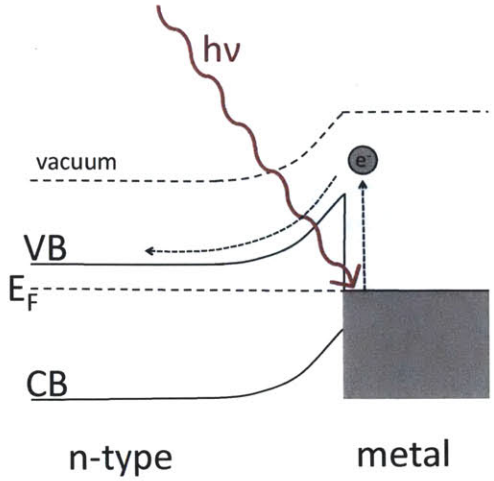

Figure 5-4: A Schottky contact with a strong built-in field under illumination. Sub-band gap light can excite charges from the metal that can be subsequently separated by the electric field, a process called internal photoemission. This charge excitation and separation process is a false positive in a photoconductivity experiment.

the Schottky junction and creates a tunnel junction. One way to test for internal photoemission is to see if a current can be measured when no bias is applied (i.e. a short-circuit current is seen). In these experiments we will use heavy doping under the contacts to reduce the effects of internal photoemission.

5.2.7 Eliminating False Positive III: Sample Heating

One of the most misleading false positives in a photoconductivity experiment is sample heating. Theoretically a sample that has an *infinitely short* lifetime can still yield a large measured $\Delta\sigma$ if the sample has a strong conductivity dependence on temperature. A carrier that is promoted and immediately thermalizes gives up its energy to the lattice and releases phonons. These phonons can them promote carriers out of trap states as the sample heats up. This false positive is certainly present for experiments done at low temperature where carrier freeze-out occurs, and is a false positive that plagues Si:S samples measured here. The model developed below is meant to be illustrative of heating effects in these types of measurements, but many of the

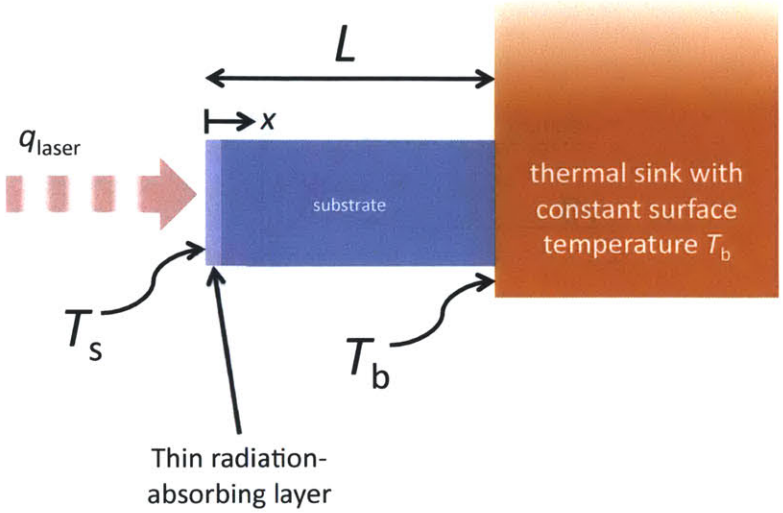

Figure 5-5: Schematic of the heat transfer model used to evaluate the effects of sample heating, which is a false positive in photoconductivity experiments.

assumptions are specific to the measurements performed on the Si:S samples in this thesis.

The best way to differentiate between both thermal and photoconductive effects is by studying the temporal response of the sample conductivity. Photoconductive effects[2] happen very quickly, and reach steady state in a timescale that is equal to the lifetime of the material. In contrast, the characteristic time to reach thermal steady state for an object being radiatively heated on it's surface is described by the Fourier number, Fo.

$$Fo = \frac{tk}{\rho c L^2} \tag{5.7}$$

Fo is a function of the thermal conductivity (k), thermal capacitance (c), cross-sectional length (L), and time (t). Even for a thin silicon wafer, the time to reach a $Fo = 1$ is longer than a ms. Because thermal effects can be much slower, we can exploit this fact by using a light source that is chopped (or pulsed) at a frequency that

[2]Photoconductive in this context refers to the promotion of trapped or immobile charge carriers into a conductive band using a photon.

is much faster than the inverse of this characteristic thermal time (*i.e.* $f >> \frac{k}{\rho c L^2}$). In this frequency regime, the peak to peak change in temperature between periods of illumination and darkness will be greatly reduced.

To understand this effect, a 1-D heat transfer model (which is detailed in Appendix A) was created to model temperature transient on the surface. A schematic of the model system is given in Figure 5-5. In the model, the sample has a thin film surface (to represent the Si:S layer on the surface) that absorbs the incident radiation. The model assumes that none of the laser radiation is absorbed in the substrate. The incident flux of radiation is given by q_{laser}, and the back surface is held at a fixed temperature (T_{b}) by a thermal sink. The sample surface is represented by temperature T_{s}. For the measurements performed for this thesis, a large block of copper is used to mount the sample, and is represented by the thermal sink shown in Figure 5-5. The laser intensity is assumed to be sinusoidally varying in time.

The model was used to study how the peak to peak change in surface temperature varies as a function of laser chopping frequency, f. The results, which show the peak to peak change in $\Delta T_{\text{S}}/\Delta T_{\text{S}_{SS}}$ (dimensionless temperature, where $T_{\text{S}_{SS}}$ is the steady state change in surface temperature) as as function of non-dimensional frequency ($f\rho cL^2/k$) are in Figure 5-6, and shows that the peak to peak change in temperature decreases only above a certain critical value of dimensionless frequency.

Because the electrical conductivity of Si:S samples used for this experiment is so temperature dependent, sample heating is the largest false positive present in these measurements. The frequency dependence will be employed to differentiate a heating and a photoconductive (or non-thermal) response in the following measurements.

5.3 Sample Fabrication

Photoconductivity samples received an S ion implantation dose of 3×10^{15} S cm^{-2} and have a peak S concentration of 1.2×10^{20} S cm^{-3} after PLM. Because measurements are performed at a temperature of 36 K, freeze-out of the S-donor electrons means additional doping is required to create contacts with low contact resistance at

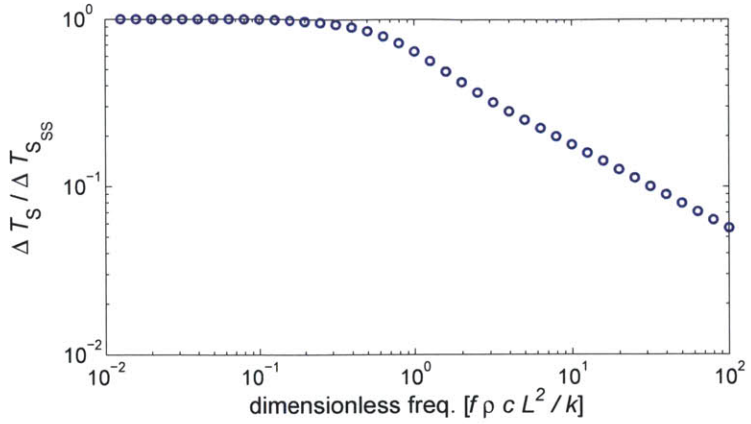

Figure 5-6: Thermal modeling results indicate high chopping frequencies reduce peak to peak temperature changes of sample surface. ΔT_{SS} represents the steady-state temperature change.

low temperature. Heavy doping of P locally underneath the metal contacts is used to achieve this. Creating excellent metal-semiconductor contact is vital to the experiment in two ways. First, by reducing contact resistance, the major resistor in the sample becomes the S-doped region, which makes estimates of the sheet conductivity of that region accurate (which will be described in section 5.4.2). Second, heavily doping reduces false positives, such as internal photoemission, which is described in Section 5.2.6.

To achieve the heavy P doping under the contacts, a new modified sample preparation was performed, as shown in Figure 5-7. Photoconductivity samples received a blanket $^{32}S^+$ ion implantation dose of 3×10^{15} atoms cm^{-2} and a second, local $^{31}P^+$ ion implantation at 10 keV to a dose of 1×10^{15} atoms cm^{-2}. The sample area that received the P implant was defined by photolithography. An additional control sample received a blanket implant of both the $^{32}S^+$ and the $^{31}P^+$. After implantation, the PLM process was performed as described in Section 2.3. SIMS measured a surface concentration of P at 2×10^{19} atoms cm^{-3}, which is well above the insulator-to-metal transition for Si:P [115, 3], ensuring that no carrier freeze-out would occur under the contacts. Contacts consisting of a stack of Ti/Pd/Ag (20/20/200 nm) were defined by photolithography aligned to an area with the P implanted regions and deposited by e-beam evaporation. A schematic of the sample geometry is shown Fig. 5-8. The

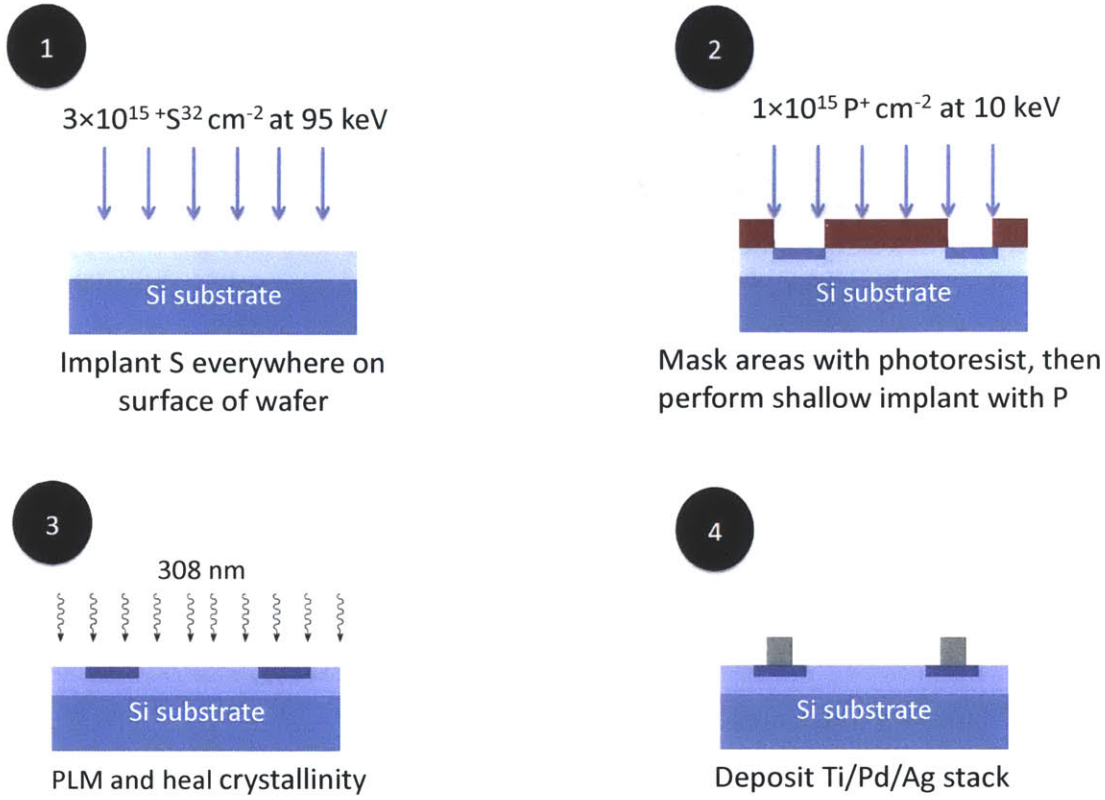

Figure 5-7: Overview of process of making photoconductivity sample with local P doping under contacts.

control sample with P implanted everywhere had identical metal contacts and will be referred to as the "contact control sample."

The samples are mounted using silver paint onto a piece of FZ silicon which had 100nm of silicon nitride deposited on it's surface, and Ti/Au rectangular pads e-beam deposited on it's edges. The silicon nitride acts as a dielectric to electrically insulate the sample from the copper block to which it is mounted, but is kept thin enough to maintain good thermal contact. Al wire bonds connect the bus bar of the sample to the Ti/Au pads. Thermal grease (Apezion N) is used to create good thermal contact to the copper block in the cryostat and the FZ Si sample mount. Electrical contact is made using copper-berylium tabs that make mechanical contact with the Ti/Au

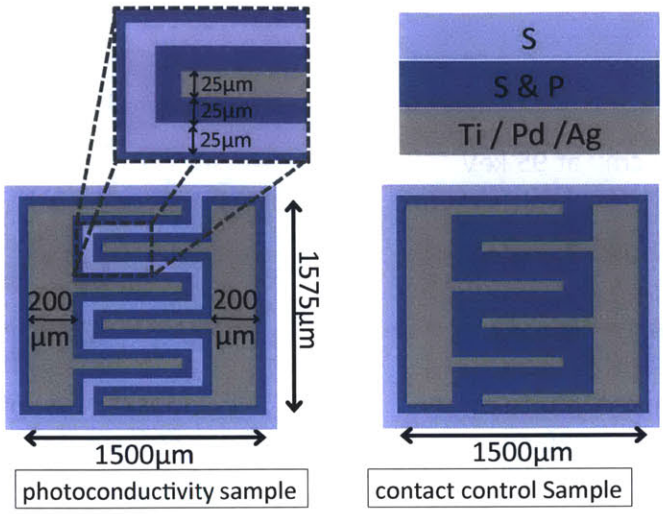

Figure 5-8: A schematic of the photoconductivity sample and contact control sample from a top-down view. Not drawn to scale. Actual samples have 8 fingers from each busbar.

pads. Figure 5-9 illustrates the sample and it's mount.

5.4 Experimental Methods and Results

5.4.1 Temeperature Calibration and Cryostat Description

Low-temperature measurements were performed in a closed-cycle He cryostat at 36 K. A quartz window allowed optical access through the vacuum shroud to perform photoconductivity measurements. During 4-point resistance measurements, the quartz window was replaced with a steel disc. Temperatures reported in this paper are based on a calibration where the temperatures measured by a permanent sensor in the cryostat was correlated to a temperature measured using a cryogenic temperature sensor (Lakeshore DT-670B-SD) mounted in an identical fashion as the actual samples. Temperature calibration measurements were fairly repeatable; the lowest reached temperature was within ± 1 K between three separate calibration runs, indicating that the thermal grease and mechanical pressure applied to attach the sample to the copper block in the cryostat provided a repeatable thermal resistance.

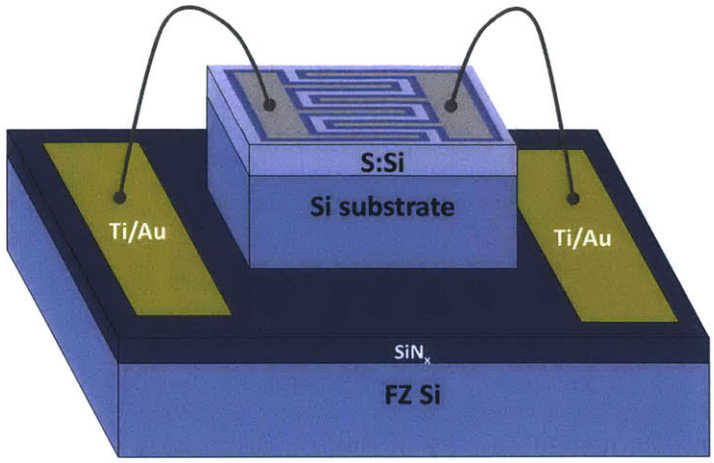

Figure 5-9: Photoconductivity samples are mounted on on a a float zone (FZ) silicon wafer coated with silicon nitride (SiN_x) to electrically isolate the sample from the rest of the system. Ti/Au contact pads were connected to sample's busbars via Al wire bonds.

5.4.2 Electrical Characterization

Four-point current-voltage measurements determined the sample resistance as a function of temperature and confirmed that carrier freeze-out occurs in the S-doped region of the photoconductivity sample. Similar measurements were performed on the contact control sample to estimate contact resistance and ensure that the P implanted regions were metallic and did not experience carrier freeze-out. The results of these measurements are shown in Figure 5-10, which demonstrates two important characteristics of the samples: first, that the S-doped region is the largest resistor in the photoconductivity sample, and second, that both the resistances of the S&P-doped regions and the metal contacts are negligibly small at low temperature.

In the inset in Figure 5-10, the estimated sheet resistance, ρ_{sheet}, of the S-only doped region in the photoconductivity sample is plotted and compared to four-point resistivity measurements performed by Winkler [147] on a sample which received the same S implantation but was prepared for Hall effect measurements. The value of

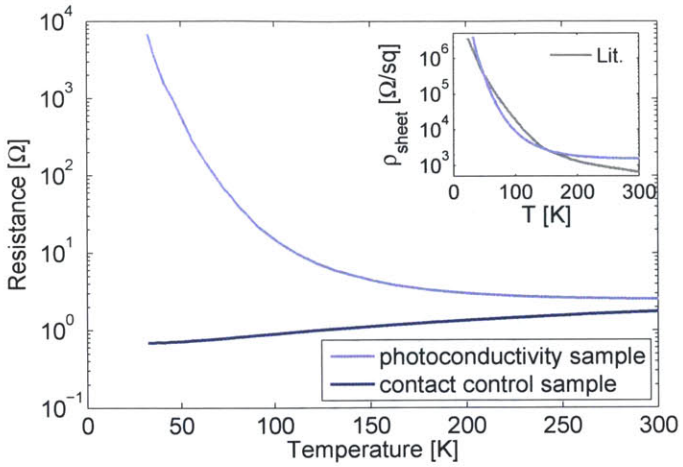

Figure 5-10: Resistance measurements of photoconductivity sample and contact control sample. Inset shows estimated ρ_{sheet} of photoconductivity sample compared to literature values of a similarly prepared sample [147].

ρ_{sheet} for the photoconductivity sample was estimated using the known geometry of the sample and assumed that only the entire measured resistance was dropped across the S-only region. The measured sheet resistivity data on the photoconductivity sample and the measurements by Winkler are within a factor of two of each other for temperatures below 250 K and are plotted in the inset of Figure 5-10; this indicates that at low temperature, the summation of the resistances from the contacts, wirebonds, and the S & P regions have a negligible contribution to the overall resistance.

5.4.3 Photoconductivity

Two different light sources were used to illuminate the sample with monochromatic light. 1550 nm and 405 nm laser diodes, which were cooled using a thermoelectric stage mount, provided 60 mW and 0.4 mW of incident radiation to the sample, respectively. Apertures of varying sizes were used to estimate the beam spot size and determined in both cases it was between 500 and 700 μm, which is smaller than the area enclosed by the busbars and the metal fingers on the sample, and larger than the spacing between metal fingers, which eliminates any issues with inhomogeneities (see Subsection 5.2.4). The light was mechanically chopped using an optical chopper wheel for frequencies ranging from 0.01-1000 Hz.

In this set of experiments, a large portion of the photo-response seen from sub-band gap light is attributed to the laser heating the sample; the Si:S sample's resistance, and thus its conductivity, is very temperature dependent, so any heating can give a false photo-response. To separate the thermal portion of the response from the photoconductive portion, the response was measured at different chopping frequencies, and the theoretical motivation for doing so was discussed in section 5.2.7.

To measure the change in resistance of the samples, two different, but complementary, methods were used, measuring photoconductivity at high and low frequencies, respectively. At low chopping frequencies (< 9 Hz), the sample resistance was measured as a function of time using a Keithley 2400 digital sourcemeter, which had a temporal resolution of 40 ms. At high frequencies, a Signal Recovery 7265 lock-in amplifier was used to measure the light-induced change in sample resistance. The digital sourcemeter was used to provide a DC voltage, V_{app}, across the sample and a comparative resistor, R_{C}, which were in series. The change in sample resistance was measured via the lock-in amplifier which monitored the AC voltage signal, with a peak-to-peak amplitude of ΔV, across R_{C}, as shown in figure 5-1. To ensure that the measurement system was behaving predictably (i.e. fits equation 5.1), different resistors were used for R_{C} and a sweep of V_{app} was performed at every chopper frequency.

For measurements taken using the lock-in amplifier, the average sample resistance, R_{s}, was determined by measuring the average current, I, provided by the sourcemeter. Thus we can estimate $R_{\text{s}} = V_{\text{app}}/I - R_{\text{C}}$. ΔV is measured at different values of V_a, and the slope of this curve is used to estimate the right-hand side of equation 5.1 and then solve for ΔR_{s}. In figure 5-11, ΔV is plotted against V_{app} for the both the highest and lowest chopped frequencies where the lock-in was used to measure photo-response of 1550nm light, and a linear trend is observed, as is expected from equation 5.1. While the trend is linear, there is a small offset at both the x and y intercepts that is just above the noise floor of the measurements, which means that internal photoemission cannot be eliminated from the signal (see discussion in Section 5.2.6). Additionally, from equation 5.1 and 5.3, $\Delta V/V_{\text{app}}$ should peak when R_{C} is equal to

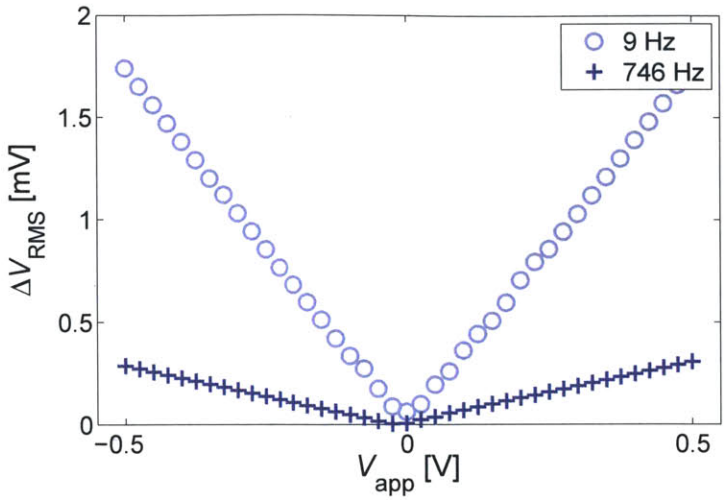

Figure 5-11: Measured ΔV for different V_{app} at highest and lowest frequencies measured using the lock-in amplifier illuminated under 1550 nm laser light.

R_{s}. A plot of $\Delta V/V_{\text{app}}$ for different values of R_{C} is given in figure 5-12 and equation 5.1 is used to fit the data; the excellent fit suggests that no capacitive or inductive effects in the system affected the measurements and that the system is well described by the circuit shown in figure 5-1.

Sheet conductivity of the S-doped region at 36 K, illuminated by chopped 1550 nm laser light, is plotted as a function of time in the left of Figure 5-13. For the lowest chopping frequency, 0.01 Hz, a rise time of around 10 seconds is needed for the conductivity to reach steady-state. This slow response time is attributed to heating of the sample surface by the laser. While a purely photoconductive response would reach steady state much faster than the time scales investigated here, a thermal response time can be much slower and is determined by the thermal mass and thermal diffusivity of both the substrate and the sample mount, as discussed in Subsection 5.2.7.

The fact that the thermally-induced response occurs over time scales that are many orders of magnitudes slower than a photoconductive response means that the two competing effects can be separated and individually quantified simply by changing the light-chopping frequency. Chopping at frequencies that are faster than the thermal transient response time will reduce the overall portion of the AC signal that is derived

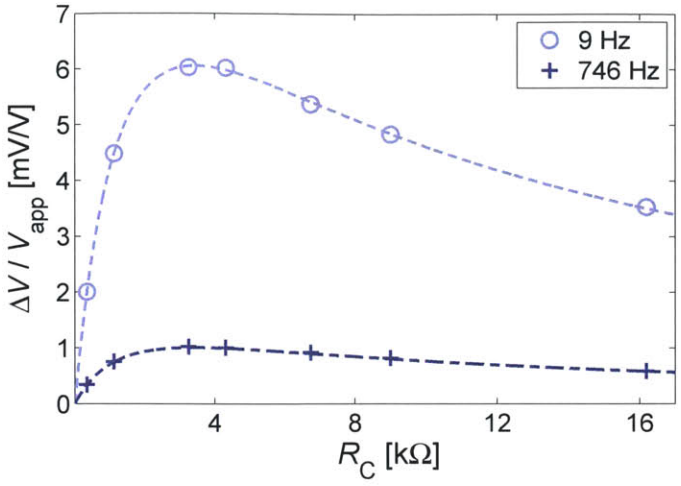

Figure 5-12: Measured $\Delta V/V_{\text{app}}$ for different values of R_{C} under 1550 nm laser illumination for highest and lowest frequencies measured using the lock-in amplifier. Dashed lines represent fits to measured data using Equation 5.1.

from sample heating. This effect is seen in left of Figure 5-13, where the peak-to-peak change in sheet conductivity, σ_{sheet}, is reduced as the chopping frequency is increased. This trend is extended to higher frequencies, where σ_{sheet} is divided by the flux of absorbed photons, G_{sheet}, and the charge of an electron, is plotted as a function of chopper frequency in the right of Figure 5-13. At high enough chopping frequencies, the thermal transient response is reduced to below that of the presumed photoconductive response.

G_{sheet}, the sheet carrier generation rate, is determined by $G_{\text{sheet}} = N_{\text{ph}}(1 - R_{\text{m}} - T_{\text{m}})/A$. N_{ph} is the measured rate at which photons hit the sample in photons per second and is measured using a National Institute of Standard (NIST) calibrated photodiode with known quantum efficiency. R_{m} and T_{m} are the measured transmittance and reflectance, respectively, of the optical sample described in the previous chapter with the same S concentration and measured in the previous chapter. A is the active area of the device ($1.1 \times 1.575 mm^2$.) The value of G_{sheet} is measured to be 5.4×10^{18} carriers $\text{cm}^{-2}\text{s}^{-1}$.

The photo-response at high frequency is used to determine an upper limit of the $\mu_e \tau_e$ product for mobile electrons freed from trap states by 1550nm light.

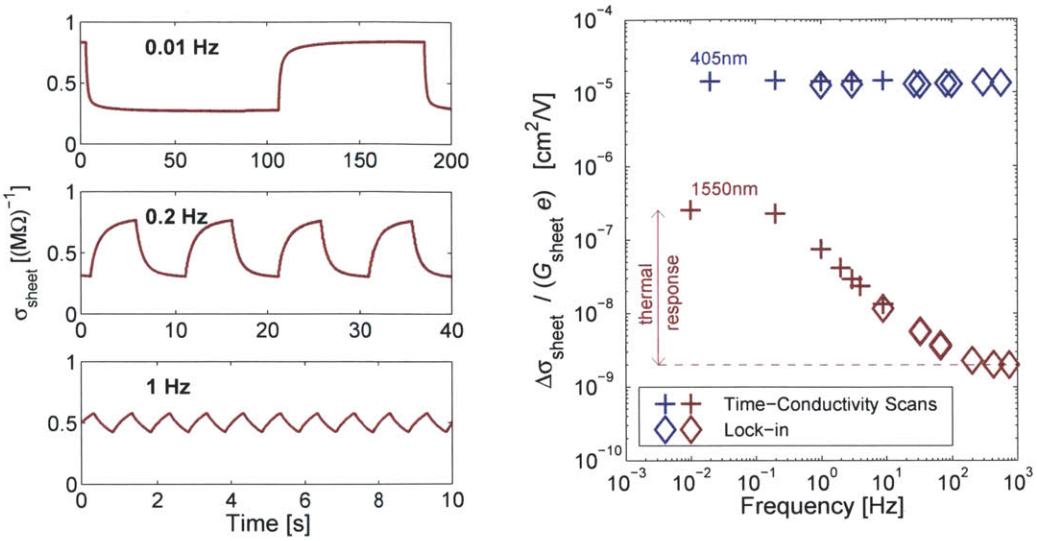

Figure 5-13: On the left, the time-conductivity scans of the photoconductivity sample are shown under 1550 nm illuminated light. On the right, the results on the left are combined with measurements taken using a lock-in amplifier, where the peak-to-peak change in sheet conductivity is divided by the product of sheet generation rate and the elementary charge, $G_{\text{sheet}}e$.

$$\mu_e\tau_e \leq \left.\frac{\Delta\sigma_{\text{sheet}}}{G_{\text{sheet}}e}\right|_{\text{high freq.}} = (2.5 \pm 1.5) \times 10^{-9}\frac{\text{cm}^2}{\text{V}} \tag{5.8}$$

The value of $(2.5 \pm 1.5) \times 10^{-9} cm^2/V$ in equation 5.8 acts as an upper limit on the $\mu_e\tau_e$ product because false positives, such as internal photoemission from the contacts, cannot be ruled out as a possible contributor to this response. This low sub-band gap response is consistent with previous contactless measurements [111], and provides an upper limit that is below the noise floor of previous measurements [106].

The same analysis described above is repeated using above-band-gap light at 405 nm, and is plotted in the right of figure 5-13, where the response is constant over all chopping frequencies measured; this indicates that thermal effects are minimal, and acts as a control to demonstrate a purely photoconductive response. Because the absorption length of 405 nm light is estimated to be around 500 nm (i.e. deeper than the hyperdoped layer) from previous low-temperature absorption measurement in pure silicon [27], the value G used for the 405 nm light certainly includes carriers generated in the substrate. Therefore, the measured $\Delta\sigma_{\text{sheet}}/G_{\text{sheet}}e$ cannot be used

to estimate a mobility-lifetime product for either holes or electrons in the S-doped region, but represents an upper bound. It has been shown that holes have a larger value for $\mu_h\tau_h$ [105] than electrons.

Using low temperatures to perform photoconductivity measurements has increased the sensitivity over previous room-temperature measurements by freezing out carriers and decreasing the dark conductivity. This enables the measurement of an upper limit of the $\mu_e\tau_e$ product that is nearly two orders of magnitude lower than previously measured in this material system. Frequency dependence of the photo-response for sub-band-gap, 1550 nm light was used as a tool to differentiate between a thermal photo-response and the non-thermal (possibly photoconductive) response. The response from above-band gap, 405 nm light was much stronger and did not have any frequency dependence, presumably because it was not appreciably heating the sample, and is used as a control.

5.5 Conclusion

Using low-temperature, proper design of the contacts, and selective doping increased the sensitivity of these photoconductivity measurements over previous efforts [106], and enabled for the first time to measure an actual photo-response in PLM Si:S using sub-band gap photons. The results presented here provide an upper limit of $\mu_e\tau_e$, which was evaluated by measuring a change in the conductivity by excited carriers from an IB into the CB with sub-band gap light. It was estimated that at 36K, the photo-excited electrons had $\mu_e\tau_e$ of less than $2.5 \times 10^{-}9$ cm$^2/V$. However, how does this result compare compare to Shockley-Reed-Hall (SRH) recombination statistics?

To explore this question, we'll compare the result presented here to literature values of the capture cross-section of S in Si. Grimmeiss measured an electron capture cross-section of $\sigma_e = 2 \times 10^{-15} cm^2$ using deep-level transient spectroscopy [41]. Using this capture cross-section, we can estimate the lifetime associated with a trapping rate for when traps are completely empty:

$$\tau_{e0} = \frac{1}{N_T \sigma_e v_{th}} \tag{5.9}$$

The value of $1/\tau_{e0}$ is a parameter used in SRH statistics that signifies the "probability per unit time that an electron in the conduction band will be captured for the case where all traps are empty are all empty, and, consequently, in a position to capture electrons" [130]. The lifetime of carriers measured in this experiment should be much longer than τ_{e0} because it is likely that the majority of traps are occupied at low temperature and are thus unable to trap an electron (see Appendix B for a discussion on how τ_e and τ_{e0} relate).[3] However, estimation of τ_{e0} gives us a lower limit for the effective electron lifetime, τ_e. If we assume the density of trap states is equal to the sulfur concentration ($N_T = 1.2 \times 10^{20}$ cm^{-3}), use the electron capture cross section as the value reported by Grimmeiss and the appropriate constants [38] for the thermal velocity of electrons in Si, we estimate $\tau_{e0} = 2ps$ at 36 K, which is on the order of thermalization time for an excited carrier [36].

Now, in order to compare this estimated value of τ_{e0} to the results to the $\mu_e\tau_e$ product measured using photoconductivity, an estimate of mobility for carriers in the CB for these samples at 36 K is needed. The Hall effect measured mobility and sheet carrier concentration in a sample which received an identical dose and PLM treatment as the photoconductivity sample is reproduced in figure 5-14. At 36 K, the measured mobility is ca. $15\frac{cm^2}{Vs}$. However, at this S concentration, the majority carrier transport at low temperatures is dominated by a thermally-activated hopping mechanism in the IB [147], and is why the this insulating sample does not exhibit a Hall carrier freeze-out, but a Hall mobility freeze-out. The CB most likely has a higher mobility for carriers than the one measured in Hall, but we can use this as a lower limit on mobility; this yields an upper limit on lifetime of τ_e <130 ps. Considering, the mobility could be in the neighborhood of the value measured at room temperature, $162\frac{cm^2}{Vs}$, the actual value of τ_e could be an order of magnitude

[3]Additionally the number of traps that are emptied via photo-excitation is estimated to be less than one in a million. This estimate is made by taking the generation rate and dividing it by the number of S atoms.

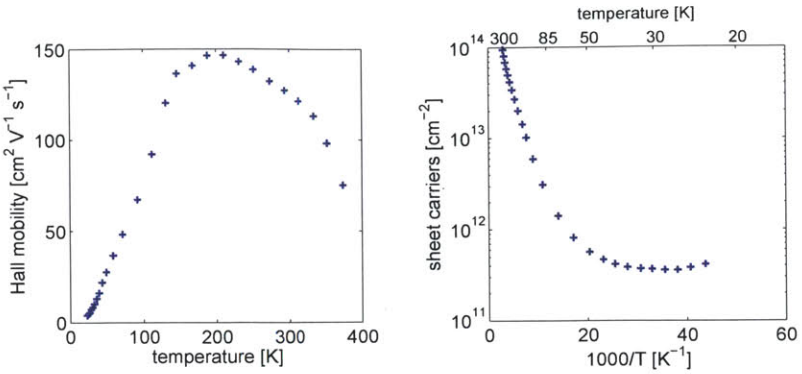

Figure 5-14: Hall data measured by Winkler [146] for a Si:S prepared prepared which received an identical dose and PLM treatment as the photoconductivity discussed in this chapter (implant dose of 3×10^{15} cm^{-2} and peak S concentration of 1.2×10^{20} cm^{-3}).

lower.

This result also indicates that the IB band must be partially un-occupied. Using the analysis in Appendix B, we can relate τ_e and τ_{e0} via a generation rate and the IB occupation probability. Using an effective layer thickness of 270 nm, we can estimate the volumetric generation rate using $G_{\text{sheet}}/d_{\text{eff}} = 2 \times 10^{23}$ carriers cm^{-2}s^{-1}. For N_T, we can assume that this is roughly equal to the S concentration. Under high injection conditions (i.e. the vast majority of traps are emptied optically), then we can use Equation B.15 to estimate τ_{e0}.

$$\tau_{e0_{\text{High Injection}}} = \tau_e^2 \frac{G}{N_T} < 3 \times 10^{-17} \text{ s} \tag{5.10}$$

Clearly, this result is non-physical (i.e. five orders of magnitude faster than thermalization times), so it is unlikely that we are in the high-injection regime. Next we can estimate a τ_{e0} for the low-injection regime. Assuming that the majority of holes in the IB result from the presence of shallow acceptors, we can approximate equation B.18 as $\tau_e \approx \tau_{e0}/f_{pT0}$, where $f_{pt,0}$ is the probability of a trap state being occupied by a hole in the dark. If we assume that the value of τ_e is consistent SRH recombination and the previously published value of the electron capture cross-section, then we see:

$$f_{\mathrm{pt},0} \geq \frac{\tau_{\mathrm{e}0}}{\tau_{\mathrm{e}}} = 0.015 \tag{5.11}$$

This means, that for our result to be consistent with the SRH statistics and the previously reported electron capture cross-section, then we must have a hole occupation rate that is above 1.5% (and below 15% if we assume an upper limit of the measured mobility at room temperature). If hole occupation rates are lower than 1.5%, then this system has faster recombination than predicted by SRH. The concentration of acceptors present in this material is currently unknown. However, compensating defects have been seen in Si:S before when prepared by thermal annealing [65]; additionally vacancies (which may result from PLM treatment) are known to form acceptors states when paired with with oxygen in CZ Si wafers [34]. Additionally, the fact that hopping conduction at low temperature at this S concentration is possible indicates that there must be some amount of compensation [87].

Current work on low-temperature Hall measurements are being performed to estimate IB occupation rates using various compensation ratios with B. Until occupation rates are known, we won't be able to generate a full picture of the recombination dynamics in this material. For now, it is clear that the results here are non inconsistent with SRH and the previous published electron capture cross-section [41].

Chapter 6

Conclusion and Future Directions for IB Materials

In this thesis, we've explored the band structure, optical absorption and transport properties of S-doped silicon in the context of developing a material for an IB PV device. Using the criteria for screening potential IB PV materials outlined in section 1.6, we can eliminate S-doped Si as a candidate IB PV material.

6.1 Estimate of Figure of Merit for Si:S System

We have shown through optical measurements that Si:S samples with S concentrations of 2.1×10^{20} cm^{-3} and below have a measurable optical gap between the IB states and the CB. This indicates that S concentrations must be kept below this limit to make a material that has an electronic structure suitable for IB PV (i.e. to meet criterion #1).

Measurements presented in this thesis allow empirical determination of ν_e for samples with concentrations below the IMT critical concentration. Combining the optical data and the photoconductivity, an upper bound on ν_e can be calculated for a sample with a 1.2×10^{20} S cm^{-3} peak concentration. Low-temperature photoconductivity measurements yielded an upper bound on $\mu_e \tau_e$ of 2.5×10^{-9} cm^2/V for carrier generated using 1550 nm light. From Figure 4-11, α is 8300 cm^{-1} for 1550 nm photons.

For an upper bound of V_{bi} (which is set to the Si band gap potential of 1.1 V) and a value of $c = 2$ (which Reference [63] deems suitable), an upper of limit on the figure of merit described in Equation 1.3 is calculated:

$$\nu_e < \frac{1}{2^2}(1.1\text{V})(2.5 \times 10^{-9}\ \text{cm}^2/\text{V})(8300\ \text{cm}^{-1})^2 = 0.05 \tag{6.1}$$

To make a useful IB absorber layer, ν_e must be greater than unity; thus, S-doped Si is an unsuitable material system for an IB absorber layer.

It is important to note that we are assuming that the optical transition that is excited in both optical and low-temperature photoconductivity experiments is from the IB to CB, and hence the subscript "e" is used on ν_e.[1] Were Si:S to have a sufficiently high ν_e, then further characterization would be needed to verify both optical strength VB $\rightarrow$ IB, transitions and estimate $\mu_h\tau_h$ for holes, which would require depleting the IB via counter-doping.

6.2 Is Impurity Band PV Possible?

In this thesis, we've demonstrated that Si:S will not make a suitable IB PV device. However, what other semonductor:impurity combinations look promising? What directions should future research take on this topic?

There are two research paths moving forward to verify if IB PV can enhance the efficiency of solar devices. Either researchers can pursue materials that may exhibit lifetime recovery, or we can assume that lifetime recovery is not real and try to find deep level impurities that have a strong optical cross-section but a weak electrical cross-section. The next two sub-sections will discuss the possible future directions for each pursuit.

[1] See Reference [123] and section 2.5 for a discussion on this topic.

6.2.1 Search for Lifetime Recovery

The original concept of the impurity band approach envisioned incorporating deep-level dopants at sufficiently high levels to drive an insulator-to-metal (IMT) transition and form a metallic impurity band within the band gap; at dopant concentrations below the IMT, non-radiative recombination would dominate, but above the IMT it was theorized that lifetime recovery would occur and suppress non-radiative recombination [74]. As discussed in Section 1.4.1, despite claims of lifetime recovery in Si:Ti, no definitive work has demonstrated this effect. Additionally recent theoretical work suggests sufficient lifetime recovery is impossible, and that even at dopant concentrations above the IMT, lifetime will not be significantly reduced from the independent-dopant limit [63].

While the debate around the theory of lifetime recovery still continues, more experimental work needs to be done to understand the interaction of deep-level dopants. In this thesis, we've shown that lifetime recovery is not possible in Si:S because substantial broadening of the IB at the IMT ruins the electronic structure, but dopants that have a different valence structure might not lead to substantial broadening. Further work using transition metals in Si may be a promising area. Further work on Si:Ti may prove successful if crystalline materials can be made using PLM of Ti-implanted Si, however, all the work on Si:Ti has been performed on layers that were not single crystalline (*i.e.* had undergone cellular breakdown during PLM treatment).

6.2.2 Enhanced Efficiency from IB PV in the Absence of Lifetime Recovery

While we have shown that Si:S is unsuitable for IBPV, we can try to make estimates for other material systems to see what possible other combinations of host semiconductor and impurity are promising. To do this, we'll estimate the value of $\nu_{e,h}$ by collecting literature values of optical and electrical cross-sections for impurities in Si at dilute concentrations; using these values, we can estimate mobility, lifetime, and absorption to estimate the figure of merit for both electrons and holes.

As demonstrated previously in equation 4.27, the absorption coefficient for a particular transition involving deep levels scales linearly with impurity concentration. We'll need to evaluate both transition (VB→IB and IB→CB), and thus we label our absorption coefficiency as α_{h} and α_{e} for both respective transitions. In an impurity band material, the IB should be partially full, so that both VB→IB and IB→CB transitions are both possible. To reflect this, we'll alter equation 4.27 to reflect this by introducing a term that represents the occupation probability of a trap state in the dark, f_{T0}. We assume low-injection conditions, and thus $f_{\mathrm{T0}} \approx f_{\mathrm{T}}$, where f_{T} represents the trap occupation rate during illumination. The altered equations are shown below:

$$\alpha_{\mathrm{h}} = f_{\mathrm{T0}} N_{\mathrm{T}} \sigma_{\mathrm{O_h}} \tag{6.2}$$

$$\alpha_{\mathrm{e}} = f_{\mathrm{T0}} N_{\mathrm{T}} \sigma_{\mathrm{O_e}} \tag{6.3}$$

We can assume that the lifetimes are approximated by the trapping rates for both electrons and holes with a deep level impurity. We'll use a modified version of SRH recombination to describe the trapping rates of electrons and holes into the IB, respectively in a low-injection limit (see Appendix B). The value of N_{T} is now modified by the pre-factor $1 - f_{\mathrm{T0}}$ to estimate the number of empty traps (see Appendix B and Equation B.18 for full derivation and justification).

$$\tau_{\mathrm{e,h}} = \frac{1}{(1 - f_{\mathrm{T0}}) N_{\mathrm{T}} \sigma_{\mathrm{e,h}} v_{\mathrm{th_{e,h}}}} \tag{6.4}$$

To estimate mobility, we optimistically assume impurities are not ionized and thus electron and hole mobility is limited only by lattice scattering only, $\mu_{\mathrm{latt_{e,h}}}$, and neutral impurities, $\mu_{\mathrm{ni_{e,h}}}$ [70].

$$\frac{1}{\mu_{\mathrm{e,h}}} = \frac{1}{\mu_{\mathrm{latt_{e,h}}}} + \frac{1}{\mu_{\mathrm{ni_{e,h}}}} \tag{6.5}$$

$$\mu_{\mathrm{ni_{e,h}}} = \frac{2\pi e^3 m^*_{\mathrm{e,h}}}{5N_{\mathrm{T}}\epsilon h^3} \tag{6.6}$$

Now, if we combine equations 6.2, 6.3, 6.4, and 6.5 we can estimate all the necessary parameters for $\nu_{\mathrm{e,h}}$ for a semiconductor:impurity combination using only known values for electrical and optical cross-sections. This is shown in Figure 6-1 for Si:S; in the top left, the absorption scales is estimated using the optical cross-section estimated in Chapter 4, the electron capture cross-section is estimated using literature values from Grimmeiss [41], and a half-full band ($f_{\mathrm{T}} = 0.5$) is assumed. Doing this, an upper limit of $\nu_{\mathrm{e}} < 0.002$ is found at high N_{T}, which is lower than than the empirical value. However if a value of $f_{\mathrm{T}} = 0.985$ is used (see section 5.5), then $nu_{\mathrm{e}} < 0.6$. While a direct comparison between the measured ν_{e} and the estimate using equations 6.3 through 6.5 is not possible until the band occupation rate is known, this simple analysis indicates that higher N_{T} does yield a higher ν and makes a justification for hyperdoping.

Now, in the very high impurity limit, mobility will be purely limited by neutral impurity scattering; if we are in this regime, an optimistic estimate of $\nu_{\mathrm{e,h}}$ can be made using our previously stated assumptions. This assumption is optimistic because if impurities were ionized, mobility would be reduced further [70]. An actual device would likely have a band that is half-full in order to allow both the promotion of electrons and holes. Thus, an upper limit of $\nu_{\mathrm{e,h}}$ for a half-full band (i.e. $f_{\mathrm{T}} = 0.5$) is given in 6.7.

$$\nu_{\mathrm{e,h}} \leq \frac{1}{c^2} E_{\mathrm{g}} \left(\frac{\pi q^2 m^*_{\mathrm{e,h}}}{5\epsilon h^3} \right) \frac{\sigma^2_{\mathrm{O}_{e,h}}}{v_{\mathrm{th}_{e,h}} \sigma_{\mathrm{e,h}}} \tag{6.7}$$

From equation 6.7, we can see that at high impurity concentration, the parameter is not dependent on N_{T}, which means that only the optical and carrier capture cross-sections are needed to estimate an upper limit of $\nu_{\mathrm{e.h}}$.

To search for an appropriate dopant in Si that that may yield an IB with a suitably high figure of merit, a compilation of literature values of the electrical and optical capture cross-sections for both holes and electrons are listed below for various

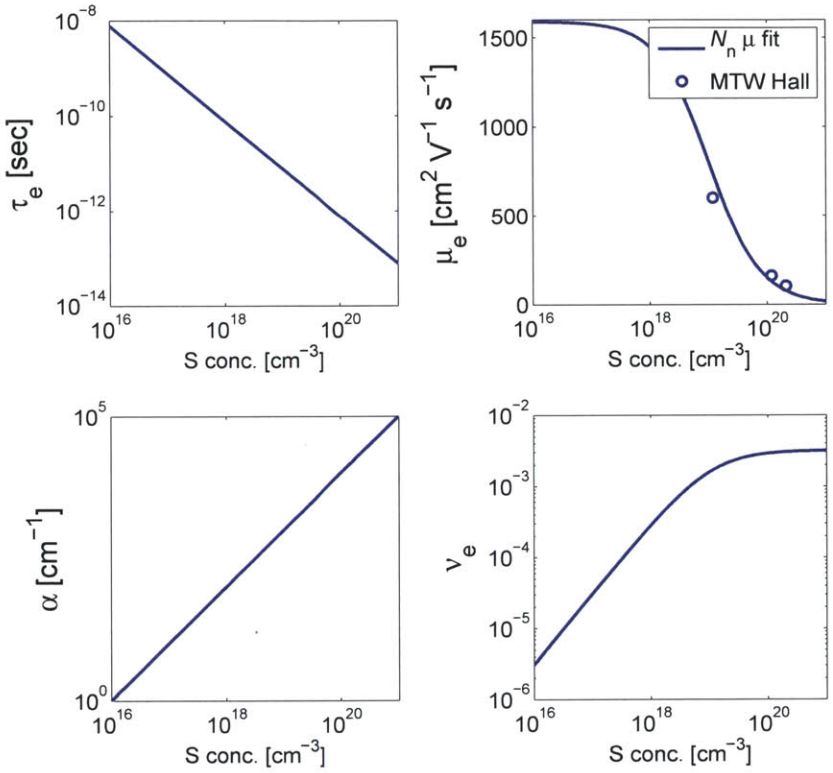

Figure 6-1: Scaling estimates of μ_e, τ_e, and α_e show that higher impurity concentration yields a higher ν_e for Si:S. A value of c=2 is used. Room temperature measurements of the mobility using Hall are reproduced in top right from [146]. Calculations are for T=300 K.

impurities in silicon. For the optical cross-sections reported here, the value at the peak of spectrum is reported. A more rigorous analysis would require estimating these values spectrally and weighting them with solar spectrum. Both the electrical and optical cross-sections are then used to estimate a figure of merit using Equation 6.7 and the results are plotted in Figure 6-2.

Element	Energy [meV]	σ_e	σ_{O_e}	Reference(s)
S (D)	$E_C - 250$	2×10^{-15}	2×10^{-16}	[92], [41]
In (A)	$E_V + 157$	2×10^{-22}	-	[136]
Au (A)	$E_C - 550$	7×10^{-17} to 4×10^{-15}	2×10^{-17}	[94], [78],[22]
Pt (D)	$E_C - 250$	3×10^{-17}	2×10^{-16} to 4×10^{-14}	[22], [12]
Fe_i (D)	$E_V + 380$	5×10^{-14}	2×10^{-16}	[78],[149]
Ag (D)	$E_V + 260$	2×10^{-15}	2×10^{-15}	[94], [140]
Zn (A)	$E_V + 310$	5×10^{-16} to 10^{-15}	3×10^{-15}	[133]
Zn (dA)	$E_V + 580$	10^{-20} to 10^{-16}	10^{-17} to 10^{-15}	[133]

Table 6.1: List of both both electrical and optical cross-sections for electrons. All values listed are in cm^2 and optical cross-sections are for the maximum reported value for given spectrum.

Element	Energy [meV]	σ_h	σ_{O_h}	Reference(s)
In (A)	$E_V + 157$	1×10^{-13}	4.5×10^{-17} to 2×10^{-16}	[124],[22]
Au (A)	$E_V + 630$	8×10^{-15}	1×10^{-17} to 2×10^{-16}	[22]
Pt (A)	$E_V + 200$	1×10^{-17} to 6×10^{-15}	2×10^{-17}	[94], [22]
Pt (D)	$E_C - 250$	1×10^{-16}	5×10^{-15} to 1×10^{-14}	[12], [22]
Fe_i (D)	$E_V + 380$	7×10^{-17}	3×10^{-17}	[78],[149]
Ag (A)	$E_C - 290$	7×10^{-16}	5×10^{-15}	[94], [140]
Zn (A)	$E_V + 310$	10^{-14} to 10^{-13}	2×10^{-16}	[133]
Zn (dA)	$E_V + 580$	10^{-16} to 10^{-13}	2×10^{-15}	[133]

Table 6.2: List of both both electrical and optical cross-sections for holes. All values listed are in cm^2 and optical cross-sections are for the maximum reported value for given spectrum.

In Figure 6-2, the acceptor, double acceptor, and donor levels are labeled with (A), (dA), and (D), respectively. The ranges of values for the capture cross listed in Tables 6.1 and 6.2 are reflected in Figure 6-2 by showing a range of calculated values. For an IB PV device to work, the creation and extraction of both electrons and holes are necessary, thus a high value of ν_e and ν_h would be required for an efficient device.

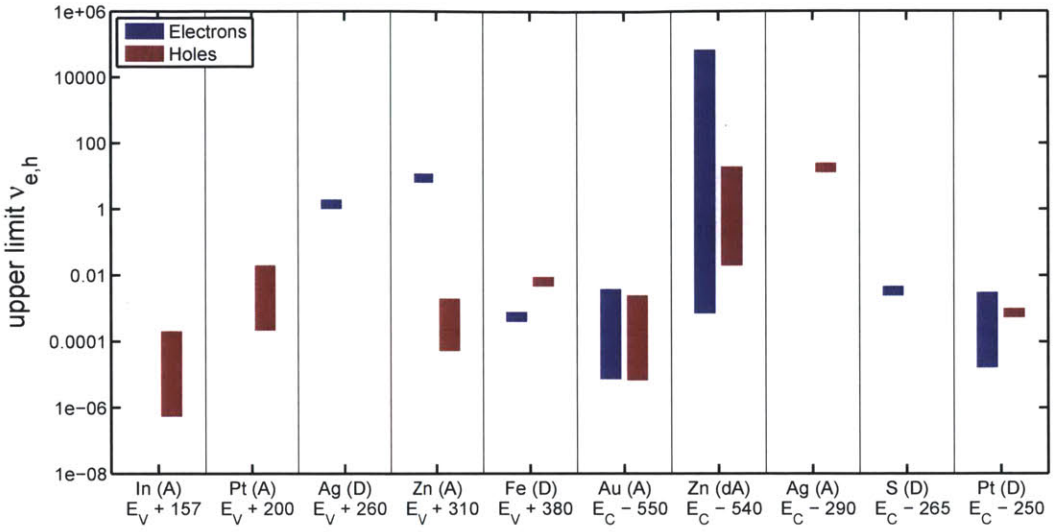

Figure 6-2: For values compiled in tables 6.1 and 6.2, an estimate of ranges of $\nu_{e,h}$ is plotted above using Equation 6.7 for different impurities in Si. The labels 'D', 'A', and 'dA' denote donor, acceptor, and double acceptor levels, respectively.

Based on this criteria, the only impurity that holds any promise would be the double acceptor level introduced by Zn^+. However, the fact that this donor level is ionized means that mobility will certainly be lower that is estimated by Equation 6.5.

Additionally, this analysis makes no assumption about spectral dependence on the optical cross-section, and a more detailed analysis would be necessary to actually assess the efficiency potential of these impurities in Si. This estimate is meant to be a quick and easy way to identify new impurities that may work for IBPV.

6.3 Impurity PV in Compensated Materials

There have been numerous theoretical studies on whether deep levels can enhance efficiency while still maintaing SRH recombination statistics (i.e. no lifetime recovery) by putting deep-level impurities in the absorber layer in a traditional p-n junction solar cells. The equation describing generation and recombination (both optical and phonon-assisted) via defects are well outlined in several References [139, 119, 118]. This device would be very different than the one described in this thesis, in the case that the device is diffusion-limited, and not drift-driven. In the original theory paper

by Keevers and Green [59], deep levels were introduced in the n-type absorber layer using In acceptor impurities and a small increase in short circuit current was seen with increased In content, with only a minor decrease in open-circuit voltage and resulting in a slight increase in overall efficiency (less than 1.5% relative increase when compared to a high efficiency cell). The impurity In was chosen for their study because the trap level was close enough to the VB that promotion to that acceptor level is completely thermal; this means that a two-photon process is not necessary to generate carriers via sub-band gap light. Additionally, because the capture electron cross-section for In is so low (see Table 6.1), the lifetimes of carriers can be kept long. This idea of incorporating compensated deep-levels to increase efficiency in p-n junction solar cell has been studied by many people theoretically [9, 156, 155, 8] that have shown that this idea can increase efficiency. However, this idea has never been brought to practice.

Despite this, one of the promising things that these devices structures possess is that it decouples the necessity for a two-photon transition. This means that elements which have a large ν for one carrier type but not the other could be used in this type of device. It is also important to note that the figure of merit for such a material would use kT in place of V_{bi} because it is a diffusion-limited device.

6.4 Final Thoughts

In this this thesis, we've explored how the fundamental material properties change at hyperedoped concentrations as compared to dilute concentrations within the context of impurity-band photovoltaics. When work began on this thesis, it was unknown how the material properties would change at hyperdoped concentrations. As a result of the work in this thesis, we've learned that the physics that describe these material properties don't deviate substantially from the physics developed for deep-level impurities at dilute concentrations.

In Chapter 3, we learned that changes in the electronic structure are predictable and number of deep-level states introduced by S scales with S concentration. The

only noticeable change in bulk electronic structure occurs when the S concentration exceeds that of the critical concentration to drive an insulator-to-metal transition [147].

In Chapter 4, we measured both the energetic location and width of the impurity band states. We learned that the location of the IB matches closely to the defect levels measured at dilute concentrations. Additionally we learned that the optical cross-section can be modeled in both magnitude and spectral shape using an optical cross-section that describes deep-levels at dilute concentrations.

Finally, in Chapter 5, we measured the photo-excited transport properties of electrons to understand the recombination statistics in hyperdoped materials. While further work is needed to estimate the occupation probability of the impurity band, we can say that there is no current evidence that suggests that recombination statistics differ from theories developed for isolated deep levels [130].

From the knowledge generated in Chapters 3-5, we can confidently make the assumption that models and theories that describe the band structure, optical excitation, and recombination statistics mimic those developed at dilute concentration. This assumption allows us to estimate the figure of merit for both holes and electrons at supersaturated concentrations. These estimates point to new materials that can ultimately lead to a successful IB PV absorber layer material.

Appendix A

Unsteady Heat Transfer Model

This section is meant to provide further detail on the simple heat transfer model discussed in Ch. 5. We start with the simple 1-D unsteady heat transfer equation [83]:

$$\frac{dT}{dt} = \frac{k}{\rho c}\frac{\partial^2 T}{\partial x^2} \tag{A.1}$$

In the above equation, k is the thermal conductivity, ρ is the density, and c is the thermal capacitance. To generalize this analysis, I non-dimensionalize equation A.1:

$$\frac{\partial \theta}{\partial \zeta} = \frac{\partial^2 \theta}{\partial \eta^2} \tag{A.2}$$

$$\theta = \frac{T - T_\mathrm{b}}{T_\mathrm{f} - T_\mathrm{b}}, \qquad \eta = \frac{x}{L}, \qquad \zeta = \frac{tk}{\rho c L^2} \tag{A.3}$$

Where $T_\mathrm{f} = T_\mathrm{s}$ is the steady state surface temperature for a constant radiative heat flux q_laser, and is determined simply by: $T_\mathrm{f} - T_\mathrm{b} = \frac{q_\mathrm{laser} L}{k}$.

The boundary conditions assume a constant base temperature and that the temperature gradient at the surface matches that of the incoming light, which is varying with time as a sinusoid with a dimensionless frequency, ω, which is in "units" of inverse ζ.

$$\theta|_{\zeta=1} = 0 \tag{A.4}$$

$$\left.\frac{\partial\theta}{\partial\zeta}\right|_{\zeta=0} = \frac{Lq_{\text{laser}}}{k(T_{\text{f}} - T_{\text{b}})}(0.5 + 0.5sin(\omega\zeta)) \tag{A.5}$$

Using the above un-steady equations and boundary conditions, we can use a numerical solver to estimate the peak to peak change in surface temperature for different laser chopping frequencies. The results from this are shown in figure 5-6

Appendix B

SRH recombination with generation from traps

Here, we'll go over the recombination rates of traps assuming that the only photo-generated transition is from occupied trap states into the conduction band. Excellent references on recombination and generation (both optical and phono-assisted) via defect levels can be found in References [139, 119, 118, 130]. We'll start with equation (3.8) from Shockley and Read's original paper [130], which described the rate at which carriers are captured from the conduction band and into a trap, U_{n}:

$$U_{\mathrm{n}} = C_{\mathrm{n}} f_{\mathrm{pT}} n - C_{\mathrm{n}} f_{\mathrm{T}} n_1 \tag{B.1}$$

where f_{pT} and f_{T} are the probabilities that a trap is unoccupied or occupied, respectively. The value of n_1 describes the number of carriers in the conduction band if the Fermi Energy was degenerate with the trap energy. We define the capture rate for all traps being empty, C_{n} as:

$$C_{\mathrm{n}} = \frac{1}{\tau_{\mathrm{e0}}} = N_{\mathrm{T}} \sigma_{\mathrm{e}} v_{\mathrm{th_e}} \tag{B.2}$$

Additionally, we need to know the trap occupation probability. To estimate trap occupation probabilities, we use charge neutrality and define it using trap donor density (N_{T}), acceptor density (N_{A}), dark carriers (n_0), and number of electrons in

traps (n_{T0}). In this analysis, we assume that traps are donors.

$$N_T - N_A = n_0 + n_{T0} \tag{B.3}$$

Now, if we assume that the trap states are completely full at zero temperature for an uncompensated system[1] (i.e. $N_A = 0$), then we can approximate the trap occupation probabilities for holes in the dark (f_{pT0}) and under illumination (f_{pT}):

$$f_{pT0} = \frac{n_0 + N_A}{N_T} \tag{B.4}$$

$$f_{pT} = \frac{n_0 + N_A + \Delta n}{N_T} \tag{B.5}$$

Similarly, trap occupation probabilities for electrons in the dark (f_{T0}) and under illumination (f_T) are estimated as:

$$f_{T0} = \frac{n_{T0}}{N_T} = 1 - f_{pT0} \tag{B.6}$$

$$f_T = \frac{n_T - \Delta n}{N_T} = 1 - f_{pT} \tag{B.7}$$

Now if we use equation B.1 and assume steady-state conditions, we set the net recombination rate to zero (i.e. $U_n = 0$). To account for carriers that are photo-generated from traps into the conduction band, we add the term, G.

$$0 = C_n f_{pT}(n_0 + \Delta n) - C_n f_T n_1 - G \tag{B.8}$$

Re-arranging equation B.8 and using equations B.5 and B.7, we write the following:

[1]This is likely true for a double donor, such as S in Si. For a single-electron donor, each donor atom introduces a spin-up and spin-down state, and would create a half-full band in an uncompensated system.

$$0 = C_{\mathrm{n}}\left(\frac{n_0 + N_{\mathrm{A}} + \Delta n}{N_{\mathrm{T}}}\right)(n_0 + \Delta n) - C_{\mathrm{n}}\left(1 - \frac{n_0 + N_{\mathrm{A}} + \Delta n}{N_{\mathrm{T}}}\right) n_1 - G \qquad \text{(B.9)}$$

We re-write equation B.9 in terms of Δn and multiply by $\frac{N_T}{C_n}$ to get:

$$\begin{aligned} 0 =& \Delta n^2 \\ &+ \Delta n\,(2n_0 + N_{\mathrm{A}} + n_1) \\ &+ \left(n_0(n_0 + N_{\mathrm{A}}) + n_1(n_0 + N_{\mathrm{A}}) - n_1 N_{\mathrm{T}} - G\frac{N_{\mathrm{T}}}{C_{\mathrm{n}}}\right) \end{aligned} \qquad \text{(B.10)}$$

In the dark, when $G = 0$, we know that $\Delta n = 0$, and thus we can write the following using equation B.10:

$$0 = (n_0(n_0 + N_{\mathrm{A}}) + n_1(n_0 + N_{\mathrm{A}}) - n_1 N_{\mathrm{T}}) \qquad \text{(B.11)}$$

We can use equation B.11 to greatly simplify the equation B.10.

$$\begin{aligned} 0 =& \Delta n^2 \\ &+ \Delta n\,(2n_0 + N_{\mathrm{A}} + n_1) \\ &- G\frac{N_{\mathrm{T}}}{C_{\mathrm{n}}} \end{aligned} \qquad \text{(B.12)}$$

We can use the quadratic formula to solve for Δn for a set of given parameters.

$$\Delta n = \frac{-(2n_0 + N_{\mathrm{A}} + n_1) \pm \sqrt{(2n_0 + N_{\mathrm{A}} + n_1)^2 + 4G\frac{N_{\mathrm{T}}}{C_{\mathrm{n}}}}}{2} \qquad \text{(B.13)}$$

Note in the above equation, the the only solution that yields positive Δn is when the $\pm$ is a $+$. Now under high injection, if we assume that $4G\frac{N_T}{C_n} >> (2n_0 + N_A + n_1)^2$, we can get the following expression after using equation B.13:

$$\Delta n = \sqrt{\frac{GN_{\mathrm{T}}}{C_{\mathrm{n}}}} \tag{B.14}$$

If we make the substitution that $\Delta n = G\tau_{\mathrm{e}}$, then we can estimate the effective lifetime of electrons:

$$\tau_{\mathrm{e_{HighInjection}}} = \sqrt{\frac{N_{\mathrm{T}}}{GC_{\mathrm{n}}}} = \sqrt{\frac{\tau_{e0}N_{\mathrm{T}}}{G}} \tag{B.15}$$

Equation B.15 will most likely be used when the traps are completely or nearly full in the dark and photo-generation is what empties the band (i.e. $f_{\mathrm{pT0}} << f_{\mathrm{pT}}$ or $f_{\mathrm{T0}} << f_{\mathrm{T}}$).

Now, under low injection, we assume that $(4GN_{\mathrm{T}}/C_{\mathrm{n}}) << (2n_0+N_{\mathrm{A}}+n_1)^2$, which allows us to linearize equation B.13 to estimate the low injection Δn. We start by re-arranging equation B.13:

$$\Delta n = (2n_0 + N_{\mathrm{A}} + n_1)\left(-\frac{1}{2} + \frac{1}{2}\sqrt{1 + \frac{4G\frac{N_{\mathrm{T}}}{C_{\mathrm{n}}}}{(2n_0 + N_{\mathrm{A}} + n_1)^2}}\right) \tag{B.16}$$

Using equation B.16, we can use the Taylor series expansion of $\sqrt{1+x} \approx 1 + \frac{1}{2}x$ around $x = 0$ for small values of x, and get the following:

$$\Delta n = \frac{GN_{\mathrm{T}}}{C_{\mathrm{n}}(2n_0 + N_{\mathrm{A}} + n_1)} \tag{B.17}$$

Again, substituting the relation $\Delta n = G\tau_{\mathrm{e}}$ into equation B.17, we estimate the effective lifetime of electrons:

$$\tau_{\mathrm{e_{LowInjection}}} = \frac{N_{\mathrm{T}}}{C_{\mathrm{n}}(2n_0 + N_{\mathrm{A}} + n_1)} = \tau_{\mathrm{e0}}\left(\frac{N_{\mathrm{T}}}{2n_0 + N_{\mathrm{A}} + n_1}\right) \tag{B.18}$$

Now in the case where n_1 is small and most of the traps are emptied by compensation, this is simply:

$$\tau_{\mathrm{e}} = \tau_{\mathrm{e0}}/f_{\mathrm{pT0}} \tag{B.19}$$

This final result provides the basis for comparison between the electron capture

cross-section measured for Si doped with S at low concentration to the S-hyperdoped sample studied in Chapter 5.

Bibliography

[1] V.V. Afanasév. *Internal photoemission spectroscopy: principles and applications.* Elsevier, Oxford, United Kingdom, 2008.

[2] V.V. Afanasév and A. Stesmans. Internal photoemission at interfaces of high-k insulators with semiconductors and metals. *Journal of Applied Physics*, 102:081301, 2007.

[3] M.N. Alexander and D.F. Holcomb. Semiconductor-to-metal transition in n-type group IV semiconductors. *Reviews of Modern Physics*, 40:815, 1968.

[4] E. Antolín, A. Martí, J. Olea, D. Pastor, G. González-Díaz, I. Mártil, and A. Luque. Lifetime recovery in ultrahighly titanium-doped silicon for the implementation of an intermediate band material. *Applied Physics Letters*, 94:042115, 2009.

[5] C.L. Archer. Evaluation of global wind power. *Journal of Geophysical Research*, 110:D12110, 2005.

[6] M.J. Aziz and T. Kaplan. Continuous growth model for interface motion during alloy solidification. *Acta Metallurgica*, 36:2335, 1988.

[7] M.J. Aziz, C.W. White, J. Narayan, and B. Stritzker. In V.T. Nguyen and A.G. Cullis, editors, *Energy Beam-Solid Interactions and Transient Thermal Processing.* Editions de Physique, Paris, 1985.

[8] G. Azzouzi and M. Chegaar. Impurity photovoltaic effect in silicon solar cell doped with sulphur A numerical simulation. *Physica B*, 406:1773, 2011.

[9] G. Beaucarne, A.S. Brown, M.J. Keevers, R. Corkish, and M.A. Green. The impurity photovoltaic (IPV) effect in wide-bandgap semiconductors: an opportunity for very-high-efficiency solar cells? *Progress In Photovoltaics: Research and Applications*, 10:345, 2002.

[10] B.P. Bob, A. Kohno, S. Charnvanichborikarn, J.M. Warrender, I. Umezu, M. Tabbal, J.S. Williams, and M.J. Aziz. Fabrication and subband gap optical properties of silicon supersaturated with chalcogens by ion implantation and pulsed laser melting. *Journal of Applied Physics*, 107:123506, 2010.

[11] J.A. Borders. Formation of SiC in silicon by ion implantation. *Applied Physics Letters*, 18:509, 1971.

[12] S. Braun, H.G. Grimmeiss, and K. Spann. Photoionization cross sections in platinum-doped silicon. *Journal of Applied Physics*, 48:3883, 1977.

[13] S.P. Bremner, M.Y. Levy, and C.B. Honsberg. Limiting efficiency of an intermediate band solar cell under a terrestrial spectrum. *Applied Physics Letters*, 92:171110, 2008.

[14] M. Brinza, J. Willekens, M.L. Benkhedir, E.V. Emelianova, and G.J. Adriaenssens. Photoconductivity methods in materials research. *Journal of Materials Science: Materials In Electronics*, 16:703, 2005.

[15] F.C. Brown, R.Z. Bachrach, and M. Skibowski. $L_{2,3}$ threshold spectra of doped silicon and silicon compounds. *Physical Review B*, 15:4781, 1977.

[16] J.E. Carey, C.H. Crouch, M. Shen, and E. Mazur. Visible and near-infrared responsivity of femtosecond-laser microstructured silicon photodiodes. *Optics Letters*, 30:1773, 2005.

[17] R. Carlson. Sulfur in silicon. *Journal of Physics and Chemistry of Solids*, 8:81, 1959.

[18] R.D. Carson and S.E. Schnatterly. X-ray emission from core excitons. *Physical Review Letters*, 59:319, 1987.

[19] H. Castán, E. Pérez, H. García, S. Dueñas, L. Bailón, J. Olea, D. Pastor, E. García-Hemme, M. Irigoyen, and G González-Díaz. Experimental verification of intermediate band formation on titanium-implanted silicon. *Journal of Applied Physics*, 113:024104, 2013.

[20] T.G. Castner, N.K. Lee, G.S. Cieloszyk, and G.L. Salinger. Dielectric anomaly and metal-insulator transition in *n*-type silicon. *Physical Review Letters*, 34:1627, 1975.

[21] A. Chantre, G. Vincent, and D. Bois. Deep-level optical spectroscopy in GaAs. *Physical Review B*, 23:5335, 1981.

[22] J.W. Chen and A.G. Milnes. Energy-levels in silicon. *Annual Review of Materials Science*, 10:157, 1980.

[23] E.M. Conwell. Impurity band conduction in germanium and silicon. *Physical Review*, 103:51, 1956.

[24] C.H. Crouch, J.E. Carey, M. Shen, E. Mazur, and F.Y. Génin. Infrared absorption by sulfur-doped silicon formed by femtosecond laser irradiation. *Applied Physics A*, 79:1635, 2004.

[25] C.H. Crouch, J.E. Carey, J.M. Warrender, M.J. Aziz, E. Mazur, and F.Y. Génin. Comparison of structure and properties of femtosecond and nanosecond laser-structured silicon. *Applied Physics Letters*, 84:1850, 2004.

[26] V.L. Dalal. Simple Model for Internal Photoemission. *Journal of Applied Physics*, 42:2274, 1971.

[27] W.C. Dash and R. Newman. Intrinsic optical absorption in single-crystal germanium and silicon at 77 K and 300 K. *Physical Review*, 99:1151, 1955.

[28] W. Eberhardt, G. Kalkoffen, C. Kunz, D. Aspnes, and M. Cardona. Photoemission studies of 2p core levels of pure and heavily doped silicon. *Physica Status Solidi B*, 88:135, 1978.

[29] P.P. Edwards and M.J. Sienko. Universality aspects of the metal-nonmetal transition in condensed media. *Physical Review B*, 17:2575, 1978.

[30] O. Engstrom and H.G. Grimmeiss. Optical properties of sulfur-doped silicon. *Journal of Applied Physics*, 47:4090, 1976.

[31] E. Ertekin, M.T. Winkler, D. Recht, A.J. Said, M.J. Aziz, T. Buonassisi, and J.C. Grossman. Insulator-to-Metal Transition in Selenium-Hyperdoped Silicon: Observation and Origin. *Physical Review Letters*, 108:026401, 2012.

[32] F. Fabbri, M.J. Smith, D. Recht, M.J. Aziz, S. Gradečak, and G. Salviati. Depth-resolved cathodoluminescence spectroscopy of silicon supersaturated with sulfur. *Applied Physics Letters*, 102:031909, 2013.

[33] H. Fujimori. Dependence on morphology of oxygen precipitates upon oxygen supersaturation in Czochralski silicon crystals. *Journal of The Electrochemical Society*, 144:3180, 1997.

[34] N. Ganagona, B. Raeissi, L. Vines, E.V. Monakhov, and B.G. Svensson. Formation of donor and acceptor states of the divacancy–oxygen centre in p-type Cz-silicon. *Journal of Physics: Condensed Matter*, 24:435801, 2012.

[35] E. García-Hemme, R. García-Hernansanz, J. Olea, D. Pastor, A. del Prado, I. Mártil, and G. González-Díaz. Sub-bandgap spectral photo-response analysis of Ti supersaturated Si. *Applied Physics Letters*, 101:192101, 2012.

[36] R.R. Gattass and E. Mazur. Femtosecond laser micromachining in transparent materials. *Nature Photonics*, 2:219, 2008.

[37] G. González-Díaz, J. Olea, I. Mártil, D. Pastor, A. Martí, E. Antolín, and A. Luque. Intermediate band mobility in heavily titanium-doped silicon layers. *Solar Energy Materials And Solar Cells*, 93:1668, 2009.

[38] M.A. Green. Intrinsic concentration, effective densities of states, and effective mass in silicon. *Journal of Applied Physics*, 67:2944, 1990.

[39] H.G. Grimmeiss, E. Janzén, H. Ennen, O. Schirmer, J. Schneider, R. Wörner, C. Holm, E. Sirtl, and P. Wagner. Tellurium donors in silicon. *Physical Review B*, 24:4571, 1981.

[40] H.G. Grimmeiss, E. Janzén, and K. Larsson. Multivally spin splitting of 1s states for sulfur, selenium, and tellurium donors in silicon. *Physical Review B*, 25:2627, 1982.

[41] H.G. Grimmeiss, E. Janzén, and B. Skarstam. Deep sulfur-related centers in silicon. *Journal of Applied Physics*, 51:4212, 1980.

[42] H.G. Grimmeiss and L. Ledebo. Photo-ionization of deep impurity levels in semiconductors with non-parabolic bands. *Journal of Physics C*, 8:2615, 1975.

[43] H.G. Grimmeiss and B. Skarstam. Excited states at deep centers in Si:S and Si:Se. *Physical Review B*, 23:1947, 1980.

[44] R.N. Hall. Electron-Hole Recombination in Germanium. *Physical Review*, 87:387, 1952.

[45] J. Hansen, M. Sato, R. Ruedy, P. Kharecha, A. Lacis, R. Miller, L. Nazarenko, K. Lo, G.A. Schmidt, G. Russell, I. Aleinov, S. Bauer, E. Baum, B. Cairns, V. Canuto, M. Chandler, Y. Cheng, A. Cohen, A. Del Genio, G. Faluvegi, E. Fleming, A. Friend, T. Hall, C. Jackman, J. Jonas, M. Kelley, N.Y. Kiang, D. Koch, G. Labow, J. Lerner, S. Menon, T. Novakov, V. Oinas, Ja. Perlwitz, Ju. Perlwitz, D. Rind, A. Romanou, R. Schmunk, D. Shindell, P. Stone, S. Sun, D. Streets, N. Tausnev, D. Thresher, N. Unger, M. Yao, and S. Zhang. Dangerous human-made interference with climate: a GISS modelE study. *Atmospheric Chemistry and Physics*, 7:2287, 2007.

[46] V.M. Harutyunyan, Z.N. Adamyan, R.S. Barseghyan, F.V. Gasparyan, M.H. Azaryan, B.O. Semerdjian, Z.H. Mkhitaryan, and S.V. Melkonyan. Phenomena in silicon photodiodes doped with Zn and S. *Infrared Physics*, 26:267, 1986.

[47] B.L. Henke, E.M Gullikson, and J.C. Davis. *Atomic Data and Nuclear Data Tables*, 55:181, 1993.

[48] T.H. Her, R.J. Finlay, C. Wu, and E. Mazur. Femtosecond laser-induced formation of spikes on silicon. *Applied Physics A*, 70:383, 2000.

[49] R.M. Hill. Hopping conduction in amorphous solids. *Philosophical Magazine*, 91:1307, 1971.

[50] H. Indusekhar and V. Kumar. Properties of iron related quenched-in levels in *p*-silicon. *Physica Status Solidi A*, 95:269, 1986.

[51] J.C. Inkson. Deep impurities in semiconductors. II. The optical cross section. *Journal Physics C*, 14:1093, 1981.

[52] E. Janzén, H.G. Grimmeiss, A. Lodding, and C. Deline. Diffusion of tellurium dopant in silicon. *Journal of Applied Physics*, 53:7367, 1982.

[53] E. Janzén, R. Stedman, G. Grossmann, and H.G. Grimmeiss. High-resolution studies of sulfur-and selenium-related donor centers in silicon. *Physical Review B*, 29:1907, 1984.

[54] M. Jaros. Wave functions and optical cross sections associated with deep centers in semiconductors. *Physical Review B*, 16:3694, 1977.

[55] P. Jensen. The potential energy surface for the electronic ground state of the water molecule determined from experimental data using a variational approach. *Journal of Molecular Spectroscopy*, 133:438, 1989.

[56] J.J. Jia, T.A. Callcott, J. Yurkas, A.W. Ellis, F.J. Himpsel, M.G. Samant, J. Stohr, D.L. Ederer, J.A. Carlisle, and E.A. Hudson. First experimental results from IBM/TENN/TULANE/LLNL/LBL undulator beamline at the advanced light source. *Review of Scientific Instruments*, 66:1394, 1995.

[57] N.V. Joshi (editor). *Photoconductivity: Art, Science, and Technology.* Marcel Dekker, New York, New York, 1990.

[58] A. Karoui. Comment on "Lifetime recovery in ultra-highly titanium-doped silicon for the implementation of an intermediate band material" [Appl. Phys. Lett. 94, 042115 (2009)]. *Applied Physics Letters*, 101:236101, 2012.

[59] M.J. Keevers and M.A. Green. Efficiency improvements of silicon solar cells by the impurity photovoltaic effect. *Journal of Applied Physics*, 75:4022, 1994.

[60] T.G. Kim, J.M. Warrender, and M.J. Aziz. Strong sub-band-gap infrared absorption in silicon supersaturated with sulfur. *Applied Physics Letters*, 88:241902, 2006.

[61] J.A. Kittl, P.G. Sanders, M.J. Aziz, D.P. Brunco, and M.O. Thompson. Complete experimental test of kinetic models for rapid alloy solidification. *Acta Materialia*, 48:4797, 2000.

[62] W.E. Krag and J. Zeigner. Infrared absorption spectrum of sulfur-doped silicon. *Physical Review Letters*, 8:485, 1962.

[63] J.J. Krich, B.I. Halperin, and A. Aspuru-Guzik. Nonradiative lifetimes in intermediate band photovoltaics–Absence of lifetime recovery. *Journal of Applied Physics*, 112:013707, 2012.

[64] S. Kuge and N. Hiroshi. Solubility and Diffusion Coefficient of Electrically Active Titanium in Silicon. *Japanese Journal of Applied Physics*, 30:2659, 1991.

[65] V.A. Kul'bachinskii, V.G. Kytin, V.V. Abramov, A.B. Timofeev, A.G. Ul'yashin, and N.V. Shlopak. Hopping conductivity in sulfur-ion-implanted silicon. *Soviet Physics Semiconductors*, 26:1009, 1992.

[66] Y.J. Lee, J. von Boehm, M. Pesola, and R. Nieminen. First-principles study of migration, restructuring, and dissociation energies of oxygen complexes in silicon. *Physical Review B*, 65:085205, 2002.

[67] Y.J. Lee, J. von Boehm, M. Pesola, and R.M. Nieminen. Comparison of oxygen-chain models for late thermal double donors in silicon. *Applied Physics Letters*, 82:2094, 2003.

[68] M.Y. Levy and C. Honsberg. Absorption coefficients of intermediate-band media. *Journal of Applied Physics*, 106:073103, 2009.

[69] L Ley, J Reichardt, and RL Johnson. Static charge fluctuations in amorphous silicon. *Physical Review Letters*, 49:1664, 1982.

[70] S.S. Li and W.R. Thurber. The dopant density and temperature dependence of electron mobility and resistivity in n-type silicon. *Solid State Electronics*, 20:609, 1977.

[71] N. López, L. Reichertz, Kin M. Yu, K. Campman, and W. Walukiewicz. Engineering the Electronic Band Structure for Multiband Solar Cells. *Physical Review Letters*, 106:028701, 2011.

[72] G. Lucovsky. On the photoionization of deep impurity centers in semiconductors. *Solid State Communications*, 3:299, 1965.

[73] A. Luque and A. Martí. Increasing the efficiency of ideal solar cells by photon induced transitions at intermediate levels. *Physical Review Letters*, 78:5014, 1997.

[74] A. Luque and A. Martí. A metallic intermediate band high efficiency solar cell. *Progress in Photovoltaics: Research and Applications*, 9:73, 2001.

[75] A. Luque and A. Martí. The Intermediate Band Solar Cell: Progress Toward the Realization of an Attractive Concept. *Advanced Materials*, 22:160, 2010.

[76] A. Luque, A. Martí, E. Antolín, P.G. Linares, I. Tobías, and I. Ramiro. Radiative thermal escape in intermediate band solar cells. *AIP Advances*, 1:022125, 2011.

[77] A. Luque, A. Martí, E. Antolín, and C. Tablero. Intermediate bands versus levels in non-radiative recombination. *Physica B*, 382:320, 2006.

[78] D. MacDonald and L.J. Geerligs. Recombination activity of interstitial iron and other transition metal point defects in p- and n-type crystalline silicon. *Applied Physics Letters*, 85:4061, 2004.

[79] A. Martí, E. Antolin, C.R. Stanley, C.D. Farmer, N. Lopez, P. Diáz, E. Canovas, P.G. Linares, and A. Luque. Production of photocurrent due to intermediate-to-conduction-band transitions: a demonstration of a key operating principle of the intermediate-band solar cell. *Physical Review Letters*, 97:247701, 2006.

[80] A. Martí, N. Lopez, E. Antolin, E. Canovas, C. Stanley, C. Farmer, L. Cuadra, and A. Luque. Novel semiconductor solar cell structures: the quantum dot intermediate band solar cell. *Thin Solid Films*, 511:638, 2006.

[81] M.D. McCluskey. Local vibrational modes of impurities in semiconductors. *Journal of Applied Physics*, 87:3593, 2000.

[82] P. Migliorato and C.T. Elliott. Sulphur Doped Silicon IR Detectors. *Solid State Electronics*, 21:443, 1978.

[83] A.E. Mills. *Basic Heat and Mass Transfer.* Prentice Hall, Saddle River, New Jersey, 1999.

[84] N.F. Mott. Metal-insulator transition. *Reviews of Modern Physics*, 40:677, 1968.

[85] N.F. Mott. Charge transport in non-crystalline semiconductors. *Festkörperprobleme*, 9:22, 1969.

[86] N.F. Mott. The pre-exponential factor in the conductivity of amorphous silicon. *Philosophical Magazine Part B*, 51:19, 1985.

[87] N.F. Mott and W.D. Twose. The theory of impurity conduction. *Advances in Physics*, 10:107, 1961.

[88] J. Narayan, O.W. Holland, C.W. White, and R.T. Young. Excimer laser annealing of ion-implanted silicon. *Journal of Applied Physics*, 55:1125, 1984.

[89] J. Narayan, R.T. Young, and C.W. White. A comparative study of laser and thermal annealing of boron-implanted silicon. *Journal of Applied Physics*, 49:3912, 1978.

[90] B.K. Newman, E. Ertekin, J.T. Sullivan, M.T. Winkler, M.A. Marcus, S.C. Fakra, M.J. Sher, E. Mazur, J.C. Grossman, and T. Buonassisi. Extended x-ray absorption fine structure of selenium-hyperdoped silicon. submitted Feb. 2013.

[91] B.K. Newman, J.T. Sullivan, M.T. Winkler, M.J. Sher, M.A. Marcus, S. Fakra, M.J. Smith, S Gradečak, E. Mazur, and T. Buonassisi. Illuminating the mechanism for sub-bandgap absorption in chalcogen doped silicon materials for PV applications. *Proceedings from the 24th European Photovoltaics Solar Energy Conference*, page 236, 2009.

[92] T.H. Ning and C.T. Sah. Photoionization cross sections of a two-electron donor center in silicon. *Physical Review B*, 14:2528, 1976.

[93] T. Okumura and K.N. Tu. Analysis of parallel Schottky contacts by differential internal photoemission spectroscopy. *Journal of Applied Physics*, 54:922, 1983.

[94] M. Okuyama, N. Matsunaga, J.W. Chen, and A.G. Milnes. Photoionization cross-section and energy levels of Gold, Iron, Platinum, Silver, and Titanium. *Journal of Electronic Materials*, page 501, 1979.

[95] J. Olea, A. del Prado, D. Pastor, I. Mártil, and G. González-Díaz. Sub-bandgap absorption in Ti implanted Si over the Mott limit. *Journal of Applied Physics*, 109:113541, 2011.

[96] J. Olea, G. Gónzalez-Diáz, D. Pastor, and I. Mártil. Electronic transport properties of Ti-impurity band in Si. *Journal of Physics D*, 42:085110, 2009.

[97] J. Olea, D. Pastor, I. Mártil, and G. González-Díaz. Thermal stability of intermediate band behavior in Ti implanted Si. *Solar Energy Materials And Solar Cells*, 94:1907, January 2010.

[98] J. Olea, D. Pastor, M. Toledano-Luque, I. Mártil, and G. Gonzalez-Diáz. Depth profile study of Ti implanted Si at very high doses. *Journal of Applied Physics*, 110:064501, 2011.

[99] J. Olea, M. Toledano-Luque, D. Pastor, G. Gónzalez-Díaz, and I. Mártil. Titanium doped silicon layers with very high concentration. *Journal of Applied Physics*, 104:016105, 2008.

[100] J. Olea, M. Toledano-Luque, D. Pastor, E. San-Andres, I. Mártil, and G. González-Diáz. High quality Ti-implanted Si layers above the Mott limit. *Journal of Applied Physics*, 107:103524, 2010.

[101] S.H. Pan, D. Recht, S. Charnvanichborikarn, J.S. Williams, and M.J. Aziz. Enhanced visible and near-infrared optical absorption in silicon supersaturated with chalcogens. *Applied Physics Letters*, 98:121913, 2011.

[102] D. Pastor, J. Olea, A. del Prado, E. García-Hemme, R. García-Hernansanz, and G. González-Díaz. Insulator to metallic transition due to intermediate band formation in Ti-implanted silicon. *Solar Energy Materials And Solar Cells*, 104:159, 2012.

[103] D.K. Paul and S.S. Mitra. Evaluation of Mott's parameters for hopping conduction in amorpous Ge, Si, and Se-Si. *Physical Review Letters*, 31:1000, 1974.

[104] A.G.U. Perera, H.X. Yuan, and M.H. Francombe. Homojunction internal photoemission far-infrared detectors: photoresponse performance analysis. *Journal of Applied Physics*, 77:915, 1995.

[105] P.D. Persans, N.E. Berry, D. Recht, D. Hutchinson, H. Peterson, J. Clark, S. Charnvanichborikarn, J.S. Williams, A. DiFranzo, M.J. Aziz, and J.M. Warrender. Photocarrier lifetime and transport in silicon supersaturated with sulfur. *Applied Physics Letters*, 101:111105, 2012.

[106] P.D. Persans, N.E. Berry, D. Recht, D. Hutchinson, A.J. Said, J.M. Warrender, H. Peterson, A. DiFranzo, C. McGahan, J. Clark, W. Cunningham, and M.J. Aziz. Photocarrier excitation and transport in hyperdoped planar silicon devices. *Materials Research Society Symposium Proceedings*, 1321:291, 2011.

[107] H. Pettersson, R. Passler, F. Blaschta, and H.G. Grimmeiss. Temperature dependence of optical properties of the deep sulfur center in silicon. *Journal of Applied Physics*, 80:5312, 1996.

[108] C.J. Powell and A. Jablonski. Evaluation of calculated and measured electron inelastic mean free paths near solid surfaces. *Journal of Physical and Chemical Reference Data*, 28:19, 1999.

[109] F. Priolo, J.M. Poate, D.C. Jacobson, J.L. Batstone, J.S. Custer, and M.O. Thompson. Trapping of Au in Si during pulsed laser irradiation: A comparison with ion beam induced segregation. *Applied Physics Letters*, 53:2486, 1988.

[110] D. Recht. *Energetic beam processing of silicon to engineer optoelectronically active defects.* PhD thesis, Harvard University, 2012.

[111] D. Recht, D. Hutchinson, T. Cruson, A. DiFranzo, A. McAllister, A.J. Said, J.M. Warrender, P.D. Persans, and M.J. Aziz. Contactless microwave measurements of photoconductivity in silicon hyperdoped with chalcogens. *Applied Physics Express*, 5:041301, 2012.

[112] D. Recht, J.T. Sullivan, R. Reedy, T. Buonassisi, and M.J. Aziz. Controlling dopant profiles in hyperdoped silicon by modifying dopant evaporation rates during pulsed laser melting. *Applied Physics Letters*, 100:112112, 2012.

[113] R. Reitano, P.M. Smith, and M.J. Aziz. Solute trapping of group III, IV, and V elements in silicon by an aperiodic stepwise growth mechanism. *Journal of Applied Physics*, 76:1518, 1994.

[114] A. Rogalski. Infrared detectors: status and trends. *Progress in Quantum Electronics*, 27:59.

[115] T.F. Rosenbaum, K. Andres, G.A Thomas, and R.N. Bhatt. Sharp metal-insulator transition in a random solid. *Physical Review Letters*, 45:1723, 1980.

[116] L.L. Rosier. Photoionization of Electrons at Sulfur Centers in Silicon. *Journal of Applied Physics*, 42:4000, 1971.

[117] J.E. Rubensson, D. Mueller, R. Shuker, D.L. Ederer, C.H. Zhang, J. Jia, and T.A. Callcott. Excitation-energy depedence in the $L_{2,3}$ fluorescence-spectrum of Si. *Physical Review Letters*, 64:1047, 1990.

[118] C.T. Sah, A.F. Tasch, Jr, and D.K. Schroder. Precise determination of the multiphonon and photon carrier generation properties using the impurity photovoltaic effect in semiconductors. *Physical Review Letters*, 19:69, 1967.

[119] C.T. Sah, A.F. Tasch, Jr, and D.K. Schroder. Recombination properties of the gold acceptor level in silicon using the impurity photovoltaic effect. *Physical Review Letters*, 19:71, 1967.

[120] A.J. Said, D. Recht, J.T. Sullivan, J.M Warrender, T. Buonassisi, P.D. Persans, and M.J. Aziz. Extended infrared photoresponse and gain in chalcogen-supersaturated silicon photodiodes. *Applied Physics Letters*, 99:073503, 2011.

[121] C.D. Salzberg and J.J. Villa. Infrared Refractive Indexes of Silicon Germanium and Modified Selenium Glass. *Journal of the Optical Society of America*, 47:244, 1957.

[122] K. Sánchez, I. Aguilera, P. Palacios, and P. Wahnón. Assessment through first-principles calculations of an intermediate-band photovoltaic material based on Ti-implanted silicon: Interstitial versus substitutional origin. *Physical Review B*, 79:165203, 2009.

[123] K. Sánchez, I. Aguilera, P. Palacios, and P. Wahnón. Formation of a reliable intermediate band in Si heavily coimplanted with chalcogens (S, Se, Te) and group III elements (B, Al). *Physical Review B*, 82:165201, 2010.

[124] W. Schelter, W. Hell, R. Helbig, and M. Schulz. Optical properties of indium-doped silicon reinspected. *Journal of Physics C*, 15:5839, 2013.

[125] D. Schroder, R. Thomas, and J. Swartz. Free carrier absorption in silicon. *IEEE Transactions on Electron Devices*, 1978.

[126] N. Sclar. The effect of dopant diffusion vapor-pressure on the properties of sulfur and selenium doped silicon infrared detectors. *Journal of Applied Physics*, 52:5207, 1981.

[127] W. Shan, W. Walukiewicz, J.W. Ager, E.E. Haller, J.F. Geisz, D.J. Friedman, J.M. Olson, and S.R. Kurtz. Band anticrossing in GaInNAs alloys. *Physical Review Letters*, 82:1221, 1999.

[128] M.A. Sheehy, B.R. Tull, C.M. Friend, and E. Mazur. Chalcogen doping of silicon via intense femtosecond-laser irradiation. *Materials Science And Engineering B*, 137:289, 2007.

[129] W. Shockley and H.J. Queisser. Detailed balance limit of efficiency of $p-n$ junction solar cells. *Journal of Applied Physics*, 32:510, 1961.

[130] W. Shockley and W.T. Read. Statistics of the recombinations of holes and electrons. *Physical Review*, 87:835, 1952.

[131] V.B. Shuman, A.A. Makhova, Yu.A. Astrov, A.M. Ivanov, and A.N. Lodygin. Solubility of sulfur in silicon. *Semiconductors*, 46:969, 2012.

[132] L. Siller, S. Krishnamurthy, L. Kjeldgaard, B.R. Horrocks, Y. Chao, A. Houlton, A.K. Chakraborty, and M.R.C. Hunt. Core and valence exciton formation in X-ray absorption, X-ray emission and X-ray excited optical luminescence from passivated Si nanocrystals at the Si $L_{2,3}$ edge. *Journal of Physics: Condensed Matter*, 21:095005, 2009.

[133] A.F. Sklensky and R.H. Bube. Photoelectronic properties of zinc impurity in silicon. *Physical Review B*, 6:1328, 1972.

[134] K. Sueoka, N. Ikeda, T. Yamamoto, and S. Kobayashi. Morphology and growth process of thermally induced oxide precipitates in Czochralski silicon. *Journal of Applied Physics*, 74:5437, 1993.

[135] J.T. Sullivan, R.G. Wilks, M.T. Winkler, L. Weinhardt, D. Recht, A.J. Said, B.K. Newman, Y. Zhang, M. Blum, and S. Krause. Soft X-ray emission spectroscopy studies of the electronic structure of silicon supersaturated with sulfur. *Applied Physics Letters*, 99:142102, 2011.

[136] B.O. Sundstrom, L. Huldt, and N.G. Nilsson. Electron capture coefficient of neutral indium and pair recombination in compensated silicon. *Journal of Physics C*, 15:3359, 1982.

[137] M. Tabbal, T. Kim, J.M. Warrender, M.J. Aziz, B.L. Cardozo, and R.S. Goldman. Formation of single crystal sulfur supersaturated silicon based junctions by pulsed laser melting. *Journal of Vacuum Science & Technology B*, 25:1847, 2007.

[138] M. Tabbal, T. Kim, D.N. Woolf, B. Shin, and M.J. Aziz. Fabrication and sub-band-gap absorption of single-crystal Si supersaturated with Se by pulsed laser mixing. *Applied Physics A*, 98:589, 2010.

[139] A.F. Tasch, Jr and C.T. Sah. Recombination-generation and optical properties of gold acceptor in silicon. *Physical Review B*, 1:800, 1970.

[140] F.L. Thiel. Electronic Properties of Silicon Doped with Silver. *Journal of Applied Physics*, 41:254, 1970.

[141] A. Thompson, D. Attwood, E. Gullikson, M. Howellis, K. Kim, J. Kirz, J. Kortright, I. Lindau, Y. Liu, P. Pianetti, A. Robinson, J. Scofield, J. Underwood, and G. Wiliams, G. Williams. X-ray data booklet. Center for X-ray Optics and Advanced Light Source, Lawrence Berkeley National Laboratory, 2009.

[142] B.R. Tull, M.T. Winkler, and E. Mazur. The role of diffusion in broadband infrared absorption in chalcogen-doped silicon. *Applied Physics A*, 96:327, 2009.

[143] W. Wang, A.S. Lin, and J.D. Phillips. Intermediate-band photovoltaic solar cell based on ZnTe:O. *Applied Physics Letters*, 95:011103, 2009.

[144] W. Wang, A.S. Lin, J.D. Phillips, and W.K. Metzger. Generation and recombination rates at ZnTe:O intermediate band states. *Applied Physics Letters*, 95:261107, 2009.

[145] T.M.L. Wigley. *Climate Change*, 5:315, 1983.

[146] M.T. Winkler. *Non-Equilibrium Chalcogen Concentrations in Silicon: Physical Structure, Electronic Transport, and Photovoltaic Potential.* PhD thesis, Harvard University, 2009.

[147] M.T. Winkler, D. Recht, M.J. Sher, A.J. Said, E. Mazur, and M.J. Aziz. Insulator-to-metal transition in sulfur-doped silicon. *Physical Review Letters*, 106:178701, 2011.

[148] C. Wu, C.H. Crouch, L. Zhao, J.E. Carey, R. Younkin, J.A. Levinson, E. Mazur, R.M. Farrell, P. Gothoskar, and A. Karger. Near-unity below-band-gap absorption by microstructured silicon. *Applied Physics Letters*, 78:1850, 2001.

[149] K. Wunstel, K. Froehner, and P. Wagner. Iron-related defects in silicon. *Physica B*, page 301, 1983.

[150] D. Yang, X. Ma, R. Fan, J. Zhang, L. Li, and D. Que. Oxygen precipitation in nitrogen-doped Czochralski silicon. *Physica B*, 273:308, 1999.

[151] R.T. Young, J. Narayan, and R.F. Wood. Electrical and structural characteristics of laser-induced epitaxial layers in silicon. *Applied Physics Letters*, 35:447, 1979.

[152] R.T. Young, C.W. White, G.J. Clark, J. Narayan, W.H. Christie, M. Murakami, P.W. King, and S.D. Kramer. Laser annealing of boron-implanted silicon. *Applied Physics Letters*, 32:139, 1978.

[153] K.M. Yu, W. Walukiewicz, J. Wu, W. Shan, J.W. Beeman, M.A. Scarpulla, O.D. Dubon, and P. Becla. Diluted II-VI oxide semiconductors with multiple band gaps. *Physical Review Letters*, 91:246403, 2003.

[154] H.X. Yuan and A.G.U. Perera. Dark current analysis of Si homojunction interfacial work function internal photoemission far-infrared detectors. *Applied Physics Letters*, 66:2262, 1995.

[155] J. Yuan, H. Shen, H. Huang, and X. Deng. Positive or negative gain: Role of thermal capture cross sections in impurity photovoltaic effect. *Journal of Applied Physics*, 110:104508, 2011.

[156] J. Yuan, H. Shen, F. Zhong, and X. Deng. Impurity photovoltaic effect in magnesium-doped silicon solar cells with two energy levels. *Physica Status Solidi A*, 209:1002, 2012.

[157] N.F. Zobov, O.L. Polyansky, C.R. Le Sueur, and J. Tennyson. Vibration-rotation levels of water beyond the Born-Oppenheimer approximation. *Chemical Physical Letters*, 260:381, 2003.